nature aging

Article

https://doi.org/10.1038/s43587-026-01204-0

Fibronectin mediates APOE4-driven blood–brain barrier dysfunction in Alzheimer's disease

Received: 24 February 2025

Accepted: 27 July 2026

Published online: 11 September 2026

Check for updates

A list of authors and their affiliations appears at the end of the paper

Blood–brain barrier (BBB) dysfunction is an early feature of Alzheimer's disease (AD) and is particularly pronounced in individuals carrying the *APOE* ε4 allele, but the mechanisms linking *APOE* ε4 to BBB failure remain unclear. Here we show that astrocyte-derived fibronectin (FN1) is a key mediator of apolipoprotein E4 (APOE4)-driven BBB dysfunction in AD. Using postmortem human brain tissue, human three-dimensional vascular models and in vivo models, we demonstrate that APOE4, amyloid-β42 and inflammatory signals induce astrocytic FN1 upregulation and excessive perivascular deposition. Fibronectin accumulation is sufficient to cause BBB leakage and disrupt VEGF/HB-EGF/IGF-1 signaling through integrin-mediated focal adhesion kinase activity. Reducing fibronectin or restoring growth factor signaling rescues BBB function in vitro and in vivo. Together, evidence from experimental models, human brain tissue and clinical datasets identifies fibronectin as a proximal mediator of APOE4-driven gliovascular dysfunction and highlights FN1 as a potential therapeutic target for vascular and BBB dysfunction in AD.

Blood–brain barrier (BBB) dysfunction is a hallmark of Alzheimer's disease (AD)[1–6] and is exacerbated in individuals carrying the *APOE* ε4 allele, the strongest genetic risk factor for late-onset AD[7,8]. Remodeling of the extracellular matrix (ECM) contributes to BBB dysfunction[2,3,9–11], but the mechanisms linking apolipoprotein E4 (APOE4) and ECM remodeling remain unclear. We previously reported that *APOE* ε4 carriers with AD accumulate fibronectin at the gliovascular interface of the BBB, and that a protective loss-of-function fibronectin 1 (FN1) variant reduces AD risk by 71% (ref. 12). These findings implicate fibronectin as a downstream mediator of APOE4 but leave its pathogenic mechanism unresolved. Here, we demonstrate that APOE4 and amyloid-β42 (Aβ42) drive the pathological accumulation of astrocyte-derived fibronectin at the gliovascular interface, disrupting astrocyte–endothelial communication and growth factor signaling essential for BBB integrity. Integrating human genetics, postmortem neuropathology, cerebrospinal fluid (CSF) analyses, single-cell transcriptomics, human induced pluripotent stem (iPS) cell-derived cerebrovascular models, and complementary zebrafish and mouse models, we establish fibronectin as a key mechanistic mediator of BBB dysfunction in AD.

Results

Fibronectin is induced in human brains with AD and cerebrovascular pathology

Because AD and cerebrovascular pathology (CVP) frequently coexist[4,13–17], we examined whether both conditions promote fibronectin deposition. We hypothesized that these conditions may induce fibronectin deposition and contribute to BBB dysfunction. To test this hypothesis, we examined fibronectin upregulation as a shared pathological feature in AD and CVP. We performed immunolabeling for fibronectin and CD31 (a vascular endothelial marker) in the dorsolateral prefrontal cortex (Brodmann area 9) of 23 postmortem human brains divided into four groups based on postmortem neuropathological assessments (Fig. 1a–e and Supplementary Table 1): (1) no CVP or AD (control brains; Braak stage 0–I, no antemortem cognitive abnormalities, arteriolosclerosis score (ATS; indicating microvascular pathology) 0–1, $n = 5$); (2) CVP without AD (ATS 3–4, Braak stage 0–II or higher without antemortem cognitive abnormalities, $n = 6$); (3) AD without CVP (Braak stage IV–VI, ATS 0–1, $n = 6$); and (4) coincident CVP and AD (Braak stage IV–VI, ATS 3–4, $n = 6$)[12]. We observed significantly higher

e-mail: ck2893@cumc.columbia.edu

FN1 levels in CVP brains (+46.7%, generalized estimating equation (GEE) donor-level comparison: $P = 1.8 \times 10^{-4}$) and codirectionally elevated trends in AD and AD + CVP (+22.3% and +21.0%, respectively) under conservative donor-level inference (Fig. 1f–h). As a secondary analysis, when we combined all pathology groups and compared them to controls, we observed a significant overall effect on FN1 levels (+29.1%, GEE donor-level $P = 8.0 \times 10^{-3}$).

Tissue fibronectin has two variants, one containing extra domain A (EDA) and the other containing extra domain B (EDB), which may be differentially deposited in the brains of individuals with AD. We tested isoform specificity using isoform-targeting antibodies to FN1-EDA and FN1-EDB but observed no preferential deposition of EDA or EDB (Extended Data Fig. 1a,b). We also observed that FN1 deposits coincide with morphological changes in microglia from ramified to amoeboid forms, with IBA1-positive microglia often appearing proximal to and encircling FN1 accumulations in AD brains (Extended Data Fig. 1a–c).

Fibronectin is induced at vasculature in mouse models of APOE4 expression and AD

To validate our results from human brains, we used aged (21- to 22-month-old) *APOE* ε3 and *APOE* ε4 knock-in mice[18], as *APOE* ε4 mice have previously been shown to exhibit CVP[19,20]. APOE knock-in mice allowed us to isolate APOE4-dependent effects independent of overt AD pathology. We performed immunolabeling for fibronectin and CD31 in brain sections from both genotypes, followed by quantitative analyses of randomly selected regions of the cortex (Fig. 1i–k) to evaluate the contribution of *APOE* ε4 to fibronectin accumulation. By comparing FN1 levels between genotypes using animals as the unit of inference, we found that *APOE* ε4 mouse brains showed markedly higher FN1 levels than *APOE* ε3 brains, with a percentage difference of +98.9% (95% confidence interval, 84.1–113.7%; $P = 4.1 \times 10^{-39}$), indicating a robust genotype-dependent effect (Fig. 1j,k). Elevated FN1 levels were a consistent feature in the brains of the APP knock-in mouse model[21] (Extended Data Fig. 1d).

Given that fibrinogen extravasation is an indication of BBB dysfunction[22,23], we assessed fibrinogen leakage in *APOE* ε4 versus *APOE* ε3 mouse brains to determine whether fibronectin accumulation correlates with this BBB compromise. *APOE* ε4 mouse brain tissue exhibited markedly elevated fibrinogen accumulation in the vasculature compared to *APOE* ε3 brains (Fig. 1l). A log-normal quantile–quantile (QQ) plot confirmed that fibrinogen intensity values followed a log-normal distribution (Fig. 1m), validating the use of parametric statistics. Quantitative analysis revealed a significant increase in fibrinogen intensity in vessels from *APOE* ε4 mouse brains relative to vessels from *APOE* ε3 brains (Fig. 1n). This genotype-dependent increase was consistently observed across individual mice (Fig. 1o). Furthermore, colocalization analysis showed that FN1 and fibrinogen overlap was significantly higher in *APOE* ε4 than in *APOE* ε3 mouse brains (Fig. 1p). Confirming these observations, comparison of the dextran-based vessel leakage assay in control and *APOE* ε4 mouse brains (Extended Data Fig. 1e) showed significantly increased fibronectin deposition and dextran–Texas Red extravasation in *APOE* ε4 mice compared to control mice (Extended Data Fig. 1f–h), supporting the presence of a dysfunctional BBB and increased leakiness with elevated fibronectin levels in *APOE* ε4 mice. These results also provide evidence implicating fibronectin deposition as a pathological mediator of cerebrovascular dysfunction in AD[2,5,6,16,24,25].

Fibronectin is associated with altered gliovascular unit in AD

To examine fibronectin's association with gliovascular alterations in AD, we analyzed its spatial relationship with the astrocyte endfeet marker aquaporin-4 (AQP4) and the endothelial marker CDH5 (also known as VE-cadherin) in postmortem human brain tissue (Extended Data Fig. 2a–f). In controls, AQP4 showed polarized perivascular localization that overlapped with FN1, consistent with fibronectin localization within perivascular astrocyte-associated regions. In AD, AQP4 appeared more diffusely distributed with reduced perivascular polarization, while FN1 deposition was broader (Extended Data Fig. 2a). Although AQP4 remains an astrocytic endfoot protein, its normal perivascular enrichment is reduced in AD, reflecting an altered spatial organization of astrocytic endfeet relative to the vasculature. Quantitative analysis showed that the proximity between vascular FN1 and AQP4 was significantly increased in AD compared to controls (138.5%, $P = 1.41 \times 10^{-13}$), indicating altered spatial relationships within the gliovascular niche (Extended Data Fig. 2b). We next examined endothelial CDH5 distribution in control and AD human brain tissue. We detected CDH5 immunoreactivity along cortical vessels in both groups, with reduced overall signal intensity in AD samples compared to controls (Extended Data Fig. 2c,d). To assess the colocalization of fibronectin with CDH5, we performed pixel-wise colocalization analysis (Extended Data Fig. 2e,f). Compared to controls, AD brains showed a pronounced increase in fibronectin–CDH5 colocalization (Pearson

Fig. 1 | *APOE* ε4 induces fibronectin deposition in CVP and AD. a–d′, Double immunofluorescence staining for CD31 and FN1 with DAPI nuclear counterstain (blue) in control (**a**, **a′**), AD (**b**, **b′**), CVP (**c**, **c′**) and AD + CVP (**d**, **d′**) conditions. **e**, Higher-magnification images of individual vessels. **f**, Left: schematic depiction of the criteria for intensity and area measurements for 1,949 blood vessels. Right: distribution histogram. **g**, QQ plot for mean intensity values of CD31 and FN1 in control, AD, CVP and AD + CVP conditions. Blue points, observed residual quantiles; orange diagonal line, expected quantiles under a normal distribution. **h**, Quantification of FN1 levels across control, CVP, AD and AD + CVP human brain samples. Each dot represents one blood vessel. Measurements were obtained from $n = 5$ control, $n = 6$ CVP, $n = 6$ AD and $n = 6$ AD + CVP independent human donors. Multiple vessels were analyzed per donor, and statistical inference was performed at the donor level using GEEs (two-sided) to account for repeated measurements. Red lines, mean values. **i**, Schematic overview of the experimental approach illustrating the use of mouse models carrying the *APOE* ε3 and *APOE* ε4 alleles, the process of histological sectioning and staining, and the subsequent quantification of results. **j**, Comparative analysis of FN1 expression in *APOE* ε3 and *APOE* ε4 mouse models. The left images display merged double immunofluorescence staining for CD31 and FN1. The middle and right images show individual immunofluorescence staining for CD31 and FN1, respectively. **k**, Fluorescence intensity of fibronectin across a number of observations, with corresponding percentage changes and *P* values. The graphs quantify the fluorescence intensity of fibronectin in individual animals. Each data column represents one mouse ($n = 6$ *APOE* ε3/ε3 mice and $n = 6$ *APOE* ε4/ε4 mice). Multiple vessels were analyzed per mouse, and statistical inference was performed at the animal level using GEEs (two-sided). **l**, Representative confocal images of brain sections stained for FN1, fibrinogen and nuclei (DAPI) in *APOE* ε3/ε3 and *APOE* ε4/ε4 brains. Top row, low-magnification views; bottom row, higher magnification of selected regions marked with boxes. **m**, log-normal QQ plots comparing vessel-level fibrinogen intensity in *APOE* ε3/ε3 and *APOE* ε4/ε4, validating the log-normal distribution before statistical testing. **n**, Quantification of fibrinogen intensity across vessels, showing a significant increase in *APOE* ε4/ε4. Each dot represents one vessel; violin plots depict the distribution and median (Kolmogorov–Smirnov, unpaired test, two-tailed). $P < 1.0 \times 10^{-15}$. **o**, Scatter plot of fibrinogen intensity. Each data point represents one vessel. Measurements were obtained from $n = 6$ independent mice per genotype. Multiple vessels were analyzed per mouse, and statistical inference was performed using a nested *t* test with a 95% confidence interval. **p**, Quantification of FN1–fibrinogen colocalization comparing genotypes. Data are presented as mean ± s.e.m. Each data point represents one mouse ($n = 6$ independent mice per genotype). Statistical inference was performed at the animal level using an unpaired *t* test (two-sided). Scale bars, 50 µm (**a**–**d′**, **j**, **l**) and 15 µm (**e**). Data are represented as dot plots or multivariable graphs, and statistical significance is noted as not significant (NS), with the precise *P* value, or as $^{*}P < 0.05$, $^{**}P < 0.005$, $^{***}P < 0.001$ and $^{****}P < 0.0001$. Each data point in the graphs is an individual measurement nested within a replicate cluster; these replicate clusters serve as the units of inference in the GEE with robust SEs.

https://doi.org/10.1038/s43587-026-01204-0

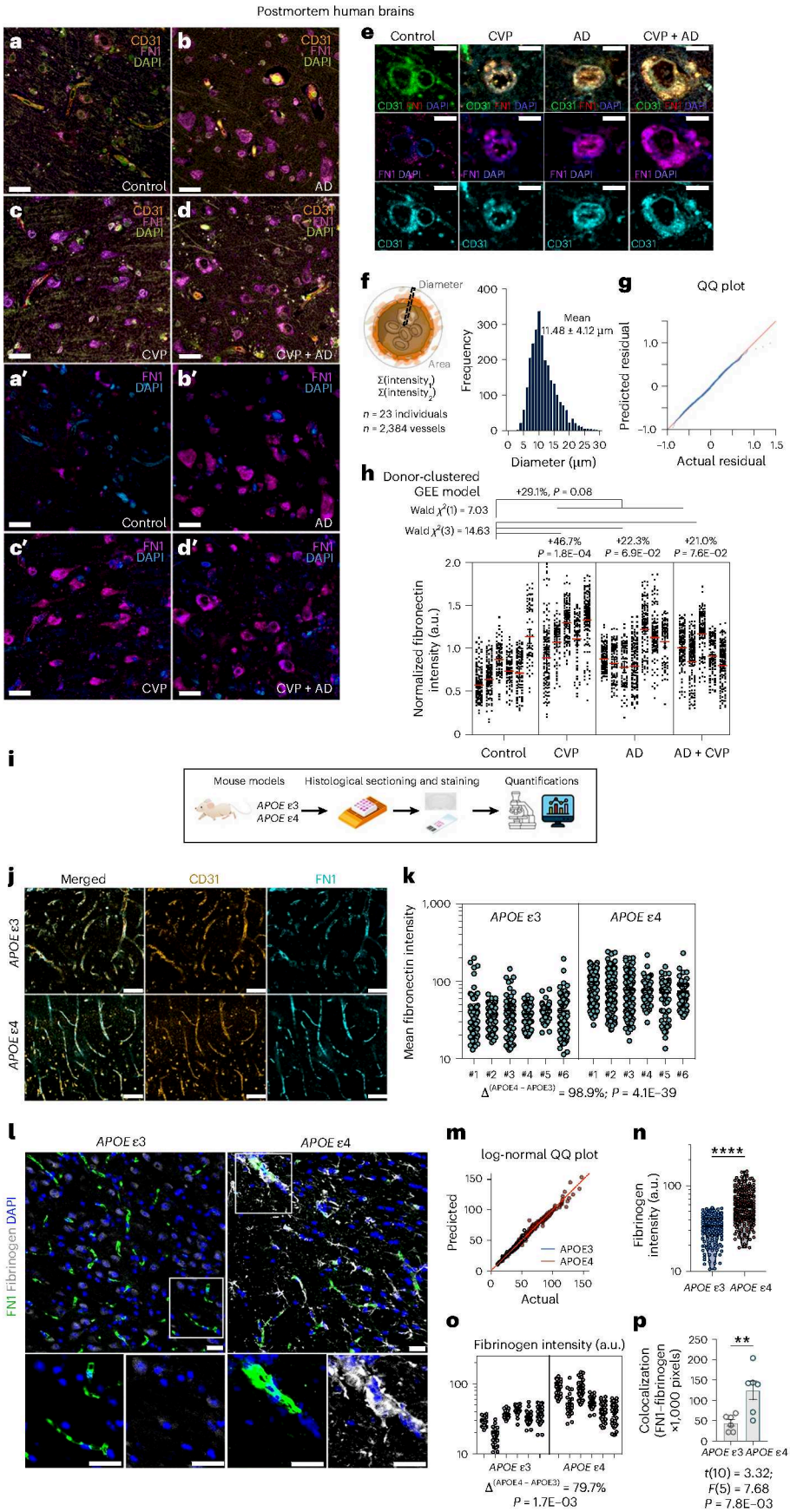

$r = 0.36$; Mander's overlap coefficient = 0.613), accompanied by a rise in Li's intensity correlation quotient (0.068–0.114), indicating a nonrandom spatial association between FN1 and CDH5 in AD. While CDH5 staining reveals altered endothelial CDH5 distribution in AD tissue, definitive assessment of adherens junction ultrastructure would require junction-preserving fixation and thicker tissue sections.

APOE4 induces fibronectin deposition

Having established that the *APOE* ε4 allele exacerbates cerebrovascular injury characterized by fibronectin accumulation and fibrinogen leakage, we next sought to identify the cellular sources and mechanisms driving this deposition. Endothelial cells and astrocytes are prominent cell types of the BBB; therefore, we hypothesized that these cells contribute to fibronectin deposition in an APOE4-dependent manner. We used isogenic human iPS cell-derived *APOE* ε3/ε3 and *APOE* ε4/ε4 astrocytes[26] to examine differences in fibronectin expression. *APOE* ε4/ε4 human astrocytes not only showed increased fibronectin expression but also generated amorphous fibronectin deposits. In contrast, *APOE* ε3/ε3 astrocytes deposited fibronectin at lower levels and in fibrillar, thread-like arrays (Fig. 2a,b). Similarly, when we compared two-dimensional (2D) iPS cell-derived endothelial monolayers and three-dimensional (3D) vasculogenesis and angiogenesis model plexus (VAMP) cultures[27] containing isogenic iPS cell-derived endothelial and mural cells across two independent *APOE* ε3/ε3 and *APOE* ε4/ε4 isogenic pairs, we found that fibronectin expression was increased in the *APOE* ε4/ε4 versions of both models (Fig. 2c–e and Extended Data Fig. 2g). To determine whether fibronectin deposition around the blood vessels increases with *APOE* ε4/ε4, as previously observed in the human brain[12], we measured FN1 intensity proximal to CD31-positive vascular structures in 3D VAMP cultures and found elevated levels in *APOE* ε4/ε4 models compared to isogenic *APOE* ε3/ε3 controls (Fig. 2e). Consistent with the increased fibronectin deposition observed in *APOE* ε4/ε4 cellular and vascular models, we also found that FN1 protein levels were significantly elevated in the CSF of individuals with AD compared to controls (Student's *t* test: $t = 5.22$, $P = 3.31 \times 10^{-7}$) (Fig. 2f).

To identify the *FN1*-expressing cell types in the human brain, we analyzed our recent single-nucleus transcriptomics datasets generated from the brain tissue of 52 individuals[28]. We found that, among 413,175 cells sequenced[28], 19,387 cells express *FN1* (4.7%), and astrocytes constitute 22.7% of *FN1*-expressing cells, while endothelial cells and pericytes together constitute 8.9% of *FN1*-expressing cells (Fig. 2g). To validate these in silico analyses and to determine FN1 protein expression at the cell type level, we performed spatial multiplex immunohistochemistry in human brain samples using cell type-specific markers for major cell types (Fig. 2h and Extended Data Fig. 2h). We observed that astrocytes, endothelial cells and pericytes (Fig. 2h), as well as non-BBB neuronal cells (Extended Data Fig. 2h), express FN1. We also observed that advanced perivascular amyloid aggregates immunoreactive for 4G8 appear to overlap with FN1 deposits associated with astrocytes (Fig. 2h). When we analyzed an independent human single-nucleus RNA-sequencing (snRNA-seq) dataset[28], we found that astrocytes show the highest upregulation of *FN1* with *APOE* ε4 (Extended Data Fig. 3a). To validate these transcriptional changes at the protein level, we analyzed multiplex immunostaining of human brain tissues from *APOE* ε3/ε3 controls, *APOE* ε3/ε3 AD cases and *APOE* ε4/ε4 AD cases. Automated analyses of 1,098,338 cells (165,099 $GFAP^+$ astrocytes, 417,936 MBP^+ oligodendrocytes, 153,096 $IBA1^+$ microglia, 205,398 $MAP2^+$ neurons, 86,668 $CD31^+$ endothelial cells and 70,141 $PDGFR\beta^+$ pericytes) showed that the *APOE* ε4/ε4 genotype increases FN1 protein levels in astrocytes (Extended Data Fig. 3b–e). These results demonstrate that, in the brain, astrocytes drive *APOE* ε4-dependent FN1 deposition at the vascular interface, consistent with their enrichment among FN1-expressing cells in perivascular regions (Fig. 2h).

APOE4 and fibronectin colocalize

APOE is known to form extracellular aggregates[29,30], and we previously showed that fibronectin also accumulates as extracellular deposits[12]. In iPS cell-derived *APOE* ε4/ε4 astrocytes, fibronectin deposits colocalized with APOE4, unlike in *APOE* ε3/ε3 astrocytes (Fig. 3a). *APOE* ε4/ε4 astrocytes also exhibited significantly higher APOE protein levels than *APOE* ε3/ε3 astrocytes (163.6%, $P = 1.6 \times 10^{-21}$) (Fig. 3a,b). At any given APOE intensity, *APOE* ε4/ε4 astrocytes consistently contained more fibronectin than *APOE* ε3/ε3 astrocytes, resulting in significantly higher APOE and FN1 levels (Fig. 3c; ε3: $R^2 = 0.049$, ε4: $R^2 = 0.396$). Accordingly, *APOE* ε4/ε4 astrocytes showed greater colocalization of APOE and fibronectin deposits than *APOE* ε3/ε3 astrocytes (Fig. 3d).

Immunolabeling of APOE, fibronectin and GFAP in postmortem AD brains ($n = 4$ *APOE* ε4/ε4 and $n = 4$ *APOE* ε3/ε3) confirmed these in vitro findings (Fig. 3e,f). Donor-clustered GEE analysis showed significantly increased APOE (+64.9%; $P = 7.3 \times 10^{-3}$) and FN1 (+30.6%; $P = 1.9 \times 10^{-2}$) in *APOE* ε4-associated AD compared to *APOE* ε3-associated AD (Fig. 3f,g). Consistent with this, the correlation between APOE and fibronectin was stronger in *APOE* ε4 carriers than in noncarriers (Fig. 3h; ε3: $R^2 = 0.108$, ε4: $R^2 = 0.154$).

To examine fibronectin localization relative to astrocyte endfeet, we quantified its colocalization with the astrocytic marker AQP4 within FN1-positive regions of interest (ROIs) from cortical sections of *APOE* ε3/ε3 and *APOE* ε4/ε4 brains (Fig. 3i–l). FN1 strongly colocalized with AQP4 across all samples, confirming enrichment at astrocytic endfeet (Fig. 3k). Additionally, APOE4 exhibited greater colocalization with

Fig. 2 | *APOE* ε4 induces fibronectin production in endothelial cells and astrocytes. a, Immunofluorescence staining for FN1 with DAPI counterstain in *APOE* ε3/ε3 and *APOE* ε4/ε4 isogenic iPS cell-derived human astrocytes. Single channels in white show FN1. Rightmost panels show high-magnification images of FN1 deposition. **b**, Top: quantification of FN1 intensity in single cells and their close periphery from acquired images. Bottom: western blot analysis ($n = 3$ samples per group). Each data point represents one cell. Measurements were obtained from $n = 12$ independent biological replicates. Multiple cells were analyzed per biological replicate, and statistical inference was performed using GEEs (two-sided). Data are presented as mean ± s.e.m. $P = 1.0 \times 10^{-9}$. **c**, Human iPS cell-derived *APOE* ε3/ε3 and *APOE* ε4/ε4 endothelial cultures showing the endothelial markers ZO-1 and CD31 with DAPI counterstain. **d**, RT–qPCR results in *APOE* ε3/ε3 and *APOE* ε4/ε4 endothelial cells for *FN1* gene expression (mean ± s.d.; unpaired *t* test, two-sided, $P = 0.0114$). **e**, Left: 3D VAMP cultures from *APOE* ε3/ε3 and *APOE* ε4/ε4 iPS cells stained for CD31 and FN1, showing FN1 deposition at the vascular interface, which increases with *APOE* ε4. Right: quantification graph, where each data point represents an independent 3D VAMP culture. Measurements were obtained from $n = 3$ independent biological replicates per condition. Statistical analyses were performed using biological replicates. Data are presented as mean ± s.e.m. (unpaired *t* test, two-sided). **f**, Violin plots of FN1 expression (relative fluorescence units (RFU) on a $\log_2$ scale) in AD ($n = 156$) and control ($n = 139$) CSF from the Emory Somalogic 7k dataset. Samples are color-coded by case status and APOE genotype (ε2/ε3, ε3/ε3, ε3/ε4, ε4/ε4). Unknown or infrequent genotypes (for example, ε2/ε4) were excluded from the visualization. Statistical test: linear regression model Wald *t* test. **g**, Breakdown of all *FN1*-expressing cells in human brain snRNA-seq analyses from ref. 28. OPC, oligodendrocyte precursor cell; InhN, inhibitory neuron; ExcN, excitatory neuron. **h**, Spatial multiplex immunohistochemistry on AD patient brain tissue sections for FN1, B2M (endothelial cells), PDGFRβ (pericytes) and GFAP + AQP4 (astrocytes and their endfeet). Enlarged images show the strongest FN1 deposits along with cell markers. 4G8 (advanced amyloid aggregate) overlaps with FN1 deposits. Representative images are from two independent runs with similar results. Scale bars, 25 μm (**a**, high-magnification images: 10 μm), 10 μm (**e**, **h**) and 20 μm (**c**). Data are represented as dot plots or multivariable graphs, and statistical significance is noted as NS, with the precise *P* value, or as $^*P < 0.05$, $^{**}P < 0.005$, $^{***}P < 0.001$ and $^{****}P < 0.0001$. Each data point in the graphs is an individual measurement nested within a replicate cluster; these replicate clusters serve as the units of inference in the GEE with robust SEs.

https://doi.org/10.1038/s43587-026-01204-0

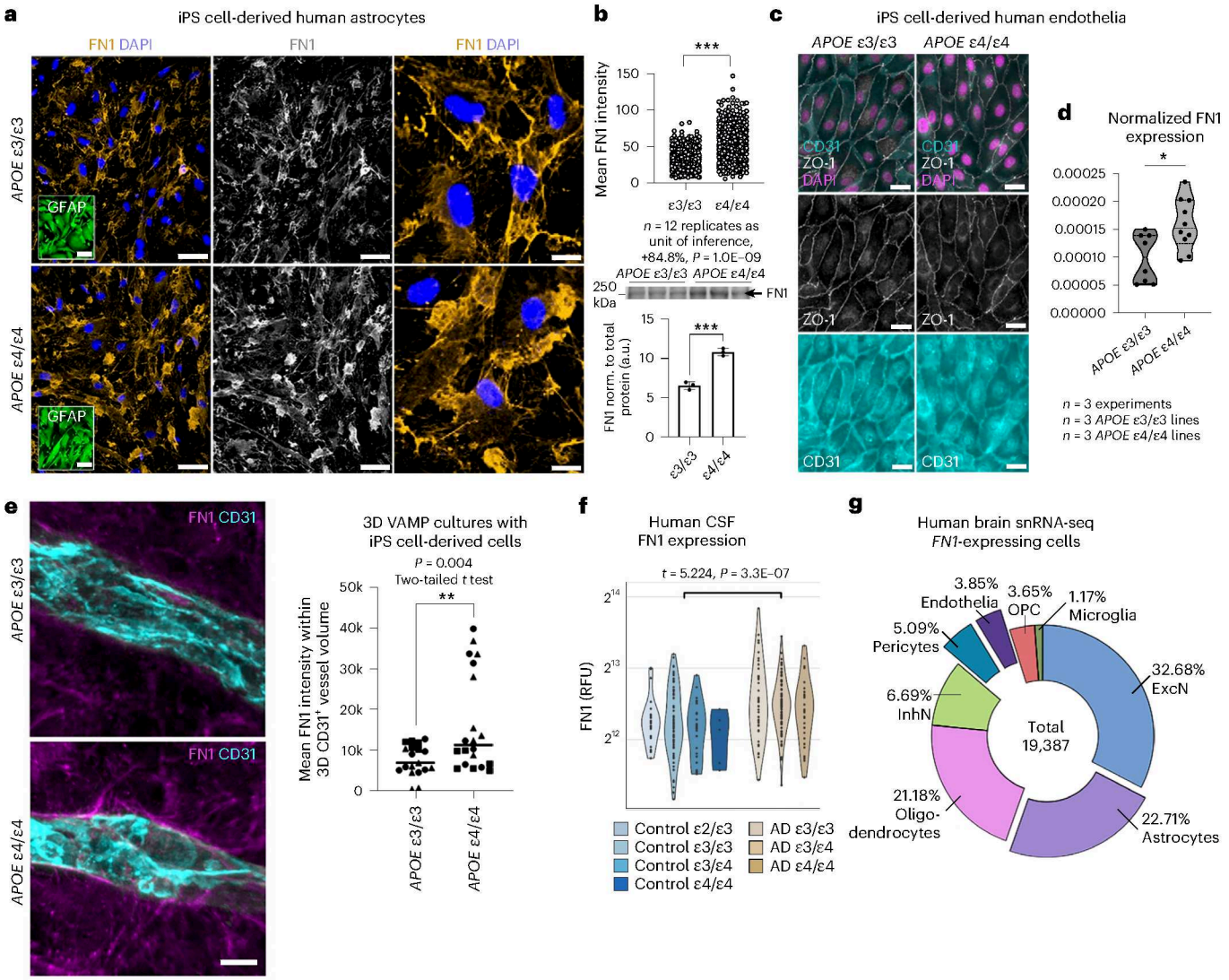

https://doi.org/10.1038/s43587-026-01204-0

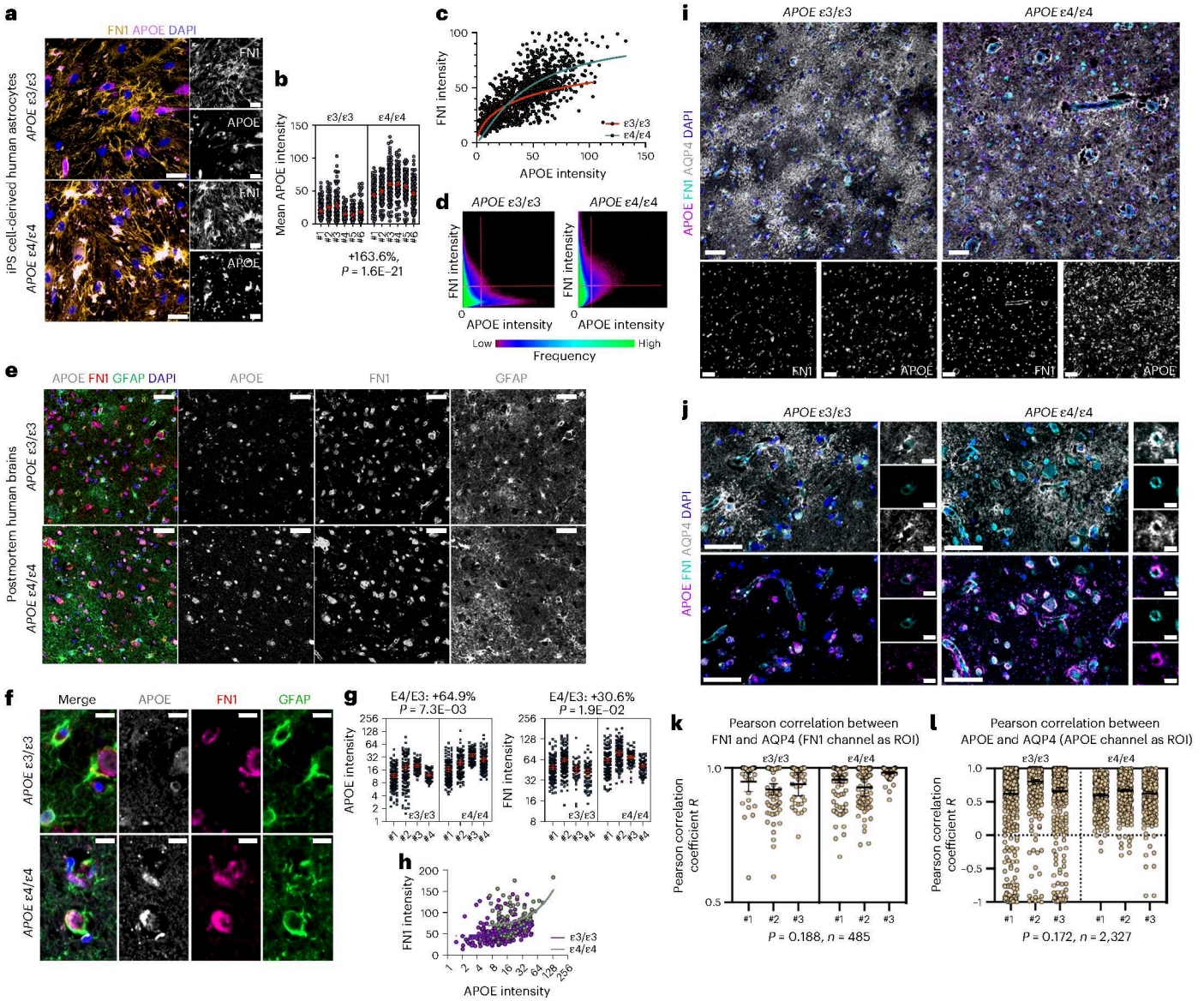

Fig. 3 | FN1 colocalizes with APOE4. **a**, Immunofluorescence staining for FN1 and APOE with DAPI counterstain (blue) in *APOE* ε3/ε3 and *APOE* ε4/ε4 isogenic iPS cell-derived human astrocytes. Single channels in white show FN1 and APOE. **b**, Quantification of APOE protein intensity in extracellular locations. Each data point represents one independent biological replicate (well). $n = 6$ independent biological replicates. Data are presented as mean ± s.e.m. Statistical test: replicate-clustered GEE (two-sided). **c**, Correlation graph for APOE and FN1 intensities in *APOE* ε3/ε3 and *APOE* ε4/ε4 astrocytes. **d**, Colocalization histogram for APOE and FN1. The upper right quadrant shows colocalization, which is enriched in *APOE* ε4/ε4. **e**, Immunofluorescence staining for FN1, APOE and GFAP with DAPI counterstain in *APOE* ε3/ε3 and *APOE* ε4/ε4 postmortem human brain samples from AD cases. Single channels in white show FN1, APOE and GFAP individually. **f**, High-magnification views from a smaller region of the brains shown in **e**, illustrating colocalization of APOE and FN1 at the GFAP-enwrapped BBB predominantly in the *APOE* ε4/ε4 case. **g**, Quantification of APOE and FN1 intensities in human brains. Measurements were obtained from $n = 4$ *APOE* ε3/ε3 AD donors and $n = 4$ *APOE* ε4/ε4 AD donors. Multiple ROIs were analyzed per donor, and statistical inference was performed at the donor level using GEEs (two-sided). Data are presented as mean ± s.e.m. **h**, Correlation graph for APOE and FN1 intensities in *APOE* ε3/ε3 and *APOE* ε4/ε4 AD cases. **i**, Representative confocal images of cortical tissue from *APOE* ε3/ε3 and *APOE* ε4/ε4 individuals, stained for APOE, FN1, AQP4 and DAPI. Bottom panels show single-channel images for FN1 and APOE. **j**, Higher-magnification images from the same samples showing perivascular localization of AQP4, FN1 and APOE, with DAPI-labeled nuclei. Insets show single-channel views of one vessel. **k**, Quantification of Pearson correlation coefficients between FN1 and AQP4, using FN1-positive ROIs. Measurements were obtained from $n = 4$ *APOE* ε3/ε3 AD donors and $n = 4$ *APOE* ε4/ε4 AD donors. Each data point represents one ROI. Multiple ROIs were analyzed per donor, and statistical inference was performed at the donor level using GEEs (two-sided). Data are presented as mean ± s.e.m. High correlation was observed in individual groups, but no significant difference in FN1–AQP4 colocalization was found between APOE genotypes. **l**, Quantification of Pearson correlation coefficients between APOE and AQP4, using APOE-positive ROIs. Colocalization levels were variable but not significantly different between the *APOE* ε3/ε3 and *APOE* ε4/ε4 groups. Data are presented as mean ± s.e.m. (donor-clustered GEE, two-sided). Scale bars, 25 µm (**a**), 50 µm (**e**, **i**, **j**), 5 µm (insets in **j**) and 15 µm (**f**). Data are represented as dot plots or multivariable graphs, and statistical significance is noted as NS, with the precise *P* value, or as $^{*}P < 0.05$, $^{**}P < 0.005$, $^{***}P < 0.001$ and $^{****}P < 0.0001$. No comparison indicates no significant differences in **k** and **l**. Each data point in the graphs is an individual measurement nested within a replicate cluster; these replicate clusters serve as the units of inference in the GEE with robust SEs.

AQP4 than APOE3 (Fig. 3l), indicating preferential accumulation at astrocytic endfeet in *APOE* ε4 brains.

To test whether APOE and FN1 interact directly, we immunoprecipitated FN1 from conditioned media and lysates of iPS cell-derived astrocytes (Extended Data Fig. 3f,g). FN1 was efficiently immunoprecipitated, but APOE was not detected in the FN1 immunoprecipitates, indicating no detectable direct interaction under these experimental conditions. These data do not support a direct FN1–APOE interaction under the experimental conditions used, but they do not exclude indirect associations or technical factors that may have prevented the detection of such interactions.

Inflammation enhances fibronectin deposition

The *APOE* ε4 allele promotes both fibronectin deposition and vascular injury, which are associated with inflammation[29–31]. Because *APOE* ε4 and brain amyloidosis amplify inflammation[19,31,32] and are linked to ECM remodeling during tissue repair[9,33], we investigated whether inflammation mediates *APOE* ε4-dependent fibronectin deposition. We used primary human astrocyte (pHA) cultures[34–37] embedded in a starPEG–heparin hydrogel system to model inflammation and recapitulate key features of the brain microenvironment, including fibronectin- and laminin-rich ECM structures and astroglia–neuron networks[34,37]. Tumor necrosis factor (TNF) induced reactive astrocytic states, nuclear factor-κB (NF-κB) signaling and FN1 expression (Fig. 4 and Extended Data Fig. 4a–f), whereas interleukin-4 (IL-4) reversed these effects (Fig. 4a–c). Because pHAs express TNF and IL-4 receptors[37] and upregulate their expression following TNF treatment (Extended Data Fig. 4g), these findings support direct cytokine regulation of astroglia. Comparison with previous analyses of 3D pHA cultures treated with Aβ42 or kynurenic acid (KYNA)[34,37] showed that TNF significantly increased FN1 expression, whereas IL-4 reduced fibronectin levels both on its own and following TNF or Aβ42 treatment (Fig. 4d). Likewise, TNF and IL-1β increased FN1 expression in induced pluripotent stem cell (iPS cell)-derived endothelial cells (Extended Data Fig. 4h), supporting inflammatory regulation of fibronectin in both astrocytes and endothelial cells.

We next analyzed snRNA-seq data from 1.64 million nuclei across 424 dorsolateral prefrontal cortex samples from the Religious Orders Study and Memory and Aging Project (ROSMAP)[38]. Fibronectin was associated with pathological AD, particularly in astrocyte cluster 5 (β: 0.0300, standard error (SE): 0.0057, false discovery rate (FDR) P: 1.55×10^{-6}), characterized by inflammation, gliosis and SERPINA3 expression (Fig. 4e). SERPINA3 is a reactive astrocyte marker[38] that was likewise upregulated in TNF-treated 3D astrocytes (Fig. 4c). Postmortem immunolabeling confirmed fibronectin upregulation in reactive astrocytes, with FN1 intensity strongly correlating with GFAP intensity (Spearman $r = 0.9177$, $P < 1.0 \times 10^{-15}$; Fig. 4f, $n = 3$). Label transfer from the ROSMAP snRNA-seq dataset[38] to our independent snRNA-seq dataset[28] further showed that reactive astrocyte subcluster 5 expressed FN1 in the highest proportion of cells (Extended Data Fig. 5a), confirming that reactive astrocytes are a major source of FN1.

We validated these findings in vivo using a zebrafish model, where TNF induced fibronectin deposition around astroglia concomitant with NF-κB activation (Fig. 4g–i and Extended Data Fig. 5b–o). Camptothecin and Torin2, which promote anti-inflammatory states by modulating microglial polarization[39], rescued amyloid-induced fibronectin deposition and astrocytic hypertrophy at the gliovascular interface in a zebrafish model of amyloid-mediated fibronectin deposition[12,14,35,36,39–46], marked by increased astrocytic glutamine synthetase (GS) levels (Fig. 4j,k and Extended Data Fig. 5o). Analysis of ROSMAP human brain single-cell RNA-sequencing (scRNA-seq) data showed increased astrocytic NF-κB1 expression in AD, with a stronger effect in *APOE* ε4 carriers ($P < 0.0001$) (Fig. 4l). NF-κB2 expression also strongly predicted FN1 levels in astrocytes ($\beta \approx 0.44$, $P = 2.4 \times 10^{-21}$; Fig. 4m), consistent with the findings in zebrafish. Together, these results identify inflammation as a major driver of fibronectin deposition and astrocyte reactivity[11].

Fibronectin attenuates the VEGF/HB-EGF/IGF-1 signaling cascade

Having found that inflammatory states enhance fibronectin deposition, particularly at astrocytic endfeet where APOE4 accumulates, we next investigated whether elevated fibronectin could perturb BBB signaling cascades essential for vascular homeostasis. To investigate the potential downstream effects of increased fibronectin, we performed single-cell transcriptomics in *fn1b* knockout zebrafish (*fn1b*$^{-/-}$)[47], which blocks the upregulation of fibronectin after Aβ42 exposure (Fig. 5a,b)[12]. We performed differential gene expression and Kyoto Encyclopedia of Genes

Fig. 4 | Inflammation enhances fibronectin production in reactive astrocytes. **a**, Schematic of culture and treatment conditions for bulk RNA sequencing in 3D pHA cultures. **b**, RNA read numbers for selected TNF downstream genes (*TNFRSF1B*, *C3*, *CCL5* and *SAA1*) in TNF-treated pHA cultures. Each data point represents an independent 3D hydrogel culture. Measurements were obtained from $n = 3$ independent biological replicates. Data are presented as mean ± s.e.m. Statistical test: two-tailed unpaired t test. **c**, Heat map of differential expression of selected TNF targets and reactive astrocyte markers in TNF versus control and TNF + IL-4 versus control 3D pHA cultures. FC, fold change. **d**, Heat map of differential expression of *FN1* under several toxicity conditions in 3D pHA cultures. KYNA, Aβ42 and Aβ42 + IL-4 from ref. 37. Statistical test: negative binomial generalized linear model, two-sided Wald test, Benjamini–Hochberg FDR. **e**, Analysis of the association of *FN1* with human AD traits in ROSMAP cohort astrocyte clusters positively associates *FN1* with reactive astrocyte cluster 5 (Ast.5). DLPFC, dorsolateral prefrontal cortex. **f**, (1) Immunostaining for GFAP and FN1 with DAPI counterstain in control and AD postmortem human brains; (2, 3) quantification of FN1 (2) and GFAP (3) intensities in masked astrocytes in control versus AD cases ($n = 3$ for each group); (4) correlation of FN1 and GFAP intensities in sampled astrocytes from the control and AD groups ($n = 120$). Measurements were obtained from $n = 3$ independent donors per group. Multiple astrocytes were quantified per donor, and statistical analyses were performed with a two-tailed Kolmogorov–Smirnov test (FN1: $P = 2.48 \times 10^{-33}$; GFAP: $P = 1.70 \times 10^{-28}$). **g**, Immunofluorescence staining for GS, FN1 and NF-κB:GFP in control and TNF-injected zebrafish brains. Smaller panels show individual color-coded channels. **h**, Quantification of GFP and FN1 intensities. Each data point represents one gliovascular contact point. Measurements were obtained from $n = 4$ independent animals per group. Multiple measurements were obtained per animal, and statistical inference was performed at the animal level using GEEs (two-sided). Data are presented as mean ± s.e.m. **i**, Interaction graph for NF-κB:GFP and FN1 levels. Statistical test: simple linear regression, Pearson correlation coefficient. **j**, Immunostaining for GS and FN1 with DAPI counterstain in control, Aβ42-injected, Aβ42 + camptothecin-injected and Aβ42 + Torin-injected zebrafish brains. Images highlight the dorsoventral vascular hub. Insets: FN1 channel alone. **k**, Quantification graph for FN1 and GS intensities normalized to DAPI. Every data point represents an independent gliovascular contact point, and statistical inference was performed at the level of the individual animals. Statistical test: animal-clustered GEE (two-sided). Scale bars, 10 µm (**f**) and 25 µm (**g**, **j**). **l**, Donor-level distributions of NF-κB1 expression in astrocytes from the ROSMAP dataset, stratified by AD diagnosis (control versus AD) and *APOE* ε4 carrier status. MCI, mild cognitive impairment. A significant upregulation of NF-κB1 was observed in AD, with a stronger effect in *APOE* ε4 carriers ($P < 0.0001$). Statistical test: two-sided Wald test from multivariable linear regression models adjusting for relevant demographic and technical covariates, followed by pairwise comparisons between diagnostic groups. **m**, Scatter plot showing a positive correlation between NF-κB2 and FN1 expression ($\beta \approx 0.44$, $P = 2.4 \times 10^{-21}$) in human astrocytes. Data are presented as mean ± s.e.m. Quantitative data in the graphs are represented as dot plots, and statistical significance is noted as NS, with the precise P value where applicable, or as $^{*}P < 0.05$, $^{**}P < 0.005$, $^{***}P < 0.001$ and $^{****}P < 0.0001$. ND, no statistical difference. GEE P values are provided in Supplementary Table 1. Each data point in the graphs is an individual measurement nested within a replicate cluster; these replicate clusters serve as the units of inference in the GEE.

https://doi.org/10.1038/s43587-026-01204-0

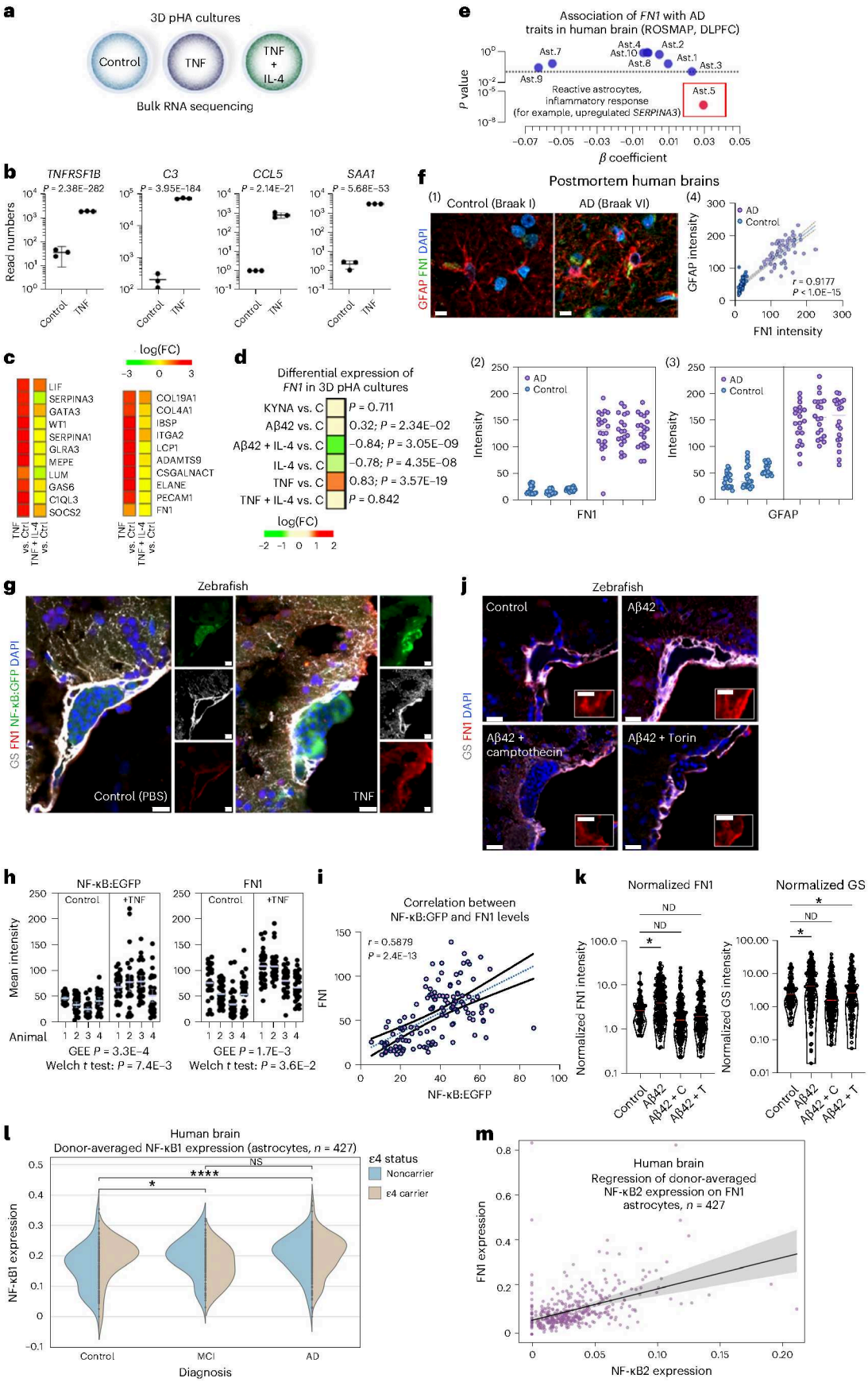

https://doi.org/10.1038/s43587-026-01204-0

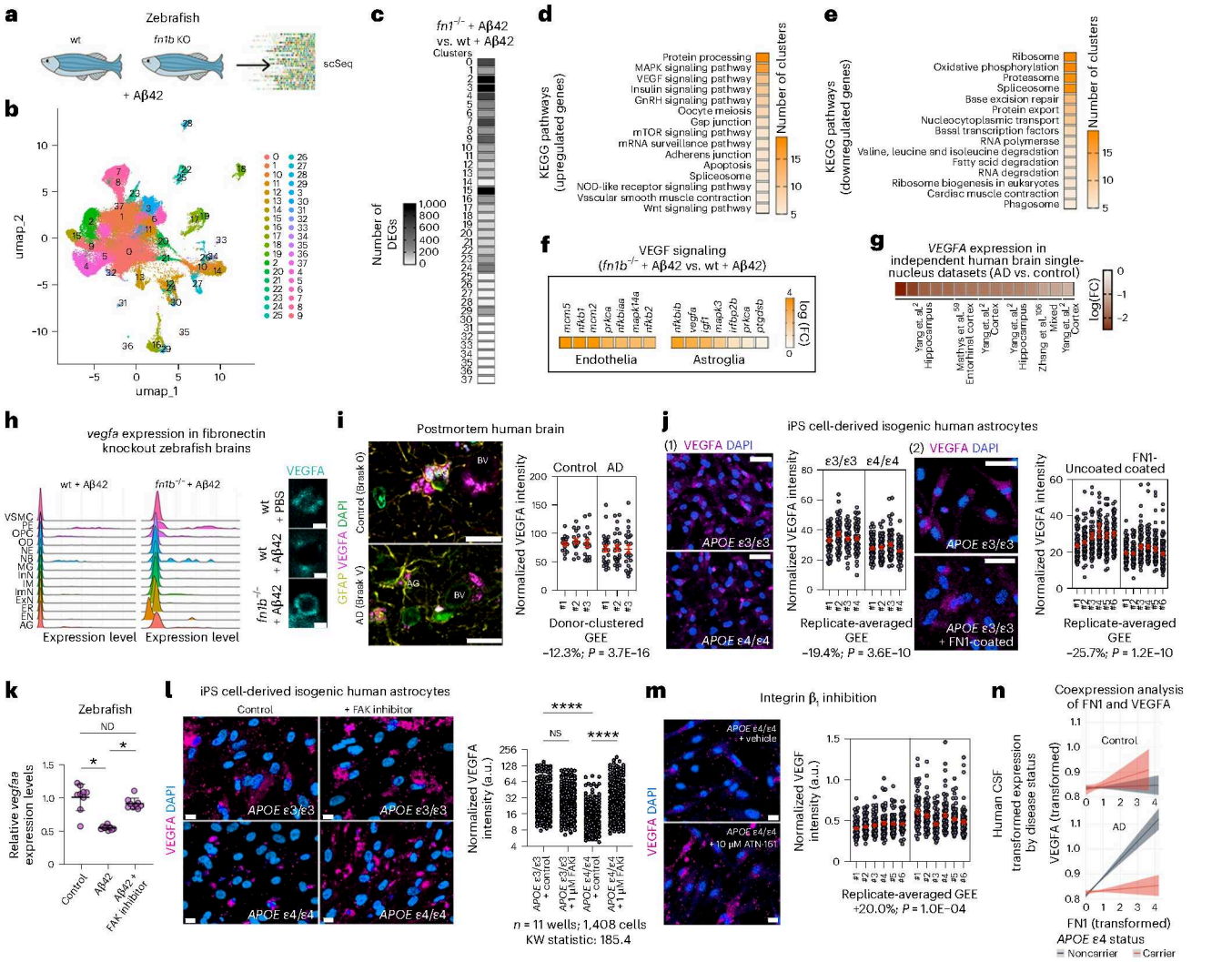

Fig. 5 | Fibronectin suppresses VEGF signaling. a, Schematic of single-cell sequencing (scSeq) comparison in wild-type (wt) control and *fn1b* homozygous knockout (KO; *fn1b*$^{-/-}$) zebrafish, both after Aβ42 treatment. **b**, UMAP plot of 38 identified cell clusters. **c**, Heat map showing the number of DEGs in each cluster. **d**,**e**, Heat maps showing the number of times a certain KEGG pathway identifier is enriched in the identified clusters. Upregulated (**d**) and downregulated (**e**) genes were analyzed separately and depicted with individual heat maps. GnRH, gonadotropin-releasing hormone. **f**, Selected top DEGs within the VEGF signaling-related KEGG pathway in endothelial cells and astrocytes. **g**, *VEGFA* expression changes in publicly available human single-nucleus datasets from control and AD human brains (from refs. 2,24,53,100). **h**, Ridge plots of *vegfa* expression (left) and representative VEGFA immunofluorescence staining (right) in wild-type + Aβ42 and *fn1b*$^{-/-}$ + Aβ42 zebrafish brains. Astrocytes increase *vegfa* expression upon *fn1b* loss of function. AG, astrocyte; VSMC, vascular smooth muscle cell; PE, pericyte; OD, oligodendrocyte; NB, neuroblast; NE, neuron; MG, microglia; InN, inhibitory neuron; ExN, excitatory neuron; IM, immune cell; ImN, immature neuron; ER, erythroid cell; EN, endothelia. Data are presented as mean ± s.e.m. **i**, Left: immunofluorescence staining for VEGFA and GFAP with DAPI counterstain in control and AD postmortem human brains, showing reduced VEGFA in AG and around the blood vessels (BV). Right: quantification of VEGF intensity. Measurements were obtained from $n = 3$ independent zebrafish per group. Statistical inference was performed at the animal level using GEEs (two-sided). Data are presented as mean ± s.e.m. **j**, (1) VEGFA protein in *APOE* ε3/ε3 and *APOE* ε4/ε4 iPS cell-derived human astrocytes (left), and quantification of VEGFA protein intensity (right). Each data point represents one cell. Statistical analyses were performed using two-sided replicate-averaged GEE, with $n = 4$ biological replicates as the unit of inference. Data are presented as mean ± s.e.m. (2) VEGFA protein in *APOE* ε3/ε3 iPS cell-derived human astrocytes in the absence and presence of fibronectin coating on the plates (left), and quantification of VEGFA protein intensity (right). Each data point represents one cell. Statistical analyses were performed using replicate-averaged GEE, with $n = 6$ biological replicates as the unit of inference. Data are presented as mean ± s.e.m. **k**, RT–qPCR for *vegfaa* in control, Aβ42-injected and Aβ42 + FAK inhibitor-injected zebrafish brains. Measurements were obtained from $n = 9$ independent replicates per group. Data are presented as mean ± s.e.m. Statistical test: Kruskal–Wallis with the two-stage step-up procedure of Benjamini, Krieger and Yekutieli (control versus Aβ42: $P < 0.001$; Aβ42 versus Aβ42 + FAK inhibitor: $P = 0.0022$). **l**, VEGFA immunofluorescence in isogenic *APOE* ε3/ε3 and *APOE* ε4/ε4 human iPS cell-derived astrocytes in the presence or absence of treatment with the FAK inhibitor PF-573228 (left), and quantification of VEGFA protein intensity (right). Data are presented as mean ± s.e.m. KW, Kruskal–Wallis; FAKi, FAK inhibitor. **m**, VEGFA immunofluorescence in *APOE* ε4/ε4 human iPS cell-derived astrocytes after treatment with the β-integrin blocker ATN-161 (left), and quantification of VEGFA protein intensity (right). Each data point represents one independent biological replicate. Statistical analyses were performed using $n = 6$ biological replicates and two-sided replicate-clustered GEE. Data are presented as mean ± s.e.m. **n**, Pseudolog-transformed coexpression analysis of FN1 (*x* axis) and VEGFA (*y* axis) in astrocytes, stratified by disease status (control versus AD) and *APOE* ε4 status (noncarrier versus ε4 carrier). Points represent single-cell data. Each panel displays a fitted linear regression (solid line) with 95% confidence intervals (shaded area). The strong main effect of FN1 on VEGFA expression ($F = 26.39$, $P = 2.79 \times 10^{-7}$) and the significant three-way interaction among FN1, *APOE* ε4 status and disease status ($F = 14.02$, $P = 1.81 \times 10^{-4}$) demonstrate genotype- and disease-specific patterns of coregulation. Statistical test: two-sided Wald test. Scale bars, 5 μm (**h**), 10 μm (**i**, **m**) and 25 μm (**i**, **j**). Data are represented as dot plots or multivariable graphs, and statistical significance is noted as NS, with the precise *P* value, or as $^{*}P < 0.05$, $^{**}P < 0.005$, $^{***}P < 0.001$ and $^{****}P < 0.0001$. Each data point in the graphs is an individual measurement nested within a replicate cluster; these replicate clusters serve as the units of inference in the GEE.

https://doi.org/10.1038/s43587-026-01204-0

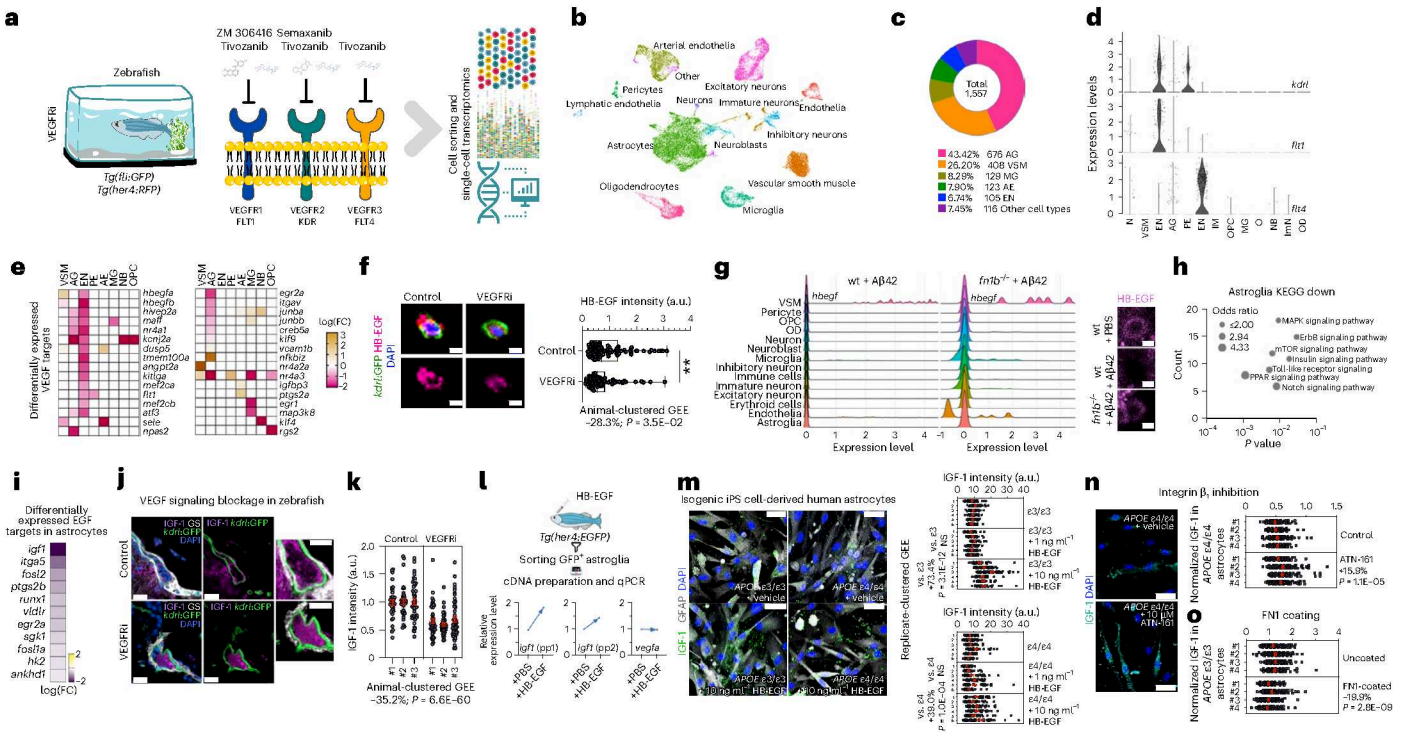

Fig. 6 | VEGF signaling is required for HB-EGF expression and subsequent IGF-1 induction. a, Schematic of the VEGFRi study and subsequent single-cell transcriptomics in the double reporter zebrafish line *Tg(fli1a:EGFP)*[61] and *Tg(her4:RFP)*[62], marking endothelial cells and astrocytes, respectively. **b**, UMAP of the identified cell types. **c**, Distribution of DEGs among cell types. **d**, Violin plots showing the expression of the VEGFRs *kdrl*, *flt1* and *flt4* in cell types. **e**, Heat map of differential expression of selected VEGF target genes in major cell types from **b** and **c**. AE, arterial endothelia; VSM, vascular smooth muscle; N, neuron; O, other. **f**, Immunostaining for HB-EGF and *kdrl*:GFP with DAPI counterstain in control and VEGFRi zebrafish brains showing single vasculature (left), along with a quantification graph for HB-EGF (right). VEGFRi reduces HB-EGF levels. Each data point represents one gliovascular contact point. Measurements were obtained from $n = 4$ independent animals per group. Multiple contact points were analyzed per animal, and statistical inference was performed at the animal level using GEEs (two-sided). Violin plots show the data distribution; the center line indicates the median; the box represents the interquartile range (25th–75th percentile); whiskers extend to the minimum and maximum values; points represent individual observations. **g**, Left: ridge plot for *hbegf* expression in control + Aβ42 and *fn1b*$^{-/-}$ + Aβ42 zebrafish brains indicating upregulation in endothelia. Right: immunostaining for HB-EGF. **h**, Multivariable graph for downregulated pathways in astrocytes, showing enrichment of MAPK, ErbB, mTOR and insulin signaling pathways. PPAR, peroxisome proliferator-activated receptor. **i**, Heat map showing differential expression of selected EGF target genes in astrocytes after VEGFRi. **j**, Immunofluorescence staining for IGF-1, GS and *kdrl*:GFP with DAPI counterstain in control and VEGFRi zebrafish brains. **k**, Quantification of IGF-1 levels. Each data point represents one gliovascular contact point analyzed with animals as the unit of inference ($n = 3$ per group). Data are presented as mean ± s.e.m. Statistical test: two-sided animal-clustered GEE. **l**, RT–qPCR scheme showing sorting of *her4*:EGFP-positive astrocytes after HB-EGF injection, which increases *igf1* expression as determined by two primer pairs (pp), while *vegfa* expression remains unchanged in the adult zebrafish brain (reference gene: β-actin). **m**, Left: immunocytochemistry for IGF-1 and GFAP with DAPI counterstain in *APOE* ε3/ε3 and *APOE* ε4/ε4 isogenic astrocytes with and without 10 ng ml^{-1} HB-EGF treatment. Right: quantification of IGF-1 intensity normalized to cell number. Each data point represents one cell. $n = 6$ independent biological replicates with multiple data points. Data are presented as mean ± s.e.m. Statistical test: two-sided, replicate-clustered GEE. **n**, Immunostaining for IGF-1 in *APOE* ε4/ε4 astrocytes with and without ATN-161 treatment (left), along with quantification per cell (right). **o**, Quantification of IGF-1 in *APOE* ε3/ε3 astrocytes with and without fibronectin coating of the wells. Each data point represents one cell. $n = 4$ independent biological replicates with multiple data points. Data are presented as mean ± s.e.m. Statistical test: two-sided animal-clustered GEE. Scale bars, 5 µm (**f**, **g**) and 25 µm (**j**, **m**, **n**). Data are represented as dot plots or multivariable graphs, and statistical significance is noted as NS, with the precise *P* value, or as $^{*}P < 0.05$, $^{**}P < 0.005$, $^{***}P < 0.001$ and $^{****}P < 0.0001$. Each data point in the graphs is an individual measurement nested within a replicate cluster; these replicate clusters serve as the units of inference in the GEE with robust SEs.

and Genomes (KEGG) pathway analyses across 32,294 cells in 38 clusters by comparing cells from wild-type (+Aβ42) and *fn1b*$^{-/-}$ (+Aβ42) zebrafish (Fig. 5c–e and Extended Data Fig. 6). We identified significant enrichment of vascular endothelial growth factor (VEGF) ($P = 3.8 \times 10^{-2}$, odds ratio (OR) = 2.87) and insulin pathways ($P = 4.3 \times 10^{-3}$, OR = 35.78), mediated by MAPK signaling ($P = 4.0 \times 10^{-5}$, OR = 3.41) (Fig. 5d,e). We show that fibronectin modulates VEGF and insulin signaling by altering ECM activity.

VEGF signaling is essential for BBB integrity and vascular–astrocytic communication, and its disruption in AD contributes to BBB breakdown[1,40,48–50]. We hypothesized that reduced VEGF signaling mediates the pathological effects of fibronectin. Astrocytes in *fn1b* knockout zebrafish upregulated the NF-κB inhibitor *nfkbib*[51], the VEGF ligand *vegfa*, the insulin growth factor *igf1* and the VEGF signaling inducer *irfbp2b*[22], while *fn1b* knockout endothelia upregulated NF-κB-related genes that potentiate VEGF signaling[52] (Fig. 5f,g). These findings are consistent with those in the human AD brain, where single-nucleus transcriptomics showed that astrocytic VEGFA is reduced in AD (Extended Data Fig. 7a,b)[2,24,53–57]. We found that *vegfa* expression increased in *fn1b*$^{-/-}$ zebrafish brains (Fig. 5h). VEGFA protein levels were significantly reduced in AD brains compared to control brains (−12.3%, $P = 3.7 \times 10^{-16}$) (Fig. 5i) and in *APOE* ε4/ε4 compared to *APOE* ε3/ε3 iPS cell-derived astrocytes (−19.4%, $P = 3.6 \times 10^{-10}$) (Fig. 5j). Culturing *APOE* ε3/ε3 astrocytes on fibronectin-coated plates also significantly reduced VEGFA levels (−25.7%, $P = 1.2 \times 10^{-10}$), recapitulating the effects of *APOE* ε4/ε4 on astrocytic VEGFA (Fig. 5j). We show that fibronectin modulates VEGF and insulin signaling by altering ECM activity, linking inflammatory remodeling of the vascular niche to impaired trophic signaling at the BBB.

Fibronectin binds integrins[11,58] that are expressed on astrocytes (Extended Data Fig. 7c). We tested the hypothesis that inhibition of focal adhesion kinase (FAK), an intracellular mediator of the integrin signaling cascade[59], could restore VEGFA expression by treating zebrafish with the selective FAK inhibitor PF-573228 (ref. 59). This restored VEGFA expression under Aβ42 conditions (Fig. 5k). Similarly, blocking FAK with PF-573228 in isogenic *APOE* ε3/ε3 and *APOE* ε4/ε4 iPS cell-derived astrocytes restored the reduced VEGFA levels in *APOE* ε4/ε4 astrocytes (Fig. 5l). Treatment with ATN-161, an independent β-integrin blocker, resulted in a similarly significant upregulation of VEGFA in *APOE* ε4/ε4 astrocytes (+20.0%, $P = 1.0 \times 10^{-4}$) (Fig. 5m), validating the relationship between integrin signaling and fibronectin-mediated alteration of VEGFA in astrocytes.

To examine the relationship between fibronectin and VEGFA protein levels in humans, we performed transformed gene coexpression analyses in human CSF from AD and control brains (Fig. 5n). FN1 expression was strongly associated with VEGFA levels ($F = 26.39$, $P = 2.79 \times 10^{-7}$), and a significant three-way interaction among *FN1*, *APOE* ε4 status and disease status ($F = 14.02$, $P = 1.81 \times 10^{-4}$) indicated that the slope of the FN1–VEGFA relationship differs in *APOE* ε4 carriers with AD compared to noncarriers and controls. In controls, VEGFA expression levels were similar between *APOE* ε3 and *APOE* ε4 carriers, whereas in AD brains, non-ε4 carriers exhibited a compensatory increase that was absent in *APOE* ε4 carriers. To determine whether the FN1–VEGFA relationship observed in CSF extends beyond the central nervous system (CNS), we analyzed plasma protein levels in 113 individuals from another cohort[12,60] (Extended Data Fig. 7d). Unlike in CSF, plasma FN1 did not correlate with VEGFA (Pearson $r = 0.13$; $R^2 = 0.018$) (Extended Data Fig. 7e), indicating that the FN1–VEGFA association is CNS-specific and varies according to the *APOE* genotype in AD.

To investigate the downstream mechanisms of the FN1/VEGF signaling axis, we used double-transgenic zebrafish (*Tg(fli1a:EGFP)*, *Tg(her4.1:RFP)*)[61,62]—marking cerebrovascular endothelial cells (green) and astrocytes (red) with fluorescent reporters—and inhibited VEGF signaling using VEGF receptor (VEGFR) inhibitors (tivozanib, ZM 306416 and semaxanib). Single-cell transcriptomics of 22,712 sorted cells (17% endothelial cells, 39.2% astrocytes) identified 1,557 differentially expressed genes (DEGs) (Fig. 6a–c and Extended Data Fig. 8). To identify potential genes proximally regulated by VEGF signaling, we analyzed previously documented VEGF target genes[63,64] among the DEGs. We found that VEGFR inhibition (VEGFRi) significantly downregulated endothelial *hbegf* isoforms, as validated in *kdrl*:GFP zebrafish, a fluorescent reporter for endothelia (−28.3%, $P = 3.5 \times 10^{-2}$) (Fig. 6e,f). This is consistent with the upregulation of *hbegf* in *fn1b* knockout, validated by single-cell sequencing and tissue immunolabeling (Fig. 6g), and indicates that reduced endothelial heparin-binding EGF-like growth factor (HB-EGF) expression downstream of FN1/VEGF signaling also contributes to BBB pathology.

HB-EGF, upon binding to the EGF receptor (ERBB1), regulates inflammation, neurogenesis and astrocyte maturation through MAPK and ERBB1 signaling[65–67]. Thus, fibronectin-dependent reduction of HB-EGF may alter astrocytes in the gliovascular niche. VEGFRi in zebrafish revealed downregulated MAPK, ERBB and insulin pathways, reflecting changes observed in *fn1b* knockout (Fig. 6h). Notably, known EGF targets[68,69], including *igf1*, were significantly reduced (Fig. 6i), a finding further confirmed by immunolabeling and quantification (−35.2%, $P = 6.6 \times 10^{-60}$) (Fig. 6j,k) and independent human brain single-nucleus datasets[28,70]. HB-EGF induced *igf1* expression without affecting *vegfa* levels (Fig. 6l), and in human iPS cell-derived astrocytes, insulin-like growth factor 1 (IGF-1) expression was significantly increased by HB-EGF in a dose-dependent manner in both isogenic *APOE* ε3 and *APOE* ε4 astrocytes (*APOE* ε3: +73.4%, $P = 3.1 \times 10^{-12}$; *APOE* ε4: +39.0%, $P = 1.0 \times 10^{-4}$) (Fig. 6m), indicating that HB-EGF is upstream of IGF-1. To determine whether IGF-1 expression in astrocytes is integrin-dependent, we treated *APOE* ε4 astrocytes with the β-integrin blocker ATN-161 and observed significantly upregulated IGF-1 protein (+15.9%, $P = 1.1 \times 10^{-5}$) (Fig. 6n). Conversely, *APOE* ε3/ε3 astrocytes showed significantly reduced IGF-1 levels when the culture wells were coated with fibronectin (−19.9%, $P = 2.8 \times 10^{-9}$), recapitulating the effects of the *APOE* ε4/ε4 genotype on IGF-1 levels in astrocytes (Fig. 6o).

As IGF-1 is crucial for BBB function[71–73], these findings indicate that the FN1/VEGF/HB-EGF/IGF-1 signaling axis regulates gliovascular homeostasis, which is disrupted in AD through *APOE* ε4-dependent elevated fibronectin deposition. To assess whether HB-EGF and IGF-1 could reverse fibronectin-mediated VEGF reduction and BBB damage, we analyzed the gliovascular structure and tight junctions in VEGFR inhibitor-treated zebrafish with or without ectopic HB-EGF/IGF-1. VEGFRi compromised endothelial integrity, as ZO-1/GFP colocalization was significantly reduced (Fig. 7a,b; analyses were performed on parenchymal capillary vessels rather than larger arterial structures), consistent with previous findings[40,49]. In contrast, HB-EGF/IGF-1 treatment restored tight junction levels (Fig. 7b).

Gliovascular interactions, vital for BBB and brain homeostasis[5,6,74,75], are disrupted early in AD[2,4,12,20,25,76]. By investigating the evolutionary conservation of the VEGFA/HB-EGF/IGF-1 signaling axis, we observed reduced levels of VEGFA, HB-EGF and IGF-1 in zebrafish, APP knock-in mice and human AD brains (Fig. 7c–e). AD brains with Braak stage V–VI, representing advanced AD pathology characterized by extensive neurofibrillary tangles in the neocortex and substantial cognitive decline[77], also show significant alterations in VEGFA, HB-EGF and IGF-1 (Fig. 7d–f), mirroring fibronectin-induced VEGFR/HB-EGF/IGF-1 signaling disruption. To further validate the downstream effects of fibronectin and *APOE* ε4, we performed KEGG pathway analysis and *FN1–APOE* ε4 interaction modeling from single-cell endothelial transcriptomics in ROSMAP human brains (Fig. 7g). Donor-level expression analysis

Fig. 7 | Conserved activities of HB-EGF and IGF-1 regulate gliovascular interactions and endothelial tight junctions. a, Representative images of mCherry-positive parenchymal microvessels (capillary structures) and BLBP (astroglial marker) staining in the zebrafish brain. Images are from three independent experiments with similar results. **b**, Left: immunostaining for GS, *kdrl*:GFP and ZO-1 with DAPI counterstain in control, VEGFR inhibitor-treated and VEGFR inhibitor + IGF-1/HB-EGF-injected zebrafish brains. Right: quantification graph of ZO-1/GFP colocalization, which indicates BBB integrity ($n = 3$ animals per group). Quantification was restricted to small-diameter parenchymal vessels and did not include large pial arteries. Statistical test: two-sided, animal-clustered GEE. **c**, Immunostaining for IGF-1 (red), HB-EGF and VEGFA with DAPI counterstain (blue) in postmortem control (Braak stage I) and AD (Braak stage VI) human brains. Individual channels are shown in white. **d**, Immunofluorescence staining for IGF-1, HB-EGF and VEGFA with DAPI counterstain in wild-type and APP knock-in (APP-KI) mouse models. **e**, Quantification of HB-EGF, IGF-1 and VEGFA intensities in human brains. Statistical test: two-sided Welch's *t* test (HB-EGF and IGF-1: $P < 1.0 \times 10^{-15}$; VEGFA: $P = 9.7 \times 10^{-8}$). **f**, Quantification of HB-EGF, IGF-1 and VEGFA intensities in mouse brains. Statistical test: two-sided Welch's *t* test (HB-EGF: $P = 6.8 \times 10^{-7}$; IGF-1: $P = 0.0099$; VEGFA: $P = 0.016$). **g**, Top 10 enriched KEGG pathways for genes showing a significant FN1 × APOE4 interaction in brain endothelial cells. Bar lengths indicate $-\log_{10}$-transformed FDR values, and bar color corresponds to the number of differentially interacting genes (orange, positive interaction; purple, negative interaction). *p*, index of the gene tested as the outcome variable; HSV1, herpes simplex virus type 1. **h**, Regional plot showing the mQTL (methylation quantitative trait loci) effects of a genetic variant of FN1 (*rs2304573*) on methylation levels of the transcriptional regulatory regions of the human VEGFA locus. The dotted red line indicates statistical significance. Statistical test: two-sided Wald test. Scale bar, 50 μm (**a**), 25 μm (**c**, **d**) and 10 μm (**b**). Data are represented as dot plots or multivariable graphs, and statistical significance is noted as NS, with the precise *P* value where applicable, or as $^{*}P < 0.05$, $^{**}P < 0.005$, $^{***}P < 0.001$ and $^{****}P < 0.0001$.

https://doi.org/10.1038/s43587-026-01204-0

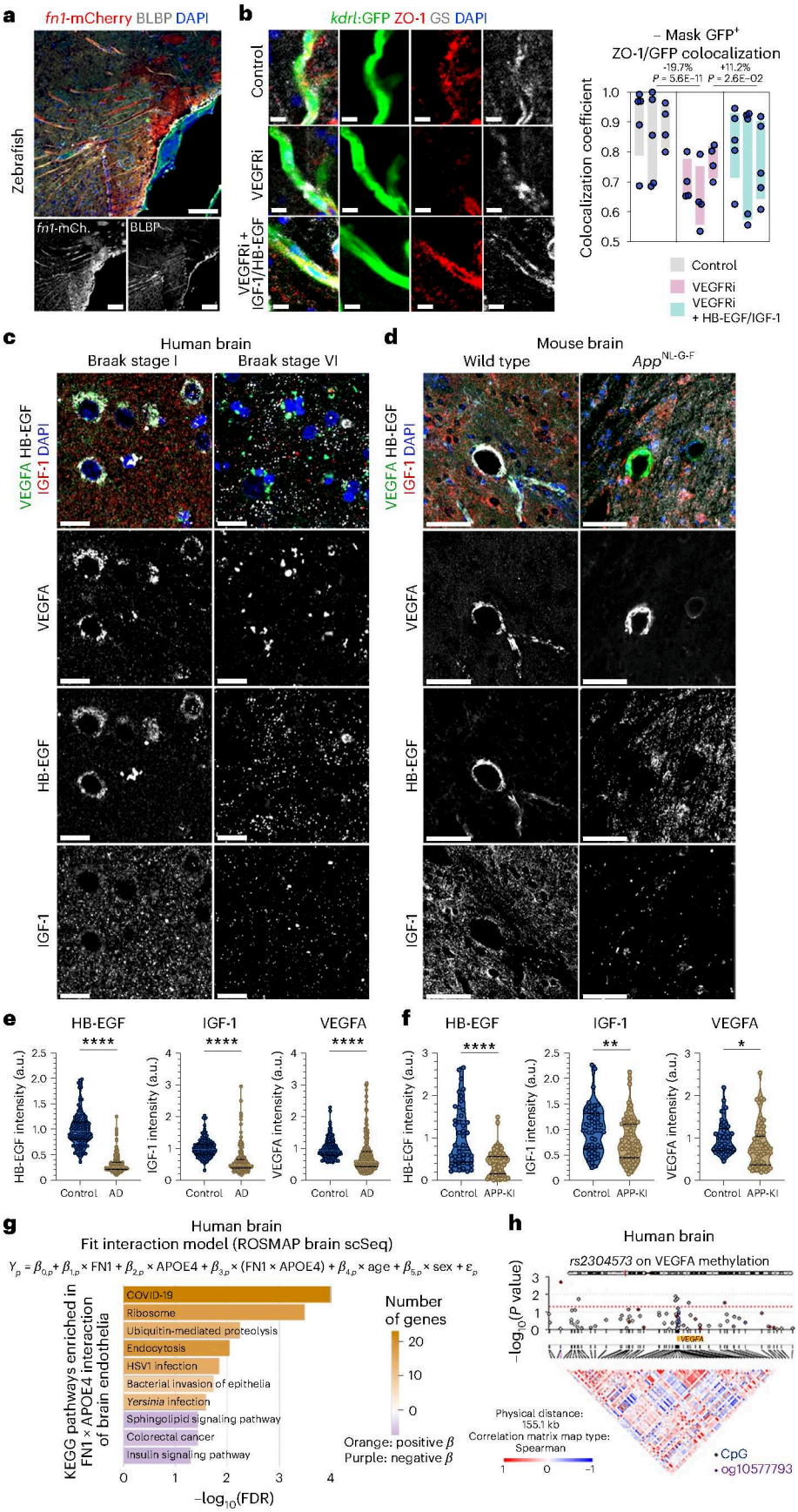

revealed significant interactions between FN1 and *APOE* ε4 status in the vascular endothelium. In particular, multiple genes exhibited robust changes associated with increasing FN1 levels in *APOE* ε4 carriers compared to noncarriers. KEGG enrichment analysis of these interacting genes uncovered distinct pathway signatures, with some pathways enriched among negatively regulated genes (for example, insulin signaling) and others enriched among positively regulated genes (for example, COVID-19 pathways). This mirrors the downregulation of IGF-1 signaling observed in vitro and provides clinical validation of our findings that fibronectin and *APOE* ε4 lead to altered insulin signaling in the gliovascular niche.

To explore the molecular interaction between FN1 and VEGFA expression, we analyzed the available epigenetic datasets and methylation profiles in autopsied AD brains[78]. We found an intronic *FN1* variant linked to altered VEGFA methylation, which supports the transcriptional regulation of VEGFA by fibronectin (Fig. 7h). These findings are consistent with human brain single-nucleus transcriptomics studies[1,2,24,38,53,54,56,57,79,80], which show upregulated *FN1* gene expression and reduced VEGFA/IGF-1 expression in astrocytes (Extended Data Fig. 9a).

Fibronectin induces BBB leakage

Fibronectin accumulation coincided with vascular fibrinogen deposition and localization in astrocytic endfeet. We then tested whether increased fibronectin alone is sufficient to disrupt BBB integrity by overexpressing human FN1 in the astroglia of zebrafish larvae and by generating a *her4.1* promoter-driven FN1-T2A-GFP construct (human FN1 linked to GFP through a T2A self-cleaving peptide) for injection. Control animals injected with empty plasmid or PBS maintained intact vascular dextran–Texas Red confinement and exhibited minimal fibronectin signal or leakage (Extended Data Fig. 9b–e). In contrast, *her4.1*:FN1-T2A-GFP larvae exhibited astroglial GFP expression, elevated fibronectin levels and dextran leakage (Extended Data Fig. 9b–e). These data indicate that astroglial FN1 expression is sufficient to compromise the integrity of the gliovascular barrier.

Discussion

Our findings illustrate the crucial role of fibronectin as a pathological mediator in AD, especially among *APOE* ε4 carriers (Supplementary Fig. 1). By integrating data from postmortem human brains, animal models and iPS cell-derived cultures, we demonstrate that fibronectin deposition contributes to BBB dysfunction through multiple interconnected mechanisms, including aberrant interactions with *APOE* ε4, inflammation-induced upregulation of fibronectin and suppression of growth factor signaling pathways. Our work demonstrates that *APOE* ε4-induced BBB dysfunction in AD is augmented by the pathological deposition of fibronectin. Fibronectin deposition disrupts regulatory signaling cascades at the gliovascular interface, exacerbates vascular dysfunction and neuroinflammatory states, and alters pathways essential for maintaining BBB integrity.

Fibronectin is a key ECM protein with a critical role in tissue repair and remodeling[10,59,81], promoting fibrous tissue deposition and the recruitment of other matrix components to stabilize injured tissues. While essential for peripheral wound healing, excessive fibronectin deposition in the CNS can be detrimental[33,81–84]. Fibronectin accumulation within the gliovascular interface interferes with the critical crosstalk between astrocytes and endothelial cells, leading to impaired clearance of metabolic waste, reduced vascular integrity and exacerbated neuroinflammation. Fibronectin deposition at the BBB, particularly in *APOE* ε4 carriers, is consistent with the broader vascular basement membrane remodeling observed in AD[1,85,86]. Our findings mechanistically link astrocyte-derived fibronectin to altered gliovascular signaling and BBB dysfunction. This conclusion is supported by elevated FN1 levels in the CSF of living individuals with AD, the strong association between fibronectin and inflammatory astrocytic states in human AD brains, and altered VEGFA regulation associated with FN1 variants in postmortem AD brains, highlighting FN1 as both a biomarker candidate and a mechanistic mediator of AD-related BBB dysfunction. The genetic association of FN1 with vascular traits, including stroke and small vessel disease[87] (Supplementary Tables 2–4), further supports its role in cerebrovascular integrity. A recent study[88] also supports the convergence between APOE4 and fibronectin in CVP. Together, these findings establish the upstream mechanism by which astrocyte-derived fibronectin disrupts the BBB, providing a mechanistic basis for the subsequent vascular remodeling observed in AD.

We show links between FN1 activity and VEGF signaling, a pathway critical for maintaining cerebrovascular health and integrity[40,48,63,89]. In AD, astrocytic states transition from maintenance roles to disease-associated reactive states, characterized by the upregulation of reactive markers and the loss of homeostatic genes, including VEGFA[57]. Previously, we showed that VEGFA, predominantly expressed by astrocytes, is significantly downregulated in AD, thereby disrupting gliovascular signaling[40,56]. Clinically, lower VEGFA levels are associated with increased tau pathology, altered cerebral blood flow, BBB dysfunction and impaired cognition[40,48,56,90,91], consistent with the broader finding that astrocytic malfunction in AD compromises BBB integrity[3,5,50]. *APOE* ε4-induced fibronectin activity regulates VEGF, HB-EGF and IGF-1 signaling, representing a prominent pathological mediator of AD at the BBB niche. Consistent with prior studies[72,73], we demonstrated impaired VEGF and IGF-1 signaling in AD by identifying fibronectin as a mediator of these disruptions.

In AD, the accumulation of amyloid and tau reduces IGF-1, which mediates the effects of HB-EGF expression, further promoting AD pathology in the brain (Supplementary Table 5). This suggests a mechanism connecting the combined functions of HB-EGF and IGF-1 with the interaction between astrocytes and endothelial cells to maintain a healthy BBB, thereby promoting homeostatic clearance mechanisms in the perivascular space. Interstitial clearance through the vascular basement membrane, which is primarily formed and regulated by endothelial cells and astrocytes, also has a critical role in AD pathology[92,93]. A previous study showed that HB-EGF, in combination with IGF-1, stimulates astrocyte migration and wound closure, showcasing their synergistic impact on glial behavior during CNS injury repair[94]. HB-EGF and IGF-1 are necessary for functional astrocyte–endothelial interactions that maintain the structural and functional integrity of the gliovascular architecture, supporting homeostatic processes such as amyloid clearance[4,16,76,92,93,95].

Our results demonstrate that fibronectin is consistently enriched at AQP4-positive astrocytic endfeet, indicating FN1 deposition at key perivascular regions (Fig. 3i,k), which is likely to contribute to BBB dysfunction. We also observed a genotype-specific shift in APOE–AQP4 colocalization, as *APOE* ε3/ε3 brains show strong positive or negative correlations, whereas *APOE* ε4/ε4 brains exhibit predominantly positive correlations (Fig. 3l), suggesting increased APOE4 accumulation at astrocytic endfeet concomitant with fibronectin accumulation. This convergence of FN1 and APOE4 at gliovascular sites may amplify astrocyte–endothelial dysfunction in *APOE* ε4 carriers. The association of altered plasma (Supplementary Tables 2–4), CSF (Fig. 5n) and brain (Fig. 4l,m) fibronectin levels with CVP and related markers further strengthens the important link between fibronectin and vascular and brain pathology. It also suggests predictive surrogate readouts for potential therapeutic interventions aiming to reduce fibronectin deposition at the gliovascular niche. Consistent with our findings, a recent proteomic study of the monogenic small vessel disease CADASIL reported strong upregulation of FN1 in plasma, with higher FN1 levels associated with greater brain atrophy, accelerated functional decline and lower global cognitive scores[96], reinforcing the connection between vascular integrity, brain health and fibronectin dysregulation.

Although single-cell transcriptomic studies have reported higher FN1 expression in pericytes and endothelial cells than in

astrocytes[1,2,24,28,38,53,70], these measurements reflect mRNA abundance rather than extracellular protein deposition, which can diverge substantially due to post-transcriptional regulation and ECM assembly[97]. Astrocytes are among the most abundant CNS cell types, comprising ~40% of brain cells, and nearly all astrocytes contact the vasculature[98,99]. In contrast, endothelial cells and pericytes together account for only 2–4% of CNS cells[24,44,53,54,100]. Although we found that FN1 is produced by multiple cell types (Fig. 2g,h), consistent with previous studies[2,24,53,54,70,88], the combination of astrocyte abundance at the gliovascular niche and marked *APOE* ε4-associated upregulation of FN1 suggests that astrocytes are the predominant contributors to pathological fibronectin deposition in AD. Our spatial immunohistochemical analyses (Fig. 2h) support this conclusion. We identify fibronectin as a central pathological mediator of *APOE* ε4-associated BBB dysfunction, highlighting the potential therapeutic value of preserving gliovascular integrity. Although *APOE* ε4 has been widely reported to reduce overall APOE secretion and steady-state protein levels in the brain and CSF[101], the increased APOE intensity observed in *APOE* ε4/ε4 astrocytes likely reflects intracellular and perivascular accumulation rather than increased synthesis. This interpretation is consistent with impaired *APOE* ε4 lipidation and BBB trafficking, resulting in aggregation and retention within astrocytic endfeet and perivascular regions[12,19,20,31,74,102], and further supports a broader role for FN1 in vascular pathology. The protective FN1 loss-of-function variant[12], which limits fibronectin deposition and protects *APOE* ε4 carriers from BBB dysfunction, also reduces the risk of Lewy body disease[103], supporting a broader role for fibronectin-mediated vascular pathology across neurodegenerative disorders.

Despite the robust findings in this study, we note some limitations. To further enhance the applicability of these findings to human AD, validation can be conducted in additional human brains and in reductionist models of the human vascular niche. Furthermore, the known overlap of other comorbidities, such as diabetes and hypertension, could contribute to the observed relationships among fibronectin, VEGFA, HB-EGF, IGF-1 and AD pathology. Although we identified inflammation as one driver of fibronectin deposition, the specific inflammatory signals and their roles at different stages of the disease require further investigation. While this study establishes fibronectin as a mechanistic mediator of BBB dysfunction, the consequences of this pathway for cognition and higher-order brain function were not directly assessed and remain an important area for future investigation.

Methods

Ethics

Human samples were sourced from the New York Brain Bank at Columbia University Vagelos College of Physicians and Surgeons and anonymized to ensure that researchers had no access to the donors' personal information. All postmortem tissue was banked with consent from next of kin and distributed stripped of identifiers under institutional review board protocol AAAB0192 as 'not human subject research'. All mice used in this study were treated in accordance with the National Institutes of Health Guide for the Care and Use of Laboratory Animals and approved by the Columbia University Medical Center Institutional Animal Care and Use Committee (IACUC) (approval nos. AABF3553 and AABR4602). Animals were maintained in a temperature- and humidity-controlled facility at Columbia University Medical Center on a 12-h light and 12-h dark cycle, with ad libitum access to food and water in compliance with protocols approved by the IACUC at Columbia University. For zebrafish, all animal experiments were performed in accordance with applicable regulations and were approved by the IACUC at Columbia University (approval no. AABN3554). Animals from the same fish clutch were randomly assigned to each experimental group. Animals were handled with caution to reduce suffering and minimize the total number used.

Brain preparation and immunohistochemistry

Twenty-three postmortem sections of Brodmann area 9 in the prefrontal cortex were acquired from the New York Brain Bank at Columbia University and provided as paraffin-embedded specimens along with neuropathological evaluations. We selected the dorsolateral prefrontal cortex (Brodmann area 9) for analysis due to its well-established involvement in early vascular and neurodegenerative changes in AD, its availability with comprehensive neuropathological assessments in our cohort, and its widespread use in large-scale transcriptomic studies, facilitating integration with existing datasets such as ROSMAP[38,54,80,104]. Immunohistochemistry was performed following previously described procedures[14,105]. For immunohistochemistry, primary antibodies used included FN1 (Proteintech, cat. no. 66042-1-Ig, dilution 1:250), CD31 (Abcam, cat. no. ab134168, dilution 1:250), FN1-EDA (Antibodies-online, cat. no. ABIN108413, dilution 1:200), FN1-EDB (Cell Signaling, cat. no. 36349, dilution 1:200), AQP4 (Abcam, cat. no. ab284135, dilution 1:200), FN1 (Sigma, cat. no. F3648, dilution 1:200), IBA1 (Wako, cat. no. 11-27991, dilution 1:100), APOE (Millipore Sigma, cat. no. 178479, dilution 1:200, and Bioss, cat. no. bs-5039R, dilution 1:200), CDH5 (Thermo Fisher Scientific, cat. no. PA5-143232, dilution 1:100), GFAP (Abcam, cat. no. ab4674, dilution 1:200), GFAP (Thermo Fisher Scientific, cat. no. OPA1-06100, dilution 1:250), VEGF (R&D Systems, cat. no. MAB2932-100, dilution 1:200), IGF-1 (Abcam, cat. no. ab106836, dilution 1:200), HB-EGF (Thermo Fisher Scientific, cat. no. PA5-119187, dilution 1:200) and Aβ42 (Cell Signaling, cat. no. 8243S, dilution 1:200). Secondary antibodies used were goat anti-mouse Alexa Fluor 488 (Thermo Fisher Scientific, cat. no. A11001, dilution 1:500), goat anti-mouse IgG1 Alexa Fluor 555 (Thermo Fisher Scientific, cat. no. A21127, dilution 1:500), goat anti-rabbit Alexa Fluor 555 (Thermo Fisher Scientific, cat. no. A32732, dilution 1:500), goat anti-rabbit Alexa Fluor 647 (Thermo Fisher Scientific, cat. no. A32733, dilution 1:500), goat anti-chicken Alexa Fluor 488 (Thermo Fisher Scientific, cat. no. A11039, dilution 1:500), donkey anti-mouse Alexa Fluor 488 (Thermo Fisher Scientific, cat. no. A32766, dilution 1:500), donkey anti-goat Alexa Fluor 555 (Thermo Fisher Scientific, cat. no. A32816, dilution 1:500) and donkey anti-rabbit Alexa Fluor 647 (Thermo Fisher Scientific, cat. no. A32795, dilution 1:500).

Human APOE replacement mouse models[106,107] and APP knock-in mice (APP(NL-G-F), harboring the Swedish, Arctic and Iberian mutations)[21] were used for this study. Nontransgenic C57BL/6J mice served as controls for $App^{NL\text{-}G\text{-}F}$ mice. $App^{NL\text{-}G\text{-}F}$ and control mice were given a ketamine/xylazine cocktail for deep anesthesia and then transcardially perfused with ice-cold 100 mM PBS (pH 7.4), followed by 10% formalin (Fisher Scientific). Isolated brains were incubated in 10% formalin overnight and then immersed in 30% sucrose at 4 °C until they sank. Brain hemispheres were cryopreserved in OCT mounting medium, sectioned into 40-µm sagittal brain slices using a Leica CM3050 S cryostat and kept in cryoprotectant at −20 °C until immunofluorescence was performed. APOE replacement mice were cervically dislocated, and their brains were subsequently drop-fixed for 48 h in 10% formalin at 4 °C. Brains were then transferred to 30% sucrose at 4 °C and cryo-embedded for sectioning. Coronal sections of 40 µm thickness were acquired and immunostained. Brain sections comprising cortico-hippocampal regions from both sets of experiments were selected and subjected to free-floating immunostaining. Brain sections were initially rinsed in PBS and permeabilized with 0.3% Triton X-100, followed by blocking with 10% normal goat or donkey serum in PBS-T (PBS with Tween-20) for 60 min at room temperature. Primary antibodies were applied overnight at 4 °C in 2% serum in PBS-T. The following primary antibodies were used in various combinations: FN1 (Proteintech, cat. no. 66042-1-Ig, dilution 1:300), CD31 (Abcam, cat. no. ab13468, dilution 1:300), VEGF (R&D Systems, cat. no. MAB2932-100, dilution 1:300), IGF-1 (Abcam, cat. no. ab106836, dilution 1:300), HB-EGF (Thermo Fisher Scientific, cat. no. PA5-119187, dilution 1:300), Fibrinogen (Abcam, cat. no. ab34269, dilution 1:300), AQP4 (Abcam, cat. no. ab284135, dilution 1:200), AQP4 (Proteintech, cat. no. CL594-16473, dilution 1:200), FN1

(Sigma, cat. no. F3648, dilution 1:200), CDH5 (Thermo Fisher Scientific, cat. no. PA5-143232, dilution 1:100), GFAP (Abcam, cat. no. ab4674, dilution 1:200) and GFAP (Thermo Fisher Scientific, cat. no. OPA1-06100, dilution 1:250). The next day, after washing with PBS-T, the sections were incubated with the appropriate secondary antibodies diluted in 2% serum in PBS-T. Secondary antibodies used were goat anti-mouse Alexa Fluor 488 (Thermo Fisher Scientific, cat. no. A11001, dilution 1:500), goat anti-mouse IgG1 Alexa Fluor 555 (Thermo Fisher Scientific, cat. no. A21127, dilution 1:500), goat anti-rabbit Alexa Fluor 555 (Thermo Fisher Scientific, cat. no. A32732, dilution 1:500), goat anti-rabbit Alexa Fluor 647 (Thermo Fisher Scientific, cat. no. A32733, dilution 1:500), goat anti-chicken Alexa Fluor 488 (Thermo Fisher Scientific, cat. no. A11039, dilution 1:500), donkey anti-mouse Alexa Fluor 488 (Thermo Fisher Scientific, cat. no. A32766, dilution 1:500), donkey anti-goat Alexa Fluor 555 (Thermo Fisher Scientific, cat. no. A32816, dilution 1:500) and donkey anti-rabbit Alexa Fluor 647 (Thermo Fisher Scientific, cat. no. A32795, dilution 1:500). DAPI or Hoechst 33342 dye (5 μg ml^{-1}) (Thermo Scientific) was used for nuclear staining for 3 min at room temperature. Following PBS-T washes, sections were mounted on Superfrost Plus slides and coverslipped using SlowFade Gold antifade reagent (Invitrogen, Thermo Fisher Scientific). The slides were kept in the dark at 4 °C until imaging. All mouse models used were 18–22 months old, with at least three animals of both sexes included in every experimental group.

Cerebroventricular microinjection, VEGFR blockage, tissue preparation and immunostaining in zebrafish

Wild-type AB, *fn1b* knockout, transgenic *Tg(nfkb:GFP)*, *Tg(her4.1:GFP)* and *Tg(fn1b:mCherry)* zebrafish lines aged 6–12 months were used for zebrafish experiments and cerebroventricular microinjection[46]. Transgenic *Tg(kdrl:GFP)*[108] zebrafish of both sexes, aged 6 months, were used for the VEGFRi study. All fish were sourced from the same clutch and randomly assigned to different experimental groups. The fish were exposed to fish water supplemented with semaxanib (SU5416) at 10 μM (Selleck Chemicals, cat. no. S2845), tivozanib (AV-951) at 10 μM (Selleck Chemicals, cat. no. S1207) and ZM 306416 at 10 μM (Selleck Chemicals, cat. no. S2897). Doses were adjusted according to the validated dosages[40]. This treatment was applied for 3 h daily over a span of 3 consecutive days. Following the treatment, the fish were killed, and tissue samples were collected[109–111]. Other injections included PBS (control), human Aβ42 (20 μM), human HB-EGF (10 μg ml^{-1}, Gibco, Thermo Fisher Scientific, cat. no. 100-47-50UG), human IGF-1 (10 μg ml^{-1}, Gibco, Thermo Fisher Scientific, cat. no. PHG0071), Torin2 (10 μM, Cayman Chemical Company, cat. no. 14185), camptothecin (1 μM, Millipore Sigma, cat. no. 390238), human TNF recombinant protein (100 ng ml^{-1}, Cell Signaling, cat. no. 16769S), PF-573228 (100 μM, FAK inhibitor, CAS no. 869288-64-2, Selleck Chemicals, cat. no. S2013) and ATN-161 (10 μM, Selleck Chemicals, cat. no. S8454). The total injection volume was 1 μl. Animals were euthanized at relevant time points and subjected either to histological tissue preparation or to brain dissection and dissociation for single-cell sequencing preparation[43,109,112].

For histological tissue preparation, zebrafish heads were dissected and fixed overnight at 4 °C in 4% paraformaldehyde (PFA). Samples were washed several times with 0.1 M phosphate buffer and incubated overnight in a solution containing 20% sucrose and 20% EDTA at 4 °C for cryoprotection and decalcification. The next day, samples were embedded in the cryoprotectant sectioning resin OCT (Thermo Fisher Scientific, cat. no. 23-730-571) and cryosectioned into 12-μm-thick sections on SuperFrost Plus glass slides. For immunohistochemistry, the sections were dried at room temperature, followed by washing steps in PBS with 0.3% Triton X-100 (PBSTx). Primary antibodies were applied overnight at 4 °C. The next day, the slides were washed three times with 0.3% PBSTx, and then the appropriate secondary antibodies, together with DAPI, were applied for 2 h at room temperature. The slides were then washed several times before mounting with coverslips using 70% glycerol in PBS. The following primary antibodies were used in various combinations: FN1 (Proteintech, cat. no. 66042-1-Ig, dilution 1:300), GS (Abcam, cat. no. ab176562, dilution 1:500), BLBP (Abcam, cat. no. ab279649, dilution 1:500), ZO-1 (Thermo Fisher Scientific, cat. no. 33-9100, dilution 1:500), GFP (Thermo Fisher Scientific, cat. no. PA1-9533, dilution 1:2,000), VEGF (R&D Systems, cat. no. MAB2932-100, dilution 1:500), IGF-1 (Abcam, cat. no. ab106836, dilution 1:300) and HB-EGF (Thermo Fisher Scientific, cat. no. PA5-119187, dilution 1:300). Secondary antibodies used were as follows: goat anti-mouse Alexa Fluor 488 (Thermo Fisher Scientific, cat. no. A11001, dilution 1:500), goat anti-chicken Alexa Fluor 488 (Thermo Fisher Scientific, cat. no. A11039, dilution 1:500), goat anti-rabbit Alexa Fluor 555 (Thermo Fisher Scientific, cat. no. A32732, dilution 1:500), goat anti-mouse Alexa Fluor 555 (Thermo Fisher Scientific, cat. no. A21127, dilution 1:500), goat anti-rabbit Alexa Fluor 647 (Thermo Fisher Scientific, cat. no. A32733, dilution 1:500), donkey anti-mouse Alexa Fluor 488 (Thermo Fisher Scientific, cat. no. A32766, dilution 1:500), donkey anti-goat Alexa Fluor 555 (Thermo Fisher Scientific, cat. no. A32816, dilution 1:500) and donkey anti-rabbit Alexa Fluor 647 (Thermo Fisher Scientific, cat. no. A32795, dilution 1:500). For antigen retrieval of ZO-1 and FN1, slides were heated in 10 mM sodium citrate (pH 6.0) at 85 °C for 15 min before the primary antibody incubation step. Imaging was performed using a Zeiss AxioImager Z1 and a Zeiss LSM 800 confocal microscope. For data analysis, colocalization of immunohistochemical markers was quantified using the Colocalization module in ZEN software (Carl Zeiss). Statistical analysis was conducted using GraphPad Prism (version 6.02, GraphPad Software). Differences between experimental groups were assessed using unpaired parametric *t* tests with Welch's correction. Effect sizes were calculated using G*Power (https://www.psychologie.hhu.de/arbeitsgruppen/allgemeine-psychologie-und-arbeitspsychologie/gpower), and sample sizes were estimated with nQuery and scPower[113]. Each experimental group included at least three animals of both sexes.

3D hydrogel preparation, cytokine treatment, RNA isolation and sequencing

Primary human fetal astrocyte (ScienCell Research Laboratories, cat. no. 1800) starPEG–heparin hydrogel (3D pHA) cultures were prepared as previously described[34,37]. Briefly, the pHAs at passage 2 were thawed and counted using an automated cell counter (Countess II FL, Thermo Fisher Scientific). Cells (0.375×10^6) were plated into T75 flasks in 10 ml of complete astrocyte medium (Astrocyte Medium, ScienCell Research Laboratories, cat. no. 1801, supplemented with 2% FBS, 1× Astrocyte Growth Supplement and 1× penicillin–streptomycin). The cells were dissociated and collected from the culture flasks using StemPro Accutase Cell Dissociation Reagent (Gibco, cat. no. A1110501) 3 days after thawing. After centrifugation at 271*g* (Thermo Fisher Scientific Heraeus Megafuge 16R, rotor 75003629 with a 168 mm maximum radius) for 8 min, the supernatant was carefully aspirated, and pHAs were resuspended in DPBS or complete astrocyte medium and counted. The cell concentration was adjusted to 25,000 cells per hydrogel. Afterward, the cells were first gently mixed with a heparin–maleimide conjugate (C. Werner, TU Dresden, cat. no. HM6 170530) solution and then with a starPEG–MMP–peptide conjugate (C. Werner, TU Dresden, cat. no. PM-CIWC-Ac 171107) solution in a 1:1:2 volume ratio to obtain the desired hydrogel volume with final concentrations of 1.5 mM heparin–maleimide conjugate and 1.12 mM starPEG–MMP–peptide conjugate in a 20 μl total volume. Next, a 20 μl droplet was quickly placed on a Parafilm sheet and left to gelate for about 2 min. Finally, the hydrogels were gently transferred into 24-well non-tissue culture-treated plates (Falcon, cat. no. 351147) containing 0.75 ml of complete astrocyte medium per well and cultured in a humidified cell culture incubator at 37 °C. The medium was changed 1 day after cell encapsulation and three times a week thereafter. The 3D pHA cultures were maintained for up to 3 weeks depending on the experimental setup. Human astrocytes encapsulated in hydrogels were treated with TNF (Peprotech, cat. no.

300-01A, 0.1 µg ml^{-1}, 5.7471 nM) and IL-4 (Peprotech, cat. no. 200-04, 0.1 µg ml^{-1}, 6.6225 nM), or a combination of both, 1 day following cell encapsulation. These treatments were prepared by diluting stock solutions in complete astrocyte medium and were applied continuously by replenishing the treatment medium along with the medium of control cells three times a week until the end of the 3-week culture period. We used the Norgen Total RNA Extraction Kit for isolation. In brief, three gels per condition were lysed in lysis buffer, followed by centrifugation and washing according to the manufacturer's protocol. The RNA concentration was measured using a NanoDrop 2000 spectrophotometer (Thermo Fisher Scientific), and the quality of the RNA was assessed using an Agilent 2100 Bioanalyzer (Agilent Technologies). Samples with an RNA integrity number >9 were deemed suitable for further analysis (Extended Data Fig. 10).

Library preparation, sequencing, alignment to the human genome and bioinformatic analyses were performed[37,46]. In brief, complementary DNA (cDNA) libraries were prepared following the protocol for the NEBNext Ultra Directional RNA Library Prep Kit. This involves the following steps: mRNA isolation through poly(A)+ selection and fragmentation; first-strand and second-strand cDNA synthesis; purification using the Agencourt AMPure kit; and end repair/dA-tailing of cDNA. Adaptors were ligated to the dA-tailed cDNA, followed by size selection using AMPure XP beads. Indexing of the library constructs was performed with Illumina index primers during the subsequent PCR amplification using NEBNext Q5 2× PCR Master Mix. Lastly, the libraries were purified using the Agencourt AMPure kit. Libraries were pooled and sequenced on an Illumina NextSeq 500 system, resulting in approximately 27–38 million 75-bp single-end reads. All protocols were performed according to the manufacturers' instructions. Raw sequence data were processed using a standard Illumina pipeline. Quality-controlled reads were aligned to the human genome (GRCh38) using GSNAP, and differential expression analysis was conducted with DESeq2. A minimum of three biological replicates per condition were used, with power analysis ensuring an adequate sample size to detect at least a twofold change in gene expression at a 5% error rate.

Cell sorting and single-cell transcriptomics in zebrafish

The telencephalon of 6- to 16-month-old fish was dissected in ice-cold PBS and directly dissociated using the Neural Tissue Dissociation Kit (Miltenyi Biotec, cat. no. 130-092-628)[45,109]. After dissociation, cells were filtered through a 40-µm cell strainer into 10 ml of 2% BSA in PBS, centrifuged at 300*g* for 10 min and resuspended in 4% BSA in PBS. The viability indicator dyes SYTOX Blue (Invitrogen, cat. no. S34857) and Vybrant DyeCycle Ruby (Invitrogen, cat. no. V10309) were used to sort the cells by flow cytometry (FACS). Samples from different experimental groups were simultaneously sorted on separate FACS machines (Sony MA900-FP) to minimize the time they remained on ice. Sorting histograms are provided in Extended Data Fig. 10. The resulting single-cell suspension was promptly loaded onto the 10x Chromium system[114]. The 10x libraries were prepared according to the manufacturer's instructions. The generated libraries were sequenced using the Illumina NovaSeq 6000 platform[43,45,109,115]. In total, 66,848 cells were sequenced for the *fn1b*$^{-/-}$ study. The raw sequencing data were processed using the Cell Ranger Single Cell Software Suite (version 6.1.2, 10x Genomics) with the default options. On average, 95.45% of the total 399.6 million gene reads were aligned to the zebrafish genome assembly GRCz11 (Ensembl release 105). For single-cell sequencing of VEGFR inhibitor treatment, we treated double-transgenic zebrafish (*Tg(fli1a:EGFP)*, *Tg(her4.1:RFP)*)[61,62] ($n = 3$ per group) with a VEGFR inhibitor cocktail (ZM 306416, semaxanib and tivozanib) or DMSO as the control. Doses were adjusted according to the established and validated protocol[40]. Three days after treatment, we dissected the telencephalons and dissociated the tissue using the same methodology described above. Filtered and dissociated cells were resuspended in 4% BSA in PBS. GFP$^+$ and RFP$^+$ cells were then sorted into separate tubes using a Sony MA900-FP sorter and promptly loaded onto the 10x Chromium system. The 10x libraries were prepared, and cDNA libraries were sequenced using the Cell Ranger Single Cell Software Suite (version 6.1.2, 10x Genomics). In total, 24,518 cells were sequenced and analyzed. On average, 95.6% of the 357.4 million gene reads per cohort mapped to the zebrafish genome assembly GRCz11 (Ensembl release 105). The resulting matrices were used as input for downstream data analysis with Seurat[116].

Read alignment and quality control

To create Seurat objects for *fn1b*$^{-/-}$ study, we filtered out cells with fewer than 200 expressed genes and genes expressed in fewer than three cells. After filtering out the low-quality cells, the Seurat objects were normalized, and the top 2,000 variable genes were used for further analysis. Anchors were identified using the FindIntegrationAnchors function, and the datasets were integrated using the IntegrateData function. Layers were integrated (IntegrateLayers) and joined (JoinLayers). In addition, DoubletFinder[117] was used to identify and remove doublets, and the remaining analyses were performed on singlets. The integrated Seurat object included 62,302 cells and 25,030 genes. The data were scaled using all genes, and 32 principal components were identified (RunPCA). Cell clustering, marker gene analyses, differential gene expression and preparation of feature plots were performed using Seurat (version 5) functions as described in previous studies[45,79,116]. To identify DEGs, we used the FindMarkers function of Seurat with a logfc.threshold of 0.25. To create Seurat (version 4.1.3) objects for the VEGFRi study, a similar analytical pipeline was used. The clusters were identified using a resolution of 1. In total, 37 clusters were found. The main cell types were identified using *s100b* and *gfap* for astrocytes; *kdrl* and *lef1* for endothelial cells; *hbaa1* and *ba1* for erythroid cells; *nell2b* and *slc17a6a* for excitatory neurons; *tubb5* and *marcksb* for immature neurons; *il2rb* and *rgs13* for immune cells; *gad1* and *gad2* for inhibitory neurons; *sv2a*, *nrgna* and *grin1a* for neurons; *cd74a* and *apoc1* for microglia; *pcna* and *mcm5* for neuroblasts; *pdgfrb* and *kcne4* for pericytes; *mbpa* and *mpz* for oligodendrocytes; *aplnra* for oligodendrocyte precursor cells; and *myh11a* and *tagln2* for vascular smooth muscle cells[45,79,112].

Isogenic iPS cell-derived astrocytes

KOLF2.1J isogenic iPS cell lines, expressing the *APOE* ε3/ε3 and *APOE* ε4/ε4 variants, were cultured according to a previously described protocol[26]. The iPS cells were maintained under feeder-free conditions on hydrogel-coated plates using mTeSR1 medium (STEMCELL Technologies). Medium changes were performed daily, and cells were passaged at approximately 80% confluency to maintain optimal growth conditions. Differentiation of iPS cells into astrocytes was performed following a previously described protocol[32]. Differentiation efficiency was confirmed by immunostaining for astrocytic markers such as GFAP, ensuring the generation of a homogeneous astrocyte population. For immunocytochemistry, astrocytes were fixed with 4% PFA, permeabilized with 0.1% Triton X-100 and blocked with 5% normal serum to minimize nonspecific binding. Cells were then incubated with the following primary antibodies: APOE (rabbit polyclonal antibody, Bioss, cat no. bs-5039R, 1:500), FN1 (mouse monoclonal antibody, Proteintech, cat. no. 66042-1-Ig, 1:500), VEGFA (mouse monoclonal antibody, R&D Systems, cat. no. MAB2932, 1:500), GFAP (rabbit polyclonal antibody, Thermo Fisher Scientific, cat. no. OPA1-06100, 1:500) and IGF-1 (rabbit polyclonal antibody, Abcam, cat. no. ab9572, 1:500). Secondary antibodies conjugated to Alexa Fluor dyes (488, 555 or 647) were used at a dilution of 1:1,000, and DAPI was included for nuclear staining. iPS cell-derived isogenic astrocytes were treated with human HB-EGF recombinant protein (Thermo Fisher Scientific, cat. no. 100-47) at final concentrations of 1 and 10 ng ml^{-1}. Treatments were performed over 24 h, after which the cells were fixed and processed for immunostaining. Immunofluorescence images were acquired using

a Zeiss Axio Observer microscope equipped with a confocal module. Image quantification was conducted using Zeiss ZEN software, supplemented by Arivis analytical pipelines to assess marker intensity and colocalization. For quantification, images containing FN1, APOE and DAPI signals were analyzed to assess fibronectin distribution in relation to the cell nucleus, cell body and its close periphery. Masks were generated based on DAPI$^+$ nuclei, with boundaries extended by 10 µm from the nuclear edge to encompass the cell body and its immediate periphery, also capturing the extracellular fibronectin localized near the cells. FN1 intensity within these defined regions was measured, and the results were normalized to the area of the analyzed region to ensure consistency and comparability across samples. Data were then subjected to statistical analysis using GraphPad Prism. Pairwise comparisons were analyzed using *t* tests with Welch's correction, while multiple comparisons were evaluated using two-way analysis of variance (ANOVA) with Tukey's post-hoc test. All results are expressed as mean ± s.e.m., and a significance threshold of $P < 0.05$ was applied to determine statistical significance.

Vascular cells, iPS cell culture and cell lines

This study used APOE isogenic lines derived from four different donors, generated from previously published iPS cell lines[118]. All lines tested negative for mycoplasma and were karyotypically normal, as confirmed by G-banded karyotype analysis (WiCell Research Institute). The iPS cells were maintained in six-well plates coated with growth factor-reduced Matrigel or Cultrex at 37 °C and 5% CO_2. The cultures were fed twice a week with mTeSR1 medium containing an FGF2 DISC (StemCultures, DSC500-48). Each week, one FGF2 DISC was added to a well of a six-well plate containing 2 ml of mTeSR1 medium. The medium, but not the FGF2 DISC, was replaced every 2–3 days based on culture confluency. Human pluripotent stem (hPS) cell cultures were clump-passaged using ReLeSR about once a week, and a new FGF2 DISC was added. Cells were not allowed to grow past 80% confluency. iPS and vascular cell samples were genotyped periodically to confirm *APOE* ε3/ε3 versus *APOE* ε4/ε4 line status using TaqMan SNP assays (rs429358, Life Technologies, Assay ID: C_3084793_20; rs7412, Life Technologies, Assay ID: C_904973_10). Assays were performed using a QuantStudio 6 Flex system.

Codifferentiation of iPS cells into vascular cells

When hPS cells reached approximately 80% confluency, they were passaged using Accutase and seeded at a density of 50,000 cells per cm^2 on Cultrex-coated tissue culture plates. hPS cells were cultured overnight in mTeSR1 medium supplemented with 10 µM Y-27632. To start the differentiation, we followed our previously published protocol[27]. In brief, hPS cell medium was replaced with LaSR medium composed of Advanced DMEM/F12, GlutaMAX and 60 µg ml^{-1} of L-ascorbic acid; supplemented with 6 µM CHIR99021; and cultured for 2 days to pattern cells toward mesoderm. On day 2, the medium was fully replaced with LaSR medium supplemented with 100 ng ml^{-1} $VEGF_{165}$ and 20 ng ml^{-1} FGF2.

FN1–APOE co-immunoprecipitation

APOE ε3/ε3 and *APOE* ε4/ε4 iPS cell-derived astrocytes were cultured for 14 days. Conditioned medium and cell lysates were collected in IP lysis buffer (Thermo Fisher Scientific, cat. no. 97787) supplemented with protease and phosphatase inhibitor cocktails. Both lysates and conditioned medium were centrifuged at 36,800*g* for 10 min at 4 °C, and the supernatants were collected. Soluble protein concentrations were determined using the BCA assay. Co-immunoprecipitation was performed using a mouse monoclonal FN1 antibody (Proteintech, cat. no. 66042-1-Ig) bound to 15 µl of Protein G-agarose beads. Samples were incubated overnight at 4 °C with gentle shaking. The following day, the beads were washed three times with IP lysis buffer, and the bound protein complexes were eluted by boiling the beads in LDS buffer at 95 °C for 5 min. Proteins were separated on 4–12% Bis–Tris NuPAGE gels and transferred to membranes, which were probed with a goat polyclonal APOE antibody (1:1,000, Sigma, cat. no. 178479) and developed using a Bio-Rad ChemiDoc imager.

FN1 measurement in human CSF and plasma

For CSF, we obtained FN1 values and associated clinical data from the Emory CSF Somalogic 7k dataset, available at https://synapse.org/Emory300ATX (project SynID: syn52888250) and through the AMP-AD Knowledge Portal. Before statistical analysis, data were $\log_2$-transformed to improve normality, as confirmed by Shapiro–Wilk tests. Because the transformed AD and control groups did not violate normality or variance assumptions, we applied a two-sample Student's *t* test to compare FN1 levels between groups. Fold change was calculated by exponentiating the difference in group means ($\log_2$ scale). Plasma levels of FN1 and VEGFA were measured using commercially available ELISA kits (VEGFA: Abcam, ab222510; FN1: Abcam, ab108847) according to the manufacturer's protocol. Briefly, plasma samples were thawed on ice, diluted (1:2 for VEGFA and 1:4,000,000 for FN1) and incubated in antibody-coated wells. Bound protein was detected using fluorescently conjugated secondary antibodies. Absorbance was measured at 450 nm using a BioTek ELx800 plate reader, and concentrations were calculated using standard curves generated from protein standards. All measurements were performed in duplicate and normalized to intra-well references. Other AD-related plasma biomarker data were obtained from previously published studies[119].

Cell sorting and iPS cell-derived endothelial cell monolayer culture

Vascular differentiated cells (described above) were sorted on days 5–8 of differentiation using CD31 magnetic beads (Miltenyi, 130-091-935). Sorted hPS cell-derived endothelial cells were plated at densities of approximately 3.0–5.5 × 10^5 cells per cm^2 on culture plates coated with EmbryoMax (0.1% gelatin, Sigma, ES006B) and containing LaSR medium supplemented with 10% FBS, 25 ng ml^{-1} VEGF, 20 ng ml^{-1} FGF2 and 10 µM Y-27632. The medium was replaced the following day to remove Y-27632. Endothelial cells were cryopreserved in CS10 freezing medium when the cultures reached approximately 80% confluency. For some experiments, three *APOE* ε3/ε3 lines and three *APOE* ε4/ε4 lines were thawed, cultured on EmbryoMax-coated plates for an additional 3 days, and then collected for RNA analysis. In other experiments, iPS cell-derived endothelial cells were not frozen but were instead cultured for an additional 2–4 days after sorting with PromoCell MV2 medium (C-22022) before RNA isolation. In either experimental setup, *APOE* ε3/ε3 and *APOE* ε4/ε4 lines were differentiated, sorted and grown in parallel for comparison.

3D iPS cell vascular models in fibrin hydrogels (VAMP models)

To encapsulate unsorted vascular cells into the hydrogel, we followed methods we previously established[27]. In brief, vascular cells were collected as single cells between days 5 and 8 of differentiation. Cells were counted, spun down and resuspended at 2 × 10^7 cells per ml. Next, 25 µl of cell suspension in LaSR medium with thrombin (4 units per ml PBS^{++} (PBS supplemented with Ca^{2+} and Mg^{2+})) and 25 µl of fibrinogen solution (20 mg ml^{-1} in PBS^{++}) were thoroughly mixed and immediately pipetted into a cell culture-treated plate. The resulting fibrin gel comprised 10 mg ml^{-1} fibrinogen, 2 units per ml of thrombin and 1 × 10^7 cells per ml. After fibrin polymerization, LaSR medium supplemented with 5 µl ml^{-1} aprotinin (10,000 kallikrein inhibitor units per ml stock solution) and 50 ng ml^{-1} VEGF was added to induce vessel growth. A 50% medium exchange was performed every 3–4 days. VAMPs were collected for analysis after 7 days of culture.

2D endothelial cell monolayers and immunofluorescence

Cells were fixed with cold 4% PFA for 15 min and washed three times with PBS. Cells were permeabilized for 7 min with 0.1% saponin (Sigma,

S7900) in PBS, washed with PBS and blocked in 2% fish gelatin for 45 min. The antibody buffer consisted of 0.01% saponin in 0.5% fish gelatin in PBS. Primary antibodies were applied sequentially with washes between steps. CD31 (BD Biosciences, cat. no. 550389, 1:200) and ZO-1 (Proteintech, cat. no. 21773-1-AP, lot no. 00106957, 1:200) were incubated for either 12 h at 4 °C or 2 h at room temperature on a rocker. Washes between antibody steps were performed at room temperature on a rocker using PBS for 5 min (twice), followed by one wash with antibody buffer. Secondary antibodies (1:250; Alexa Fluor 568 anti-mouse, Thermo Fisher Scientific, A11019; Alexa Fluor 647 anti-rabbit, Jackson ImmunoResearch, 705-606-147) were applied sequentially for 45 min at room temperature on a rocker, followed by DAPI staining for 15 min. Fluorescence imaging was performed on an Echo Revolution microscope with a 20× objective (NA 0.45), equipped with DAPI, FITC, Texas Red and Cy5 emission/excitation filters. Images were converted to the OME-TIFF format, and those shown were cropped at higher magnification for visualization.

Whole-mount immunofluorescence of 3D VAMP models

Cells were fixed with cold 4% PFA for 1 h on a rocker at 4 °C and washed three times with PBS. Staining was performed without permeabilization or blocking steps. Primary antibodies were diluted in PBS, with anti-CD31 at 1:200 (BD Biosciences, cat. no. 550389, lot no. 4137906) and anti-fibronectin at 1:250 (Invitrogen, cat. no. PA5-29578, lot no. 79657018). All washes were performed with PBS in triplicate for 60 min at 4 °C on a rocker. The primary antibodies were incubated sequentially overnight on a rocker at 4 °C, with washes following each incubation. Secondary antibodies were incubated overnight at a 1:250 dilution in PBS, using Alexa Fluor 647-conjugated donkey anti-rabbit IgG (Jackson ImmunoResearch, cat. no. 711-605-152, lot no. 165592) and Alexa Fluor 488-conjugated donkey anti-mouse IgG (Jackson ImmunoResearch, cat. no. 715-545-150, lot no. 174724). The VAMPs were stored in PBS for imaging.

Fibronectin and CD31 imaging and analysis in 3D VAMP models

Imaging of the VAMPs was performed on a Zeiss LSM 780 confocal microscope with a Zeiss Plan-Apochromat 40× objective (NA 1.2, water immersion). The 488-nm argon laser and the 633-nm HeNe laser were used at the same power throughout all acquisitions. Optical sections were matched for each channel with an optical section thickness of 1.2 µm and a step size of 0.6 µm. To avoid bias, each z-stack was selected by searching for CD31 staining only. Three VAMPs were imaged per cell line, each with a minimum of three z-stacks.

Analysis was performed using Imaris software (version 10.2.0). Three ROIs were selected per image; the ROIs were restricted to tube-like (vessel) formations. To keep the size of rendered regions comparable, the ROIs were cut from raw files at the same size of 30 µm × 80 µm (*xy*), with a thickness of 4.5 µm (eight *z*-slices). Selection of each ROI was recorded to confirm that no overlap had occurred. The CD31 signal within each ROI was 3D-rendered using the Imaris Surfaces application. There was no image subtraction, deconvolution or other processing before rendering. The surface algorithm included smoothing at 0.6 µm, and each isogenic pair was subjected to the same threshold. A size restriction filter was added to the surface rendering so that each ROI contains only one large tube-like structure, removing small edges of neighboring structures. Imaris surface statistics files were exported as CSV files for each ROI. The statistics were opened in Excel, organized by cell line, and the mean fibronectin intensity within CD31 structures was exported to Prism for graphing and statistical analysis.

Western blots

VAMP sample preparation (treated). VAMP models were pooled based on genotype and lysed in 100 µl of lysate buffer consisting of a 1:1 mixture of Laemmli buffer (without bromophenol blue) and 1× RIPA buffer supplemented with a broad-spectrum protease inhibitor (1:50) (Roche, cat. no. 11836170001) and phosphatase inhibitor (1:10; Roche, cat. no. 04906837001). The samples were mechanically dissociated with a pestle to help dissolve the model and then sonicated for 10 min using a 30-s on/off cycle at 4 °C. In between each round, a P200 pipette was used to mechanically dissociate any remaining chunks. The sonication and mechanical dissociation steps were each repeated three times.

VAMP sample preparation (untreated). Three VAMP models were pooled and lysed in 100 µl of lysate buffer consisting of a 1:1 mixture of Laemmli buffer (without bromophenol blue) and 1× RIPA buffer supplemented with a broad-spectrum protease inhibitor (1:50; Roche, cat. no. 11836170001) and phosphatase inhibitor (1:10; Roche, cat. no. 04906837001). Samples were lysed using a LABGIC tissue grinder to disrupt the 3D model, then sonicated for 10 min using a 30-s on/off cycle at 4 °C. The samples were then centrifuged at 36,800*g* at 4 °C for 10 min. The supernatant was discarded, and the remaining lysate was retained.

Astrocyte lysates. Isogenic iPS cell-derived human astrocytes were cultured in standard medium. Culture medium was removed, and the cells were pelleted after washing with ice-cold PBS. For protein isolation, pelleted cells were treated with a cell lysis buffer containing 8 M urea, 1% SDS in 0.1 M ammonium bicarbonate and protease inhibitors (one mini-Complete EDTA-free tablet). The cell lysates were centrifuged at 36,800*g* for 30 min at 4 °C. The supernatant, containing total proteins, was collected in a new tube. The total protein concentration was then determined using the BCA assay (Pierce).

All samples. Total protein concentrations were determined using the DC Protein Assay (Bio-Rad, 5000111). Lysates and conditioned medium were prepared for gel electrophoresis by diluting each sample with Laemmli SDS sample buffer (Boston BioProducts, BP-111R). A 30-µg sample (VAMP) was loaded onto a 6% Bis–acrylamide gel. The gel was then run on ice for approximately 2 h. Using a wet transfer system, proteins were transferred from the Bis–acrylamide gel to a polyvinylidene fluoride membrane at 20 V and 3 A overnight in an ice bucket at 4 °C. The membranes were dried for 10 min at 37 °C, then rehydrated in 100% methanol for 30 s, followed by Tris-buffered saline (TBS) for 5 min on a rocker at room temperature. Membranes were stained for total protein (LiCor, 926-10016). Next, the membranes were blocked in a 1:1 mixture of TBS and EveryBlot blocking buffer (Bio-Rad, 12010020) for 10 min on a rocker at room temperature. The membrane was incubated with primary antibodies (fibronectin, 1:1,000; Invitrogen, PA5-29578) diluted in blocking buffer (a 1:1 mix of EveryBlot blocking buffer and TBST (TBS with 0.2% Tween-20)) overnight on a rocker at 4 °C. All blots, raw data and experimental parameters are provided as source data.

Chemiluminescent secondary antibody and imaging

The following day, the membranes were washed in TBST on an orbital shaker at 125 rotations per minute (rpm) for 5 min per wash, with a total of four washes. The membranes were incubated with an anti-rabbit IgG HRP antibody (Cell Signaling, 7074S) diluted in blocking buffer (a 1:1 mix of EveryBlot blocking buffer and TBST) for 1 h on a rocker at room temperature. The membranes were then washed in TBST on an orbital shaker at 125 rpm for 5 min per wash, with a total of four washes, followed by a final fifth wash in TBS. Finally, the membranes were rinsed with Milli-Q water and incubated in Clarity Western ECL Substrate (Bio-Rad, 170-5060) for 3 min. The membranes were then imaged using the Odyssey M imaging system, and quantification was performed using the Empiria Studio program, normalizing to total protein.

KEGG pathway analyses of ε4 carrier screen in endothelial snRNA-seq

We obtained snRNA-seq data from a multiregion single-cell transcriptomic atlas of postmortem human brains (1.3 million cells from 48

ROSMAP participants, covering six brain regions and six stages of AD progression; Synapse SynID: syn52293442 and syn3157322). Using Seurat (version 4), we isolated astrocytes and major vascular cell subsets (endothelial cells, pericytes, smooth muscle cells), annotated relevant clinical metadata (for example, Braak stage, *APOE* genotype) and filtered cells by quality control criteria (minimum 200 detected genes, <10% mitochondrial content and <5% ribosomal content). We then applied SCTransform (version 2) to normalize the data and regress out technical covariates, including mitochondrial and ribosomal content. For downstream analyses, we aggregated gene expression at the donor level, retaining genes that met a minimum detection threshold for each cell type. We tested the effects of *APOE* genotype and AD diagnosis on FN1 and VEGFA expression within astrocytes and endothelial cells by fitting a linear mixed-effects model for each gene. Specifically, we retained only donors whose Braak stage classified them as control (0–II) or AD (IV–VI) and limited *APOE* genotype categories to ε3/ε3, ε3/ε4 and ε4/ε4. The model included a fixed effect for *APOE* genotype, a fixed effect for AD diagnosis, and their interaction, with donor ID specified as a random intercept. We used lmerTest for model fitting, emmeans for post-hoc comparisons and a violin/box plot overlay to visualize expression distributions. We then assessed FN1–VEGFA coexpression in astrocytes using a three-way interaction model involving FN1 (gene 1), APOE4 status and disease status (control versus AD) to capture potential genotype-by-disease effects. When necessary, we applied log-like (pseudolog) transformations to stabilize variance, refitted the model and visualized predicted interactions using ggeffects. Then, we performed a donor-level analysis of NF-κB1 expression across Braak-based classifications (control, mild cognitive impairment, AD) in astrocytes using a Kruskal–Wallis test (due to non-normal distributions), followed by Dunn's post-hoc tests (FDR-corrected). We also assessed associations between NF-κB1 (or NF-κB2) and FN1 expression in astrocytes by fitting ordinary least squares regressions controlling for age and sex. Finally, to test whether FN1 expression interacts with *APOE* ε4 carrier status, we fitted a linear model of each gene's donor-level expression on FN1, *APOE* ε4 carrier status, and their interaction. Genes with significant interaction terms ($P < 0.05$, uncorrected) were assessed using KEGG enrichment analysis (clusterProfiler) to identify biological pathways enriched among positively and negatively interacting genes.

RNA isolation, cDNA preparation and qPCR in iPS cell-derived endothelial cells

Total RNA was isolated from cells using the Zymo RNA Clean & Concentrator Kit. RNA concentrations were measured using a Nanodrop instrument, and cDNA was generated with the High-Capacity cDNA Reverse Transcription Kit. qPCR was run with 1.25 ng of cDNA per reaction using TaqMan probes for FN1 (Assay ID: Hs01549976_m1, Life Technologies) with 18S (Assay ID: Hs01026310_m1, Life Technologies) as the loading control. qPCR was performed on a QuantStudio 6 Flex system.

RT–qPCR in zebrafish

HB-EGF was microinjected into the adult telencephalon of the reporter transgenic zebrafish line *Tg(her4:GFP)*[120], a widely used reporter that labels astroglial populations. Because adult zebrafish astroglial populations overlap in molecular markers, we used *her4.1* to label the dominant astroglia. One day after cerebroventricular microinjection, the brains were dissected, and single-cell suspensions were prepared. Following FACS, GFP-positive sorted astrocytes and the remaining GFP-negative sorted cells, mainly neurons, were immersed in TRIzol reagent (Invitrogen, cat. no. 15596026). Sorting histograms are provided in Extended Data Fig. 10. RNA isolation was performed using the Direct-zol RNA Microprep Kit (Zymo Research, cat. no. R2060) according to the manufacturer's instructions. cDNA was synthesized from the purified RNA using the SuperScript III First-Strand Synthesis System (Invitrogen, Thermo Fisher Scientific, cat. no. 18080051) with oligo(dT) primers, following the manufacturer's protocol. The reverse transcription followed by qPCR (RT–qPCR) reaction was performed in a final volume of 10 µl. To reach the final volume, we used 5 µl of PowerUp SYBR Green Master Mix 2× (Applied Biosystems, cat. no. A25742), 1 µM of each primer (*igf1* forward #1: CAGCAAACCGACAGGATATGG, reverse #1: CAGCTCTGAAAGCAGCATTCG from ref. 121; *igf1* forward #2: GGGATGTCTAGCGGTCATTT, reverse #2: CAGTGAGAGGGTGTGGGTA; *vegfa* forward: TTCGAGCGCCTCATCATTAC, *vegfa* reverse: GCTGCTGGTAGACATCATCC; β-actin forward: ATGCAGAAGGAGATCACATCCC, β-actin reverse: GCTTGCTAATCCACATCTGCTG), 1 µl of the cDNA (10 ng final concentration), and UltraPure DNase/RNase-free distilled water (dH_2O) (Invitrogen, cat. no. 10977015). The cycle threshold (C_t) value for the target gene was calculated using the QuantStudio 3 real-time PCR system. Amplification conditions for RT–qPCR were as follows: 50 °C for 2 min, 95 °C for 10 min, followed by 40 cycles of 95 °C for 15 s and 60 °C for 1 min. The melting curve for each sample was analyzed by heating at 95 °C for 15 s, 60 °C for 1 min and 95 °C for 1 s after the amplification reactions.

Human single-nucleus datasets

Preprocessing and quality control steps for snRNA-seq data—including library alignment, background noise removal, demultiplexing, normalization, clustering, removal of low-quality cells and cell type classification—were performed[38,40]. We tested the association between pathological AD and normalized snRNA-seq data using logistic regression, controlling for age and sex. Results were corrected for multiple hypothesis testing by calculating the FDR.

Human brain DNA methylation measurement

The genome-wide DNA methylation profile was measured using the Infinium MethylationEPIC Kit (Illumina) on the New York Brain Bank, National Institute on Aging–AD Family-Based Study (NIA–AD FBS)/National Centralized Repository for AD and Related Dementias (NCRAD) and Estudio Familiar de Influencia Genetica en Alzheimer (EFIGA) cohorts[60]. For sample-level quality control, we checked the control probes, sex mismatch, contamination and genotype outlier calling to identify and remove samples that failed any of these quality control metrics. For CpG probe-level quality control, we kept those CpG sites with a detection *P* value of <0.01 across all qualified samples and masked sample-specific CpG sites with new detection *P* values of >0.01 (ref. 122). We further removed CpG sites reported to have cross-hybridization problems[123] and polymorphic CpG sites[123]. We further corrected the dye bias for all qualified CpG probes. For this study, we used 20 Hispanic samples with both DNA methylation data and genome-wide association study data.

Causal mediation analyses

Causal mediation modeling was performed in ROSMAP RNA-sequencing samples[124] to test whether the expression of the mediator gene mediates the association between the expression of the predictor gene and the trait in dorsolateral prefrontal cortex samples. This analysis was performed using the mediation package in R, and confidence intervals were established through a nonparametric bootstrap method involving 1,000 resamples[125].

Fibronectin overexpression and BBB leakage assay

Zebrafish embryos were injected at the single-cell stage with the *her4.1*:FN1-T2A-GFP plasmid to express human fibronectin (FN1, derived from ref. 126) specifically in astroglia. Later, at 4 days post-fertilization, intravascular injections of 3-kDa dextran–Texas Red (Invitrogen, D3328) at a concentration of 10 µg ml^{-1} were performed[127]. Five minutes after dextran injection, the larvae were fixed using 4% PFA at 4 °C overnight. The following day, larvae were washed three times (5–10 min each) with 0.1 M PBS (pH 7.4), then dehydrated in graded methanol/PBS solutions: 25% methanol (10 min), 50% methanol (10 min), 75% methanol (10 min), and finally stored in 100% methanol. For immunohistochemistry, larvae

were depigmented using freshly prepared H_2O_2–KOH solution (100 µl of 30% H_2O_2 + 100 µl of 10% KOH + 800 µl of dH_2O) for 15 min at room temperature, then rehydrated through 75%, 50% and 25% methanol in PBS (10 min each), followed by 100% PBS and three washes with 0.3% PBSTx (PBS + 0.3% Triton X-100). Blocking was performed with 10% goat serum in 0.3% PBSTx for 2 h at room temperature. Primary antibodies—anti-GFP (Abcam, ab4674, 1:2,000), anti-dextran (STEMCELL Technologies, clone DX1, 1:1,000) and anti-FN1 (Sigma-Aldrich, F3648, 1:500)—were applied in 2% goat serum in 0.3% PBSTx overnight at 4 °C. After three 10-min washes in 0.3% PBSTx, secondary antibodies (1:500) and DAPI were applied for 3 h at room temperature. Larvae were washed five times (10 min each), mounted in 1% low-melting-point agarose with 80% glycerol, and imaged using a confocal microscope. GFP-tagged FN1 expression and dextran diffusion were analyzed ($n \geq 10$ larvae per group). For mouse BBB leakage, 3-kDa dextran–Texas Red (Invitrogen, D3328) was injected into the tail vein of 20-month-old animals, which were euthanized 30 min after the injection. Brains were drop-fixed in 4% PFA, and subsequent tissue preparation was performed.

For mouse and zebrafish experiments, dextran leakage and fibronectin deposition were quantified from confocal images using ZEN software (Zeiss). Blood vessels were delineated based on CD31 immunoreactivity (mouse) or vascular fluorescence (zebrafish), and perivascular ROIs were defined relative to vessel boundaries. Extravascular dextran signal intensity and fibronectin fluorescence were quantified following background subtraction. Correlation analyses between fibronectin intensity and dextran leakage were performed on a per-animal basis using Pearson correlation. For dextran leakage analysis, the extravascular signal was quantified by excluding CD31-positive vessel lumens and measuring the surrounding parenchymal fluorescence. Analyses were restricted to small-diameter parenchymal vessels based on morphology and location, excluding large surface arteries.

Association with vascular traits

We examined variants within ±1 Mb of *FN1* for associations with cerebral small vessel disease and stroke traits using European-ancestry genome-wide association study data for white matter hyperintensities[128], perivascular spaces[129], cerebral microbleeds[130] and stroke subtypes[131]. Associations were considered significant at $P < 5 \times 10^{-8}$ and suggestive at $P < 1 \times 10^{-3}$; corresponding plasma protein associations were obtained from the UK Biobank[87]. Mendelian randomization analyses using genetically predicted FN1 proteins from 35,559 Icelanders[132] were performed with TwoSampleMR[133], including only independent *cis*-protein quantitative trait loci ($r^2 < 0.01$, $P < 5 \times 10^{-8}$). The primary method used was the inverse-variance weighted approach, with heterogeneity and pleiotropy assessed by Cochran's *Q*, MR-Egger and weighted median approaches. Significance was defined as $P < 0.005$ (ten outcomes), and directionality was confirmed using the Steiger test[134].

Spatial multiplex immunohistochemistry

Formalin-fixed, paraffin-embedded tissue blocks were obtained from the New York Brain Bank and sectioned at a thickness of 6 µm. For dewaxing and rehydration, tissue sections were submerged in CitriSolv (Decon Labs, 1601) for 20 min, followed by washing twice with 100% ethanol and once with 70% ethanol. For epitope retrieval, tissue slides were microwaved twice for 25 min each at 30% power in Tris–Cl (pH 9.0) (Abcam, ab93684) and EDTA (pH 8.5). The slides were removed from the microwave and allowed to cool. The slides were washed three times with 1× TBST (Thermo Scientific, 28360) before performing sequential immunofluorescence staining using an automated hyperplex throughput immunofluorescence machine (COMET, Lunaphore Technologies)[135]. Reagents for automated sequential immunofluorescence were prepared according to the manufacturer's instructions. Briefly, antibodies were diluted in multistaining buffer (Advanced Cell Diagnostics, BU06); imaging buffer (Advanced Cell Diagnostics, BU09) was prepared using diluent 1 (20×), diluent 2 (10×) and water; quenching buffer (Advanced Cell Diagnostics, BU08L) was prepared with solution 1 and solution 2 (10×) in water; and elution buffer (Advanced Cell Diagnostics, BU070L) was prepared by combining buffer 1 and diluent 2. All buffers were diluted to a final 1× concentration. Images were taken during each staining cycle. For quality control, autofluorescence images, negative controls (secondary antibody autofluorescence only) and post-elution images were captured. To control experimental conditions, control, AD ε3/ε3 and AD ε4/ε4 samples were run simultaneously. During the COMET run, each cycle included three primary antibodies imaged in the FITC, Cy5 and Cy7 channels. During each immunofluorescence cycle, the tissue was blocked with 1% BSA (Miltenyi Biotec, 130-091-376) for 2 min, then incubated with primary antibodies for 4 min, followed by 1 min of blocking, and finally incubated with secondary antibodies for 1 min. After each cycle, the antibody was eluted using the elution buffer and imaged for post-elution quality control. For CNS cell markers, MAP2 (1:5,000), GFAP (1:2,500), IBA1 (1:100), MBP (1:12,000), CD31 (1:50) and CD140b (1:250) were used to detect neurons, astrocytes, microglia, oligodendrocytes, endothelial cells and pericytes, respectively. Secondary antibodies—donkey anti-rabbit IgG (Thermo Fisher Scientific, A31573), anti-mouse IgG (Thermo Fisher Scientific, SA000081), anti-chicken IgY (Thermo Fisher Scientific, A78952) and anti-goat IgG (Thermo Fisher Scientific, A11055)—were used at a 1:1,000 dilution. Images were captured at 20× magnification. All images were automatically processed and aligned using the COMET software (Lunaphore Technologies), and the output was generated as a single OME-TIFF file for further analysis.

For visualization and subtraction of autofluorescence and negative controls, HORIZON Viewer (Lunaphore Technologies) software was used[136]. The images were analyzed for quantitative outcomes using HALO software (Indica Labs, PR02122) with artificial intelligence add-ons[137]. For nuclei and membrane segmentation, the software was trained based on the size, shape and intensity of DAPI and membrane markers across all cell types. For FN1 measurements, thresholds were set using the software's threshold calculation function for all images. The intensity of all stained markers across all cell types was analyzed for all subjects, and the tissue area and total cell number for each cell type and subject were normalized to the final FN1 intensity. The combined file containing datasets from all analyzed images is provided in the source data for Extended Data Fig. 3. The results were generated as CSV files. For visualization, the CSV files were processed using RStudio.

Image acquisition and quantification

Immunofluorescence images were acquired using a Zeiss LSM 800 confocal microscope with identical acquisition settings for all samples. For each histological section, five randomly selected fields were imaged. Vascular structures were delineated using established endothelial markers in ZEN software (Carl Zeiss), and fluorescence intensity, vessel area and diameter were quantified within vessel-delimited ROIs. Image acquisition and quantification were performed blinded to genotype, diagnosis and experimental conditions. Vessels exceeding 50 µm in diameter were excluded.

For mouse experiments, five fields from at least three sections per animal were analyzed. For zebrafish experiments, at least five images were acquired from a minimum of three animals per condition. Human brain analyses were performed on multiple sections per donor, with donors treated as the units of biological replication. For analyses involving repeated measurements nested within individuals (for example, vessels, ROIs, or cells within animals or human donors), statistical inference was performed using GEEs[138–140], with the individual animal or donor specified as the clustering variable. This ensured that inference was conducted at the appropriate biological unit and avoided inflation of the degrees of freedom from lower-level observations. GEEs were fitted using a Gaussian distribution with an identity link and an exchangeable working correlation structure, appropriate for imaging-based data in which repeated observations within individuals are correlated but

not ordered[138,139]. Robust (sandwich) variance estimators were used for inference. Overall effects were assessed using omnibus Wald χ^2 tests, and planned contrasts were evaluated using Wald tests from the same models. Effect sizes are reported as percentage differences with 95% confidence intervals, where applicable. The number of individuals and nested observations is reported for each analysis. For datasets without a nested structure, standard parametric or nonparametric tests were applied as appropriate, including Welch's *t* tests, Brown–Forsythe and Welch's ANOVA, or Kruskal–Wallis tests with multiple-comparison correction using the Benjamini–Krieger–Yekutieli procedure.

Colocalization analyses were performed using Mander's coefficients[141] and Pearson correlation metrics implemented in ZEN software or ImageJ/Fiji (Coloc 2 plugin), with thresholds determined using Costes' method. For FN1–AQP4 spatial proximity analyses, binary masks were generated for each channel, and Euclidean distances between FN1-positive pixels and the nearest AQP4-positive pixels were computed. For CDH5–FN1 analyses, connected vascular components were identified using connected-component labeling, excluding small objects (<50 pixels), and per-region intensities were quantified. All colocalization and proximity measurements involving nested observations were analyzed using donor- or animal-clustered GEE models. For analyses involving astrocytic markers (GFAP, FN1), fluorescence intensities were quantified within marker-defined ROIs and analyzed using donor-clustered GEE models. Correlations were assessed using Spearman's rank correlation. Statistical significance thresholds are indicated as $P < 0.05$ unless otherwise stated. No data were excluded except when tissue integrity was compromised during preparation.

Statistics and reproducibility

Sample sizes were chosen based on prior studies using similar experimental models and endpoints[12,14,39,46,112], the availability of human postmortem samples and established cohort datasets, and feasibility constraints for animal and cell culture experiments. They are reported in the corresponding figure legends and source data. Normality and equality of variance were assessed where applicable using Shapiro–Wilk tests and Brown–Forsythe or equal variance tests. When the assumptions for parametric testing were not met, nonparametric tests or variance-robust methods were used as appropriate. Data distributions are shown using individual data points in the relevant graphs.

For animal experiments, animals from the same litter or clutch, where applicable, were assigned to experimental groups before treatment. Cell culture experiments were performed using independently generated biological replicates, which were assigned to treatment conditions. No animals, human donors, biological replicates or experimental datasets were excluded from the analyses, except when samples failed technical quality control criteria during preparation and were therefore unsuitable for downstream analysis. For sequencing experiments, low-quality cells and doublets were removed during standard quality control processing before downstream analyses. Quantitative image analyses were performed blinded to experimental group allocation whenever feasible. Samples were decoded only after the completion of image acquisition and quantification.

Reporting summary

Further information on research design is available in the Nature Portfolio Reporting Summary linked to this article.

Data availability

All sequencing datasets generated in this study have been deposited in the NCBI Gene Expression Omnibus (GEO) with the following accession numbers: GSE268721, GSE268780, GSE268803 and GSE269111. Previous datasets used in this study are GSE108038 and GSE78117. The unique reagents generated in this study are available from the corresponding author upon reasonable request. Source data are provided with this paper.

References

1. Tsartsalis, S. et al. A single nuclear transcriptomic characterisation of mechanisms responsible for impaired angiogenesis and blood–brain barrier function in Alzheimer's disease. *Nat. Commun.* **15**, 2243 https://doi.org/10.1038/s41467-024-46630-z (2024).
2. Yang, A. C. et al. A human brain vascular atlas reveals diverse mediators of Alzheimer's risk. *Nature* **603**, 885–892 https://doi.org/10.1038/s41586-021-04369-3 (2022).
3. Xu, L., Nirwane, A. & Yao, Y. Basement membrane and blood–brain barrier. *Stroke Vasc. Neurol.* **4**, 78–82 https://doi.org/10.1136/svn-2018-000198 (2019).
4. Sweeney, M. D., Sagare, A. P. & Zlokovic, B. V. Blood–brain barrier breakdown in Alzheimer disease and other neurodegenerative disorders. *Nat. Rev. Neurol.* **14**, 133–150 https://doi.org/10.1038/nrneurol.2017.188 (2018).
5. Yamazaki, Y. & Kanekiyo, T. Blood–brain barrier dysfunction and the pathogenesis of Alzheimer's disease. *Int. J. Mol. Sci.* **18**, 1965 https://doi.org/10.3390/ijms18091965 (2017).
6. Zenaro, E., Piacentino, G. & Constantin, G. The blood–brain barrier in Alzheimer's disease. *Neurobiol. Dis.* **107**, 41–56 https://doi.org/10.1016/j.nbd.2016.07.007 (2017).
7. Martens, Y. A. et al. ApoE Cascade Hypothesis in the pathogenesis of Alzheimer's disease and related dementias. *Neuron* **110**, 1304–1317 https://doi.org/10.1016/j.neuron.2022.03.004 (2022).
8. Corder, E. H. et al. Gene dose of apolipoprotein E type 4 allele and the risk of Alzheimer's disease in late onset families. *Science* **261**, 921–923 https://doi.org/10.1126/science.8346443 (1993).
9. Sun, Y. et al. Role of the extracellular matrix in Alzheimer's disease. *Front. Aging Neurosci.* **13**, 707466 https://doi.org/10.3389/fnagi.2021.707466 (2021).
10. Lepelletier, F.-X., Mann, D. M. A., Robinson, A. C., Pinteaux, E. & Boutin, H. Early changes in extracellular matrix in Alzheimer's disease. *Neuropathol. Appl. Neurobiol.* **43**, 167–182 https://doi.org/10.1111/nan.12295 (2017).
11. Chu, P.-H. et al. Astrocyte-associated fibronectin promotes the proinflammatory phenotype of astrocytes through β1 integrin activation. *Mol. Cell. Neurosci.* **125**, 103848 https://doi.org/10.1016/j.mcn.2023.103848 (2023).
12. Bhattarai, P. et al. Rare genetic variation in fibronectin 1 (FN1) protects against *APOEε4* in Alzheimer's disease. *Acta Neuropathol.* **147**, 70 https://doi.org/10.1007/s00401-024-02721-1 (2024).
13. Reitz, C., Pericak-Vance, M. A., Foroud, T. & Mayeux, R. A global view of the genetic basis of Alzheimer disease. *Nat. Rev. Neurol.* **19**, 261–277 https://doi.org/10.1038/s41582-023-00789-z (2023).
14. Lee, A. J. et al. FMNL2 regulates gliovascular interactions and is associated with vascular risk factors and cerebrovascular pathology in Alzheimer's disease. *Acta Neuropathol.* **144**, 59–79 https://doi.org/10.1007/s00401-022-02431-6 (2022).
15. Luchsinger, J. A. et al. Aggregation of vascular risk factors and risk of incident Alzheimer disease. *Neurology* **65**, 545–551 https://doi.org/10.1212/01.wnl.0000172914.08967.dc (2005).
16. Tarasoff-Conway, J. M. et al. Clearance systems in the brain—implications for Alzheimer disease. *Nat. Rev. Neurol.* **11**, 457–470 https://doi.org/10.1038/nrneurol.2015.119 (2015).
17. Oveisgharan, S. et al. Frequency and underlying pathology of pure vascular cognitive impairment. *JAMA Neurol.* **79**, 1277–1286 https://doi.org/10.1001/jamaneurol.2022.3472 (2022).
18. Huynh, T.-P. V. et al. Lack of hepatic apoE does not influence early Aβ deposition: observations from a new *APOE* knock-in model. *Mol. Neurodegener.* **14**, 37 https://doi.org/10.1186/s13024-019-0337-1 (2019).

19. Montagne, A. et al. *APOE4* accelerates advanced-stage vascular and neurodegenerative disorder in old Alzheimer's mice via cyclophilin A independently of amyloid-β. *Nat. Aging* **1**, 506–520 https://doi.org/10.1038/s43587-021-00073-z (2021).
20. Jackson, R. J. et al. APOE4 derived from astrocytes leads to blood–brain barrier impairment. *Brain* **145**, 3582–3593 https://doi.org/10.1093/brain/awab478 (2022).
21. Saito, T. et al. Single *App* knock-in mouse models of Alzheimer's disease. *Nat. Neurosci.* **17**, 661–663 https://doi.org/10.1038/nn.3697 (2014).
22. Mendiola, A. S. et al. Defining blood-induced microglia functions in neurodegeneration through multiomic profiling. *Nat. Immunol.* **24**, 1173–1187 https://doi.org/10.1038/s41590-023-01522-0 (2023).
23. Ryu, J. K. & McLarnon, J. G. A leaky blood–brain barrier, fibrinogen infiltration and microglial reactivity in inflamed Alzheimer's disease brain. *J. Cell. Mol. Med.* **13**, 2911–2925 https://doi.org/10.1111/j.1582-4934.2008.00434.x (2009).
24. Sun, N. et al. Single-nucleus multiregion transcriptomic analysis of brain vasculature in Alzheimer's disease. *Nat. Neurosci.* **26**, 970–982 https://doi.org/10.1038/s41593-023-01334-3 (2023).
25. Kim, Y. A., Mellen, M., Kizil, C. & Santa-Maria, I. Mechanisms linking cerebrovascular dysfunction and tauopathy: adding a layer of epiregulatory complexity. *Br. J. Pharmacol.* **181**, 879–895 https://doi.org/10.1111/bph.16280 (2024).
26. Pantazis, C. B. et al. A reference human induced pluripotent stem cell line for large-scale collaborative studies. *Cell Stem Cell* **29**, 1685–1702 https://doi.org/10.1016/j.stem.2022.11.004 (2022).
27. Bertucci, T. et al. Direct differentiation of human pluripotent stem cells into vascular network along with supporting mural cells. *APL Bioeng.* **7**, 036107 https://doi.org/10.1063/5.0155207 (2023).
28. Yilmaz, E. et al. Single-nucleus multiomics in brains from Hispanic individuals reveal *APOE-ε4*-driven disruption of focal adhesion signaling in the presence of cerebrovascular pathology. Preprint at *medRxiv* https://doi.org/10.1101/2025.05.21.25328040 (2025).
29. Jackson, R. J., Hyman, B. T. & Serrano-Pozo, A. Multifaceted roles of APOE in Alzheimer disease. *Nat. Rev. Neurol.* **20**, 457–474 https://doi.org/10.1038/s41582-024-00988-2 (2024).
30. Kaji, S. et al. Apolipoprotein E aggregation in microglia initiates Alzheimer's disease pathology by seeding β-amyloidosis. *Immunity* **57**, 2651–2668 https://doi.org/10.1016/j.immuni.2024.09.014 (2024).
31. Riphagen, J. M. et al. Linking APOE-ε4, blood–brain barrier dysfunction, and inflammation to Alzheimer's pathology. *Neurobiol. Aging* **85**, 96–103 https://doi.org/10.1016/j.neurobiolaging.2019.09.020 (2020).
32. de Leeuw, S. M. et al. APOE2, E3, and E4 differentially modulate cellular homeostasis, cholesterol metabolism, and inflammatory response in isogenic iPSC-derived astrocytes. *Stem Cell Rep.* **17**, 110–126 https://doi.org/10.1016/j.stemcr.2021.11.007 (2022).
33. Sottile, J. et al. Fibronectin-dependent collagen I deposition modulates the cell response to fibronectin. *Am. J. Physiol.* **293**, C1934–C1946 https://doi.org/10.1152/ajpcell.00130.2007 (2007).
34. Siddiqui, T. et al. Three-dimensional biohybrid starPEG–heparin hydrogel cultures for modeling human neuronal development and Alzheimer's disease pathology. *Methods Mol. Biol.* **2561**, 159–170 https://doi.org/10.1007/978-1-0716-2655-9_8 (2023).
35. Siddiqui, T. et al. Nerve growth factor receptor (Ngfr) induces neurogenic plasticity by suppressing reactive astroglial Lcn2/Slc22a17 signaling in Alzheimer's disease. *NPJ Regen. Med.* **8**, 33 https://doi.org/10.1038/s41536-023-00311-5 (2023).
36. Siddiqui, T. et al. KYNA/Ahr signaling suppresses neural stem cell plasticity and neurogenesis in adult zebrafish model of Alzheimer's disease. *Cells* **10**, 2748 https://doi.org/10.3390/cells10102748 (2021).
37. Papadimitriou, C. et al. 3D culture method for Alzheimer's disease modeling reveals interleukin-4 rescues Aβ42-induced loss of human neural stem cell plasticity. *Dev. Cell* **46**, 85–101 https://doi.org/10.1016/j.devcel.2018.06.005 (2018).
38. Green, G. S. et al. Cellular communities reveal trajectories of brain ageing and Alzheimer's disease. *Nature* **633**, 634–645 https://doi.org/10.1038/s41586-024-07871-6 (2024).
39. Haage, V. et al. A pharmacological toolkit for human microglia identifies topoisomerase I inhibitors as immunomodulators for Alzheimer's disease. Preprint at *bioRxiv* https://doi.org/10.1101/2024.02.06.579103 (2024).
40. İs, Ö. et al. Gliovascular transcriptional perturbations in Alzheimer's disease reveal molecular mechanisms of blood brain barrier dysfunction. *Nat. Commun.* **15**, 4758 https://doi.org/10.1038/s41467-024-48926-6 (2024).
41. Turgutalp, B. & Kizil, C. Multi-target drugs for Alzheimer's disease. *Trends Pharmacol. Sci.* **45**, 628–638 https://doi.org/10.1016/j.tips.2024.05.005 (2024).
42. Bhattarai, P., Turgutalp, B. & Kizil, C. Zebrafish as an experimental and preclinical model for Alzheimer's disease. *ACS Chem. Neurosci.* **13**, 2939–2941 https://doi.org/10.1021/acschemneuro.2c00583 (2022).
43. Bhattarai, P. et al. Neuron–glia interaction through serotonin–BDNF–NGFR axis enables regenerative neurogenesis in Alzheimer's model of adult zebrafish brain. *PLoS Biol.* **18**, e3000585 https://doi.org/10.1371/journal.pbio.3000585 (2020).
44. Jurisch-Yaksi, N., Yaksi, E. & Kizil, C. Radial glia in the zebrafish brain: functional, structural, and physiological comparison with the mammalian glia. *Glia* **68**, 2451–2470 https://doi.org/10.1002/glia.23849 (2020).
45. Cosacak, M. I. et al. Single-cell transcriptomics analyses of neural stem cell heterogeneity and contextual plasticity in a zebrafish brain model of amyloid toxicity. *Cell Rep.* **27**, 1307–1318 https://doi.org/10.1016/j.celrep.2019.03.090 (2019).
46. Bhattarai, P. et al. IL4/STAT6 signaling activates neural stem cell proliferation and neurogenesis upon amyloid-β42 aggregation in adult zebrafish brain. *Cell Rep.* **17**, 941–948 https://doi.org/10.1016/j.celrep.2016.09.075 (2016).
47. Guillon, E. et al. Fibronectin is a smart adhesive that both influences and responds to the mechanics of early spinal column development. *eLife* **9**, e48964 https://doi.org/10.7554/eLife.48964 (2020).
48. Yang, H.-S. et al. Plasma VEGFA and PGF impact longitudinal tau and cognition in preclinical Alzheimer's disease. *Brain* **147**, 2158–2168 https://doi.org/10.1093/brain/awae034 (2024).
49. Shen, F. et al. Coexpression of angiopoietin-1 with VEGF increases the structural integrity of the blood–brain barrier and reduces atrophy volume. *J. Cereb. Blood Flow Metab.* **31**, 2343–2351 https://doi.org/10.1038/jcbfm.2011.97 (2011).
50. Daneman, R. & Prat, A. The blood–brain barrier. *Cold Spring Harb. Perspect. Biol.* **7**, a020412 https://doi.org/10.1101/cshperspect.a020412 (2015).
51. Woronicz, J. D., Gao, X., Cao, Z., Rothe, M. & Goeddel, D. V. IκB kinase-β: NF-κB activation and complex formation with IκB kinase-α and NIK. *Science* **278**, 866–869 https://doi.org/10.1126/science.278.5339.866 (1997).
52. Kiriakidis, S. et al. VEGF expression in human macrophages is NF-κB-dependent: studies using adenoviruses expressing the endogenous NF-κB inhibitor IκBα and a kinase-defective form of the IκB kinase 2. *J. Cell Sci.* **116**, 665–674 https://doi.org/10.1242/jcs.00286 (2003).
53. Mathys, H. et al. Single-cell atlas reveals correlates of high cognitive function, dementia, and resilience to Alzheimer's disease pathology. *Cell* **186**, 4365–4385 https://doi.org/10.1016/j.cell.2023.08.039 (2023).

54. Mathys, H. et al. Single-cell transcriptomic analysis of Alzheimer's disease. *Nature* **570**, 332–337 https://doi.org/10.1038/s41586-019-1195-2 (2019).
55. Lake, B. B. et al. Neuronal subtypes and diversity revealed by single-nucleus RNA sequencing of the human brain. *Science* **352**, 1586–1590 https://doi.org/10.1126/science.aaf1204 (2016).
56. İs, Ö. et al. Multi layered omics approaches reveal glia specific alterations in Alzheimer's disease: a systematic review and future prospects. *Glia* **73**, 539–573 https://doi.org/10.1002/glia.24652 (2024).
57. Serrano-Pozo, A. et al. Astrocyte transcriptomic changes along the spatiotemporal progression of Alzheimer's disease. *Nat. Neurosci.* **27**, 2384–2400 https://doi.org/10.1038/s41593-024-01791-4 (2024).
58. Schumacher, S. et al. Structural insights into integrin $\alpha_5\beta_1$ opening by fibronectin ligand. *Sci. Adv.* **7**, eabe9716 https://doi.org/10.1126/sciadv.abe9716 (2021).
59. Guan, J. L. Role of focal adhesion kinase in integrin signaling. *Int. J. Biochem. Cell Biol.* **29**, 1085–1096 https://doi.org/10.1016/s1357-2725(97)00051-4 (1997).
60. Vardarajan, B. N. et al. Age-specific incidence rates for dementia and Alzheimer disease in NIA-LOAD/NCRAD and EFIGA families: National Institute on Aging Genetics Initiative for Late-Onset Alzheimer Disease/National Cell Repository for Alzheimer Disease (NIA-LOAD/NCRAD) and Estudio Familiar de Influencia Genetica en Alzheimer (EFIGA). *JAMA Neurol.* **71**, 315–323 https://doi.org/10.1001/jamaneurol.2013.5570 (2014).
61. Lawson, N. D. & Weinstein, B. M. In vivo imaging of embryonic vascular development using transgenic zebrafish. *Dev. Biol.* **248**, 307–318 https://doi.org/10.1006/dbio.2002.0711 (2002).
62. Galant, S. et al. Embryonic origin and lineage hierarchies of the neural progenitor subtypes building the zebrafish adult midbrain. *Dev. Biol.* **420**, 120–135 https://doi.org/10.1016/j.ydbio.2016.09.022 (2016).
63. Rivera, C. G., Mellberg, S., Claesson-Welsh, L., Bader, J. S. & Popel, A. S. Analysis of VEGF-A regulated gene expression in endothelial cells to identify genes linked to angiogenesis. *PLoS ONE* **6**, e24887 https://doi.org/10.1371/journal.pone.0024887 (2011).
64. Schweighofer, B. et al. The VEGF-induced transcriptional response comprises gene clusters at the crossroad of angiogenesis and inflammation. *Thromb. Haemost.* **102**, 544–554 https://doi.org/10.1160/th08-12-0830 (2009).
65. Jin, K. et al. Heparin-binding epidermal growth factor-like growth factor: hypoxia-inducible expression in vitro and stimulation of neurogenesis in vitro and in vivo. *J. Neurosci.* **22**, 5365–5373 https://doi.org/10.1523/jneurosci.22-13-05365.2002 (2002).
66. Linnerbauer, M. et al. The astrocyte-produced growth factor HB-EGF limits autoimmune CNS pathology. *Nat. Immunol.* **25**, 432–447 https://doi.org/10.1038/s41590-024-01756-6 (2024).
67. Mehta, V. B. & Besner, G. E. HB-EGF promotes angiogenesis in endothelial cells via PI3-kinase and MAPK signaling pathways. *Growth Factors* **25**, 253–263 https://doi.org/10.1080/08977190701773070 (2007).
68. Liu, B., Chen, H., Johns, T. G. & Neufeld, A. H. Epidermal growth factor receptor activation: an upstream signal for transition of quiescent astrocytes into reactive astrocytes after neural injury. *J. Neurosci.* **26**, 7532–7540 https://doi.org/10.1523/jneurosci.1004-06.2006 (2006).
69. Roudabush, F. L., Pierce, K. L., Maudsley, S., Khan, K. D. & Luttrell, L. M. Transactivation of the EGF receptor mediates IGF-1-stimulated Shc phosphorylation and ERK1/2 activation in COS-7 cells. *J. Biol. Chem.* **275**, 22583–22589 https://doi.org/10.1074/jbc.m002915200 (2000).
70. Reid, M. M. et al. Human brain vascular multi-omics elucidates disease-risk associations. *Neuron* **113**, 3143–3161 https://doi.org/10.1016/j.neuron.2025.07.001 (2025).
71. Du, H. et al. Relationship between insulin-like growth factor-1 and cerebral small vessel disease and its mechanisms: advances in the field. *Front. Aging Neurosci.* **15**, 1190869 https://doi.org/10.3389/fnagi.2023.1190869 (2023).
72. Hayes, C. A., Valcarcel-Ares, M. N. & Ashpole, N. M. Preclinical and clinical evidence of IGF-1 as a prognostic marker and acute intervention with ischemic stroke. *J. Cereb. Blood Flow Metab.* **41**, 2475–2491 https://doi.org/10.1177/0271678x211000894 (2021).
73. Tarantini, S. et al. IGF1R signaling regulates astrocyte-mediated neurovascular coupling in mice: implications for brain aging. *GeroScience* **43**, 901–911 https://doi.org/10.1007/s11357-021-00350-0 (2021).
74. Montagne, A. et al. *APOE4* leads to blood–brain barrier dysfunction predicting cognitive decline. *Nature* **581**, 71–76 https://doi.org/10.1038/s41586-020-2247-3 (2020).
75. Toth, P., Tarantini, S., Csiszar, A. & Ungvari, Z. Functional vascular contributions to cognitive impairment and dementia: mechanisms and consequences of cerebral autoregulatory dysfunction, endothelial impairment, and neurovascular uncoupling in aging. *Am. J. Physiol.* **312**, H1–H20 https://doi.org/10.1152/ajpheart.00581.2016 (2017).
76. Iadecola, C. The neurovascular unit coming of age: a journey through neurovascular coupling in health and disease. *Neuron* **96**, 17–42 https://doi.org/10.1016/j.neuron.2017.07.030 (2017).
77. Braak, H. & Braak, E. Neuropathological stageing of Alzheimer-related changes. *Acta Neuropathol.* **82**, 239–259 https://doi.org/10.1007/bf00308809 (1991).
78. Ma, Y. et al. Epigenetic and genetic risk of Alzheimer disease from autopsied brains in two ethnic groups. *Acta Neuropathol.* **148**, 27 https://doi.org/10.1007/s00401-024-02778-y (2024).
79. Cosacak, M. I. et al. Single cell/nucleus transcriptomics comparison in zebrafish and humans reveals common and distinct molecular responses to Alzheimer's disease. *Cells* **11**, 1807 https://doi.org/10.3390/cells11111807 (2022).
80. Wang, X. et al. Deciphering cellular transcriptional alterations in Alzheimer's disease brains. *Mol. Neurodegener.* **15**, 38 https://doi.org/10.1186/s13024-020-00392-6 (2020).
81. Cao, L. et al. Detection of an integrin-binding mechanoswitch within fibronectin during tissue formation and fibrosis. *ACS Nano* **11**, 7110–7117 https://doi.org/10.1021/acsnano.7b02755 (2017).
82. Noda, Y. et al. Fibronectin type III domain-containing protein 5 interacts with APP and decreases amyloid β production in Alzheimer's disease. *Mol. Brain* **11**, 61 https://doi.org/10.1186/s13041-018-0401-8 (2018).
83. Chhum, P. et al. Consequences of glycine mutations in the fibronectin-binding sequence of collagen. *J. Biol. Chem.* **291**, 27073–27086 https://doi.org/10.1074/jbc.m116.753566 (2016).
84. Zou, L., Cao, S., Kang, N., Huebert, R. C. & Shah, V. H. Fibronectin induces endothelial cell migration through β_1 integrin and Src-dependent phosphorylation of fibroblast growth factor receptor-1 at tyrosines 653/654 and 766. *J. Biol. Chem.* **287**, 7190–7202 https://doi.org/10.1074/jbc.m111.304972 (2012).
85. Thomsen, M. S., Routhe, L. J. & Moos, T. The vascular basement membrane in the healthy and pathological brain. *J. Cereb. Blood Flow Metab.* **37**, 3300–3317 https://doi.org/10.1177/0271678x17722436 (2017).
86. Askenazi, M. et al. Compilation of reported protein changes in the brain in Alzheimer's disease. *Nat. Commun.* **14**, 4466 https://doi.org/10.1038/s41467-023-40208-x (2023).

87. Sun, B. B. et al. Plasma proteomic associations with genetics and health in the UK Biobank. *Nature* **622**, 329–338 https://doi.org/10.1038/s41586-023-06592-6 (2023).
88. Schuldt, B. R. et al. APOE4 promotes cerebrovascular fibrosis and amyloid deposition via a pericyte-to-myofibroblast transition. Preprint at *bioRxiv* https://doi.org/10.1101/2025.09.04.674192 (2025).
89. De Silva, T. M. & Faraci, F. M. Contributions of aging to cerebral small vessel disease. *Annu. Rev. Physiol.* **82**, 275–295 https://doi.org/10.1146/annurev-physiol-021119-034338 (2020).
90. Carmeliet, P. & de Almodovar, C. R. VEGF ligands and receptors: implications in neurodevelopment and neurodegeneration. *Cell. Mol. Life Sci.* **70**, 1763–1778 https://doi.org/10.1007/s00018-013-1283-7 (2013).
91. Tang, H., Mao, X., Xie, L., Greenberg, D. A. & Jin, K. Expression level of vascular endothelial growth factor in hippocampus is associated with cognitive impairment in patients with Alzheimer's disease. *Neurobiol. Aging* **34**, 1412–1415 https://doi.org/10.1016/j.neurobiolaging.2012.10.029 (2013).
92. Chen, X. et al. Cerebral amyloid angiopathy is associated with glymphatic transport reduction and time-delayed solute drainage along the neck arteries. *Nat. Aging* **2**, 214–223 https://doi.org/10.1038/s43587-022-00181-4 (2022).
93. Da Mesquita, S., Fu, Z. & Kipnis, J. The meningeal lymphatic system: a new player in neurophysiology. *Neuron* **100**, 375–388 https://doi.org/10.1016/j.neuron.2018.09.022 (2018).
94. Faber-Elman, A., Solomon, A., Abraham, J. A., Marikovsky, M. & Schwartz, M. Involvement of wound-associated factors in rat brain astrocyte migratory response to axonal injury: in vitro simulation. *J. Clin. Invest.* **97**, 162–171 https://doi.org/10.1172/jci118385 (1996).
95. Schwartz, M., Kipnis, J., Rivest, S. & Prat, A. How do immune cells support and shape the brain in health, disease, and aging? *J. Neurosci.* **33**, 17587–17596 https://doi.org/10.1523/jneurosci.3241-13.2013 (2013).
96. Keller, J. N. et al. Plasma proteomics of genetic brain arteriosclerosis and dementia syndrome identifies signatures of fibrosis, angiogenesis, and metabolic alterations. Preprint at *bioRxiv* https://doi.org/10.1101/2024.03.28.587249 (2025).
97. Franks, A., Airoldi, E. & Slavov, N. Post-transcriptional regulation across human tissues. *PLoS Comput. Biol.* **13**, e1005535 https://doi.org/10.1371/journal.pcbi.1005535 (2017).
98. Kameyama, T. et al. Heterogeneity of perivascular astrocyte endfeet depending on vascular regions in the mouse brain. *iScience* **26**, 108010 https://doi.org/10.1016/j.isci.2023.108010 (2023).
99. Hösli, L. et al. Direct vascular contact is a hallmark of cerebral astrocytes. *Cell Rep.* **39**, 110599 https://doi.org/10.1016/j.celrep.2022.110599 (2022).
100. Zhang, Y. et al. Purification and characterization of progenitor and mature human astrocytes reveals transcriptional and functional differences with mouse. *Neuron* **89**, 37–53 https://doi.org/10.1016/j.neuron.2015.11.013 (2016).
101. Lin, Y.-T. et al. *APOE4* causes widespread molecular and cellular alterations associated with Alzheimer's disease phenotypes in human iPSC-derived brain cell types. *Neuron* **98**, 1141–1154 https://doi.org/10.1016/j.neuron.2018.05.008 (2018).
102. Reas, E. T. et al. *APOE* ε4-related blood–brain barrier breakdown is associated with microstructural abnormalities. *Alzheimers Dement.* **20**, 8615–8624 https://doi.org/10.1002/alz.14302 (2024).
103. Reho, P. et al. Rare FN1 missense mutations indicate a protective role against Lewy body dementia in APOEε4 homozygous carriers. *Acta Neuropathol.* **150**, 22 https://doi.org/10.1007/s00401-025-02925-z (2025).
104. Salloway, S. et al. Effect of APOE genotype on microvascular basement membrane in Alzheimer's disease. *J. Neurol. Sci.* **203–204**, 183–187 https://doi.org/10.1016/s0022-510x(02)00288-5 (2002).
105. Waldvogel, H. J., Curtis, M. A., Baer, K., Rees, M. I. & Faull, R. L. Immunohistochemical staining of post-mortem adult human brain sections. *Nat. Protoc.* **1**, 2719–2732 https://doi.org/10.1038/nprot.2006.354 (2006).
106. Sullivan, P. M. et al. Targeted replacement of the mouse apolipoprotein E gene with the common human *APOE3* allele enhances diet-induced hypercholesterolemia and atherosclerosis. *J. Biol. Chem.* **272**, 17972–17980 https://doi.org/10.1074/jbc.272.29.17972 (1997).
107. Nuriel, T. et al. Neuronal hyperactivity due to loss of inhibitory tone in *APOE4* mice lacking Alzheimer's disease-like pathology. *Nat. Commun.* **8**, 1464 https://doi.org/10.1038/s41467-017-01444-0 (2017).
108. Jin, S.-W., Beis, D., Mitchell, T., Chen, J.-N. & Stainier, D. Y. R. Cellular and molecular analyses of vascular tube and lumen formation in zebrafish. *Development* **132**, 5199–5209 https://doi.org/10.1242/dev.02087 (2005).
109. Cosacak, M. I., Bhattarai, P. & Kizil, C. Protocol for dissection and dissociation of zebrafish telencephalon for single-cell sequencing. *STAR Protoc.* **1**, 100042 https://doi.org/10.1016/j.xpro.2020.100042 (2020).
110. Bhattarai, P., Thomas, A. K., Zhang, Y. & Kizil, C. The effects of aging on Amyloid-β42-induced neurodegeneration and regeneration in adult zebrafish brain. *Neurogenesis* **4**, e1322666 https://doi.org/10.1080/23262133.2017.1322666 (2017).
111. Bhattarai, P. et al. Modeling amyloid-β42 toxicity and neurodegeneration in adult zebrafish brain. *J. Vis. Exp.* https://doi.org/10.3791/56014 (2017).
112. Tayran, H. et al. ABCA7-dependent induction of neuropeptide Y is required for synaptic resilience in Alzheimer's disease through BDNF/NGFR signaling. *Cell Genom.* **4**, 100642 https://doi.org/10.1016/j.xgen.2024.100642 (2024).
113. Schmid, K. T. et al. scPower accelerates and optimizes the design of multi-sample single cell transcriptomic studies. *Nat. Commun.* **12**, 6625 https://doi.org/10.1038/s41467-021-26779-7 (2021).
114. Zheng, G. X. Y. et al. Haplotyping germline and cancer genomes with high-throughput linked-read sequencing. *Nat. Biotechnol.* **34**, 303–311 https://doi.org/10.1038/nbt.3432 (2016).
115. Raj, B. et al. Simultaneous single-cell profiling of lineages and cell types in the vertebrate brain. *Nat. Biotechnol.* **36**, 442–450 https://doi.org/10.1038/nbt.4103 (2018).
116. Butler, A., Hoffman, P., Smibert, P., Papalexi, E. & Satija, R. Integrating single-cell transcriptomic data across different conditions, technologies, and species. *Nat. Biotechnol.* **36**, 411–420 https://doi.org/10.1038/nbt.4096 (2018).
117. McGinnis, C. S., Murrow, L. M. & Gartner, Z. J. DoubletFinder: doublet detection in single-cell RNA sequencing data using artificial nearest neighbors. *Cell Syst.* **8**, 329–337 https://doi.org/10.1016/j.cels.2019.03.003 (2019).
118. Tcw, J. et al. Cholesterol and matrisome pathways dysregulated in astrocytes and microglia. *Cell* **185**, 2213–2233 https://doi.org/10.1016/j.cell.2022.05.017 (2022).
119. Ray, N. R. et al. Local genetic covariance analysis with lipid traits identifies novel loci for early-onset Alzheimer's disease. *PLoS Genet.* **21**, e1011631 https://doi.org/10.1371/journal.pgen.1011631 (2025).
120. Yeo, S.-Y., Kim, M., Kim, H.-S., Huh, T.-L. & Chitnis, A. B. Fluorescent protein expression driven by *her4* regulatory elements reveals the spatiotemporal pattern of Notch signaling in the nervous system of zebrafish embryos. *Dev. Biol.* **301**, 555–567 https://doi.org/10.1016/j.ydbio.2006.10.020 (2007).

121. Biswas, S., Ghosh, S. & Maitra, S. Role of insulin-like growth factor 1 (IGF1) in the regulation of mitochondrial bioenergetics in zebrafish oocytes: lessons from in vivo and in vitro investigations. *Front. Cell Dev. Biol.* **11**, 1202693 https://doi.org/10.3389/fcell.2023.1202693 (2023).
122. Heiss, J. A. & Just, A. C. Improved filtering of DNA methylation microarray data by detection *p* values and its impact on downstream analyses. *Clin. Epigenetics* **11**, 15 https://doi.org/10.1186/s13148-019-0615-3 (2019).
123. McCartney, D. L. et al. Identification of polymorphic and off-target probe binding sites on the Illumina Infinium MethylationEPIC BeadChip. *Genom. Data* **9**, 22–24 https://doi.org/10.1016/j.gdata.2016.05.012 (2016).
124. De Jager, P. L. et al. A multi-omic atlas of the human frontal cortex for aging and Alzheimer's disease research. *Sci. Data* **5**, 180142 https://doi.org/10.1038/sdata.2018.142 (2018).
125. Tingley, D., Yamamoto, T., Hirose, K., Keele, L. & Imai, K. mediation: R package for causal mediation analysis. *J. Stat. Softw.* **59**, 1–38 https://doi.org/10.18637/jss.v059.i05 (2014).
126. Rossnagl, S. et al. EDA-fibronectin originating from osteoblasts inhibits the immune response against cancer. *PLoS Biol.* **14**, e1002562 https://doi.org/10.1371/journal.pbio.1002562 (2016).
127. O'Brown, N. M., Megason, S. G. & Gu, C. Suppression of transcytosis regulates zebrafish blood–brain barrier function. *eLife* **8**, e47326 https://doi.org/10.7554/eLife.47326 (2019).
128. Sargurupremraj, M. et al. Cerebral small vessel disease genomics and its implications across the lifespan. *Nat. Commun.* **11**, 6285 https://doi.org/10.1038/s41467-020-19111-2 (2020).
129. Duperron, M.-G. et al. Genomics of perivascular space burden unravels early mechanisms of cerebral small vessel disease. *Nat. Med.* **29**, 950–962 https://doi.org/10.1038/s41591-023-02268-w (2023).
130. Knol, M. J. et al. Association of common genetic variants with brain microbleeds: a genome-wide association study. *Neurology* **95**, e3331–e3343 https://doi.org/10.1212/wnl.0000000000010852 (2020).
131. Mishra, A. et al. Stroke genetics informs drug discovery and risk prediction across ancestries. *Nature* **611**, 115–123 https://doi.org/10.1038/s41586-022-05165-3 (2022).
132. Ferkingstad, E. et al. Large-scale integration of the plasma proteome with genetics and disease. *Nat. Genet.* **53**, 1712–1721 https://doi.org/10.1038/s41588-021-00978-w (2021).
133. Hemani, G. et al. The MR-Base platform supports systematic causal inference across the human phenome. *eLife* **7**, e34408 https://doi.org/10.7554/eLife.34408 (2018).
134. Burgess, S. et al. Guidelines for performing Mendelian randomization investigations: update for summer 2023. *Wellcome Open Res.* **4**, 186 https://doi.org/10.12688/wellcomeopenres.15555.3 (2019).
135. Najem, H. et al. High dimensional proteomic multiplex imaging of the central nervous system using the COMET™ system. Preprint at *bioRxiv* https://doi.org/10.1101/2025.02.14.638299 (2025).
136. Cakmak, P. et al. Spatial immune profiling defines a subset of human gliomas with functional tertiary lymphoid structures. *Immunity* **58**, 2847–2863 https://doi.org/10.1016/j.immuni.2025.09.018 (2025).
137. Rivest, F. et al. Fully automated sequential immunofluorescence (seqIF) for hyperplex spatial proteomics. *Sci. Rep.* **13**, 16994 https://doi.org/10.1038/s41598-023-43435-w (2023).
138. Zeger, S. L., Liang, K.-Y. & Albert, P. S. Models for longitudinal data: a generalized estimating equation approach. *Biometrics* **44**, 1049–1060 https://doi.org/10.2307/2531734 (1988).
139. Liang, K.-Y. & Zeger, S. L. Longitudinal data analysis using generalized linear models. *Biometrika* **73**, 13–22 https://doi.org/10.1093/biomet/73.1.13 (1986).
140. Galbraith, S., Daniel, J. A. & Vissel, B. A study of clustered data and approaches to its analysis. *J. Neurosci.* **30**, 10601–10608 https://doi.org/10.1523/jneurosci.0362-10.2010 (2010).
141. Dunn, K. W., Kamocka, M. M. & McDonald, J. H. A practical guide to evaluating colocalization in biological microscopy. *Am. J. Physiol.* **300**, C723–C742 https://doi.org/10.1152/ajpcell.00462.2010 (2011).
142. Hall, T. E. et al. In vivo cell biological screening identifies an endocytic capture mechanism for T-tubule formation. *Nat. Commun.* **11**, 3711 https://doi.org/10.1038/s41467-020-17486-w (2020).

Acknowledgements

We would like to thank the Molecular Pathology Shared Resource (MPSR) and the Flow Cytometry Core Facility (Columbia Center for Translational Immunology, supported in part by the Office of the Director, National Institutes of Health (NIH), under award S10OD020056) platforms of the Columbia University Herbert Irving Comprehensive Cancer Center for procedural support; the New York Brain Bank for postmortem human brain sections; the Taub Institute Imaging Platform; and the DRESDEN-Concept Genome Center for total RNA sequencing of 3D cultures or pHAs. We thank the contributors who collected samples used in this study, as well as the patients and their families for their participation, without whom this work would not have been possible. We thank S. A. Hussaini, G. A. Rodriguez and D. Flaherty (New York Brain Bank) for postmortem brain samples; M. Kissner (Columbia Stem Cell Initiative Flow Cytometry Core Facility) for his help during sorting; and E. Bush (Single Cell Analysis Core and Columbia Genome Center, Sulzberger Genome Center). Fibronectin-human-EDA in pMAX, which was used to generate the human FN1 overexpression plasmid for zebrafish, was a gift from I. Nakchbandi (Addgene plasmid no. 120402; https://n2t.net/addgene:120402; RRID:Addgene_120402)[126]. nls-transposase-nls-pA in pT3TS-Dest was a gift from R. Parton (Addgene plasmid no. 140873; https://n2t.net/addgene:140873; RRID:Addgene_140873)[142]. Authors from the Neural Stem Cell Institute (D.M., E.S.F., K.T., T.B., S.T.) gratefully acknowledge the Albany Medical College Imaging Core Facility for providing access to Imaris software.
The National Institute on Aging–Alzheimer's Disease Family-Based Study (NIA–AD FBS; https://www.neurology.columbia.edu/research/research-centers-and-programs/national-institute-aging-alzheimers-disease-family-based-study-nia-ad-fbs) collected the samples used in this study and is supported by the National Institute on Aging (NIA) grants U24AG026395, U24AG021886, R01AG041797 and U24AG056270. Additional families were contributed to the NIA–AD FBS through the NIH grants R01AG028786, R01AG027944, RF1AG054074 and U01AG052410. The NIA–AD FBS began in 2003 with the goal of recruiting large, multiply affected families with late-onset Alzheimer's disease (AD) for genetic research. The study created a resource of well-characterized families with late-onset AD. The initial phases of the Alzheimer's Disease Sequencing Project (ADSP) included genotyping hundreds of participants from the NIA–AD FBS. The ADSP Follow-Up Study heavily relies on resources provided by the NIA–AD FBS and depends on the longitudinal follow-up of families, as well as the collection of additional families, particularly those from diverse populations. Samples include biological materials for genome-wide association studies and whole-genome sequencing; peripheral blood mononuclear cells for stem cell modeling; plasma for studies of metabolomics, proteomics and biomarker research; and brain autopsy materials for bulk RNA sequencing.
Estudio Familiar de Influencia Genetica en Alzheimer (EFIGA) is a study of sporadic and familial AD among Caribbean Hispanics recruited from clinics in the Dominican Republic and New York (R01 AG067501). The goal of this study is to identify genetic variants that increase the risk of late-onset AD in this ethnic group. This study was initiated in

1998 and recruited individuals and their families from New York as well as from clinics in the Dominican Republic. Recruitment for the EFIGA study began in 1998 to investigate the genetic architecture of AD in the Caribbean Hispanic population. Patients with familial AD were recruited. If a sibling of the proband had dementia, all other living siblings and available relatives underwent evaluation. Cases were defined as any individual meeting the NINCDS-ADRDA criteria for probable or possible AD.

The results published here are, in part, based on data obtained from the AD Knowledge Portal (https://adknowledgeportal.org). The Mayo RNAseq Study was led by N.E.-T. (Mayo Clinic, Jacksonville, FL), as part of the multi-principal investigator grant U01 AG046139 (principal investigators: Golde, Ertekin-Taner, Younkin, Price) using samples from the Mayo Clinic Brain Bank.

Author contributions

P.B., E.Y., B.N.V., R.M. and C.K. conceived and designed this study. P.B., E.Y., H.T. and C.K. performed human and zebrafish brain immunolabeling, quantitative assays, image acquisition, quantification and statistical analyses. E.Y., P.B. and C.K. performed single-cell transcriptomic analysis in zebrafish. N.N. performed zebrafish brain tissue sectioning. A.F.T. provided the human brain samples. A.J.L., B.N.V. and R.M. provided human datasets and analytical samples. Y.M. performed methylation analyses. V.H. and P.L.D.J. provided the microglial activity blocking compound. X.W., Ö.İ. and N.E.-T. integrated human single-nucleus datasets. W.L. and Y.Z. provided the TNF blocking compound. T.N. provided mouse brain tissues and performed in vivo mouse procedures. H.Y.K. and P.B. prepared the mouse brain tissues and performed staining. S.A.H. and D.J. provided the *fn1b* knockout zebrafish. H.C. and C.K. conducted 3D pHA experiments and analyses. H.C., M.I.C. and C.K. performed bulk RNA sequencing in 3D cultures and data analyses. I.H., J.O.E. and H.P. performed multiplex immunostaining, analyses and quantifications on human brain tissue. E.Ö.C., B.T., S.M.d.L. and C.K. performed isogenic iPS cell-derived astrocyte cultures, astrocytic differentiation, immunocytochemistry, imaging and quantification. C.W. and U.F. provided hydrogel materials. T.B., D.M., E.S.F., K.T. and S.T. performed 2D iPS cell-derived endothelial cell and 3D VAMP modeling of isogenic line pairs, conducted RT–qPCR on 2D endothelial cells, carried out western blot and immunohistochemical analyses on VAMP models, quantified the samples and collected relevant data. R.P. and P.S.G.-H. performed co-immunoprecipitation and acquired the relevant data. Q.L.-G. and S.D. performed genetic association and Mendelian randomization analyses of FN1 in cerebral small-vessel disease and stroke datasets. J.N.K. and F.M.E. performed statistical analyses of CSF FN1 levels and astrocytic NFKB1 and FN1–VEGFA expression in human samples. Authors contributed to the interpretation of their results and methodologies. P.B., E.Y., B.N.V., R.M. and C.K. generated the figures and wrote the original paper. All authors were given the opportunity to review and approve the final version of the paper before submission.

Funding

This work was supported by the National Institute on Aging R01 AG067501 (Genetic Epidemiology and Multi-Omics Analyses in Familial and Sporadic Alzheimer's Disease Among Secular Caribbean Hispanics and Religious Order) (R.M., B.N.V., C.K.); the National Institute on Aging RF1 AG066107 (Epidemiological Integration of Genetic Variants and Metabolomics Profiles in Washington Heights Columbia Aging Project) (R.M., B.N.V., C.K.); the Schaefer Research Scholars Award (C.K.); the Taub Institute Grants for Emerging Research (TIGER) (C.K.); the Thompson Family Foundation Program for Accelerated Medicine Exploration in Alzheimer's Disease and Related Disorders of the Nervous System (TAME-AD) (C.K.); the American Brain Foundation Cure-One-Cure-Many Award (C.K.); the Carol and Gene Ludwig Family Foundation (C.K., A.J.L., B.N.V.); the Toffler Scholar Program (P.B.); P30 AG066462 Alzheimer's Disease Research Center (A.F.T.); the National Institute on Aging and Department of Veterans Affairs (IK2CX002180) (F.M.E.); the Chan Zuckerberg Initiative (F.M.E.); the Rainwater Charitable Foundation (F.M.E.); and the National Institute on Aging U54 AG076040 (H.P.). The content of this publication is solely the responsibility of the authors and does not necessarily represent the official views of the National Institutes of Health. The funders had no role in study design, data collection and analysis, decision to publish or preparation of the manuscript.

Competing interests

C.K., R.M. and B.N.V. are founders and shareholders of KVM Therapeutics. C.K., R.M. and B.N.V. are inventors on patent applications related to FN1-targeted therapeutic approaches. C.K. is also a founder, shareholder and scientific advisor of Neuron-D GmbH. These entities had no role in the design, conduct, analysis, interpretation or reporting of this study. The other authors declare no competing interests.

Additional information

Extended data is available for this paper at https://doi.org/10.1038/s43587-026-01204-0.

Supplementary information The online version contains supplementary material available at https://doi.org/10.1038/s43587-026-01204-0.

Correspondence and requests for materials should be addressed to Caghan Kizil.

Peer review information *Nature Aging* thanks Caroline Menard, Andrew Mendiola, Natasha M. O'Brown, Michael Vanlandewijck and the other, anonymous, reviewer(s) for their contribution to the peer review of this work. Peer reviewer reports are available.

Prabesh Bhattarai[1,2,26], Elanur Yilmaz[1,2,26], Elif Öykü Cakir[1,2], Huseyin Tayran[1,2], Imdadul Haq[1,3], Dylan Murphy[4], Jonah Nadelmann Keller[5,6,7], Quentin Le Grand[8], Jacqueline O. Eschbach[1,3], Hilal Celikkaya[9], Mehmet I. Cosacak[9], Hande Yüceer Korkmaz[2,10], Annie J. Lee[1,2,11], Verena Haage[12], Yiyi Ma[1,12], Xue Wang[13], Nastasia Nelson[1,2], Weilin Lin[14,15], Yixin Zhang[14], Bengisu Turgutalp[2], Sherida M. de Leeuw[2,16], Ronak Patel[2], Dörthe Jülich[17], Özkan İş[18], Scott A. Holley[17], Philip L. De Jager[1,2,12], Uwe Freudenberg[19], Carsten Werner[19], Peter St George-Hyslop[1,2], Nilüfer Ertekin-Taner[18,20], Stéphanie Debette[8,21,22,23], Fanny M. Elahi[5,6], Elizabeth S. Fisher[4], Hemali Phatnani[1,3], Andrew F. Teich[1,2,16], Kate Tubbesing[4], Taylor Bertucci[4], Sally Temple[4], Tal Nuriel[2,16], Badri N. Vardarajan[1,2,3,11], Richard Mayeux[1,2,3,11,24,25] & Caghan Kizil[1,2,3,11]

[1]Department of Neurology, Columbia University Irving Medical Center, New York, NY, USA. [2]Taub Institute for Research on Alzheimer's Disease and the Aging Brain, Columbia University Irving Medical Center, New York, NY, USA. [3]New York Genome Center, New York, NY, USA. [4]Neural Stem Cell Institute, Albany, NY, USA. [5]Department of Neurology, Icahn School of Medicine at Mount Sinai, New York, NY, USA. [6]Department of Neuroscience, Icahn School of Medicine at Mount Sinai, New York, NY, USA. [7]Perelman School of Medicine, University of Pennsylvania, Philadelphia, PA, USA. [8]Bordeaux Population Health Research Center, University of Bordeaux, Inserm, UMR 1219, Bordeaux, France. [9]German Center for Neurodegenerative Diseases (DZNE), Dresden, Germany. [10]Department of Neuroscience, Aziz Sancar Institute of Experimental Medicine, Istanbul University, Istanbul, Turkey. [11]Gertrude H. Sergievsky Center, College of Physicians and Surgeons, Columbia University, New York, NY, USA. [12]Center for Translational and Computational Neuroimmunology, Department of Neurology, Columbia University Irving Medical Center, New York, NY, USA. [13]Department of Quantitative Health Sciences, Mayo Clinic Florida, Jacksonville, FL, USA. [14]B CUBE Center for Molecular Bioengineering, Technische Universität Dresden, Dresden, Germany. [15]National Key Laboratory of Immunity and Inflammation, Suzhou Institute of Systems Medicine, Chinese Academy of Medical Sciences and Peking Union Medical College, Suzhou, China. [16]Department of Pathology and Cell Biology, Columbia University Irving Medical Center, New York, NY, USA. [17]Department of Molecular, Cellular, and Developmental Biology, Yale University, New Haven, CT, USA. [18]Department of Neuroscience, Mayo Clinic Florida, Jacksonville, FL, USA. [19]Leibniz Institute of Polymer Research Dresden, Max Bergmann Center of Biomaterials Dresden, Dresden, Germany. [20]Department of Neurology, Mayo Clinic Florida, Jacksonville, FL, USA. [21]Institut du Cerveau (ICM), Paris Brain Institute, INSERM U1127, UMR CNRS 7225, Paris, France. [22]Department of Neurology, Bordeaux University Hospital, Bordeaux, France. [23]Assistance Publique des Hôpitaux de Paris, Sorbonne Université, Paris, France. [24]Department of Psychiatry, Columbia University Irving Medical Center, New York, NY, USA. [25]Department of Epidemiology, Mailman School of Public Health, Columbia University Irving Medical Center, New York, NY, USA. [26]These authors contributed equally: Prabesh Bhattarai, Elanur Yilmaz.
✉e-mail: ck2893@cumc.columbia.edu

https://doi.org/10.1038/s43587-026-01204-0

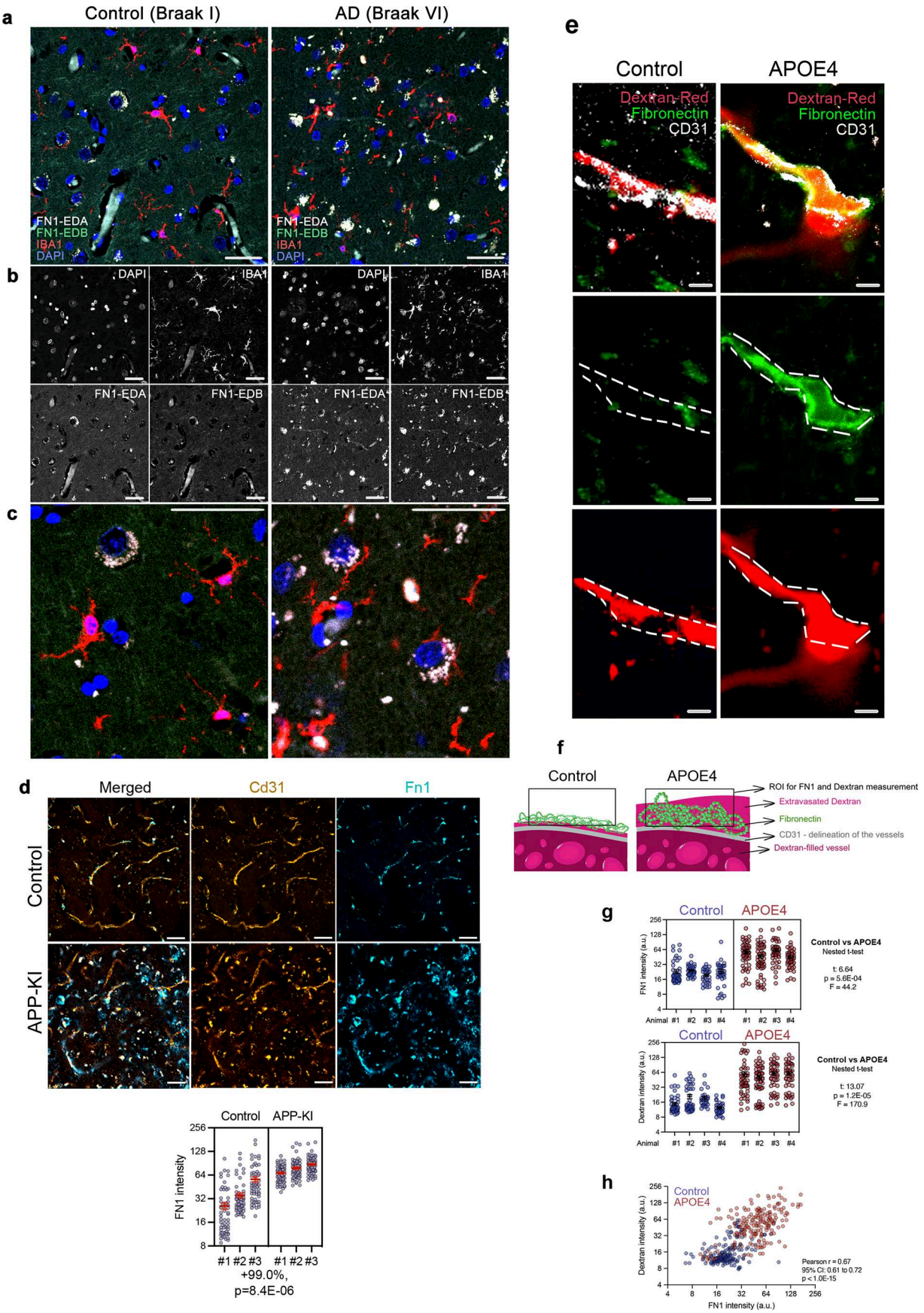

Extended Data Fig. 1 | See next page for caption.

https://doi.org/10.1038/s43587-026-01204-0

Extended Data Fig. 1 | Increased expression of fibronectin splice variants FN1-EDA and FN1-EDB in Alzheimer's disease brains; and FN1-deposited vessels show leakage in *APOE4* mice. a, Representative confocal images of cortical sections from control (Braak I) and AD (Braak VI) brains stained for FN1-EDA, FN1-EDB, IBA1 (microglia), and DAPI (nuclei). AD tissue shows elevated FN1-EDA and FN1-EDB immunoreactivity and diffuse deposition compared to control. Representative images are from independent experiments that were repeated three times with similar results. **b**, Corresponding single-channel grayscale images from the same fields shown in A. FN1-EDA and FN1-EDB are both minimally expressed in control tissue but are markedly upregulated in AD, particularly around vessels and glial structures. **c**, High-magnification views showing close spatial association of FN1 splice variants with IBA1-positive microglia in AD cortex. FN1-EDA and FN1-EDB signals appear localized around or within activated microglia in AD, suggesting microglial association or uptake. Scale bars: 25 µm. **d**, Assessment of FN1 expression in control and APP knock-in mouse model. Merged double immunofluorescence staining (left) and individual staining for CD31 (middle) and FN1 (right) are shown. The graphs quantify the fluorescence intensity for FN1 and CD31, providing statistical analysis with n representing the number of observations, as well as percent changes and p-values. Each data point represents one mouse. Measurements were obtained from n = 3 independent mice per group. Multiple vessels were analyzed per mouse, and statistical inference was performed at the animal level using generalized estimating equations (GEE, two-sided). Data are presented as mean ± s.e.m. Scale bars equal 100 µm. Quantitative data in the graphs are represented as dot plots, and statistical significance is noted as non-significant (ns) or with the precise p-value where applicable. * ($p < 0.0332$), ** ($p < 0.0021$), *** ($p < 0.002$), and **** ($p < 0.0001$). **e**, Representative confocal images show fibronectin, Dextran, CD31 in control (left) and APOE4/4 (right) mice at 20 months of age. Scale bars: 5 µm. **f**, Schematic illustrating the quantification strategy. CD31 staining was used to delineate vessel boundaries, and perivascular regions of interest (ROIs) were defined to quantify fibronectin deposition and extravascular Dextran intensity outside the vessel lumen. **g**, Quantification of fibronectin intensity (top) and extravascular Dextran intensity (bottom) in control and *APOE4* mice. Each data point represents a vessel. Statistical inference was performed at the level of the individual animals using Nested t-test, two sided. Data are presented as mean ± s.e.m. Statistical comparisons were performed with animals as the unit of inference. *APOE4* mice show significantly increased fibronectin deposition and Dextran leakage compared to controls. **h**, Correlation analysis between fibronectin intensity and extravascular Dextran intensity across quantified vessels, demonstrating a strong positive association between fibronectin deposition and BBB leakage. Data are presented as mean ± s.e.m (Pearson correlation).

https://doi.org/10.1038/s43587-026-01204-0

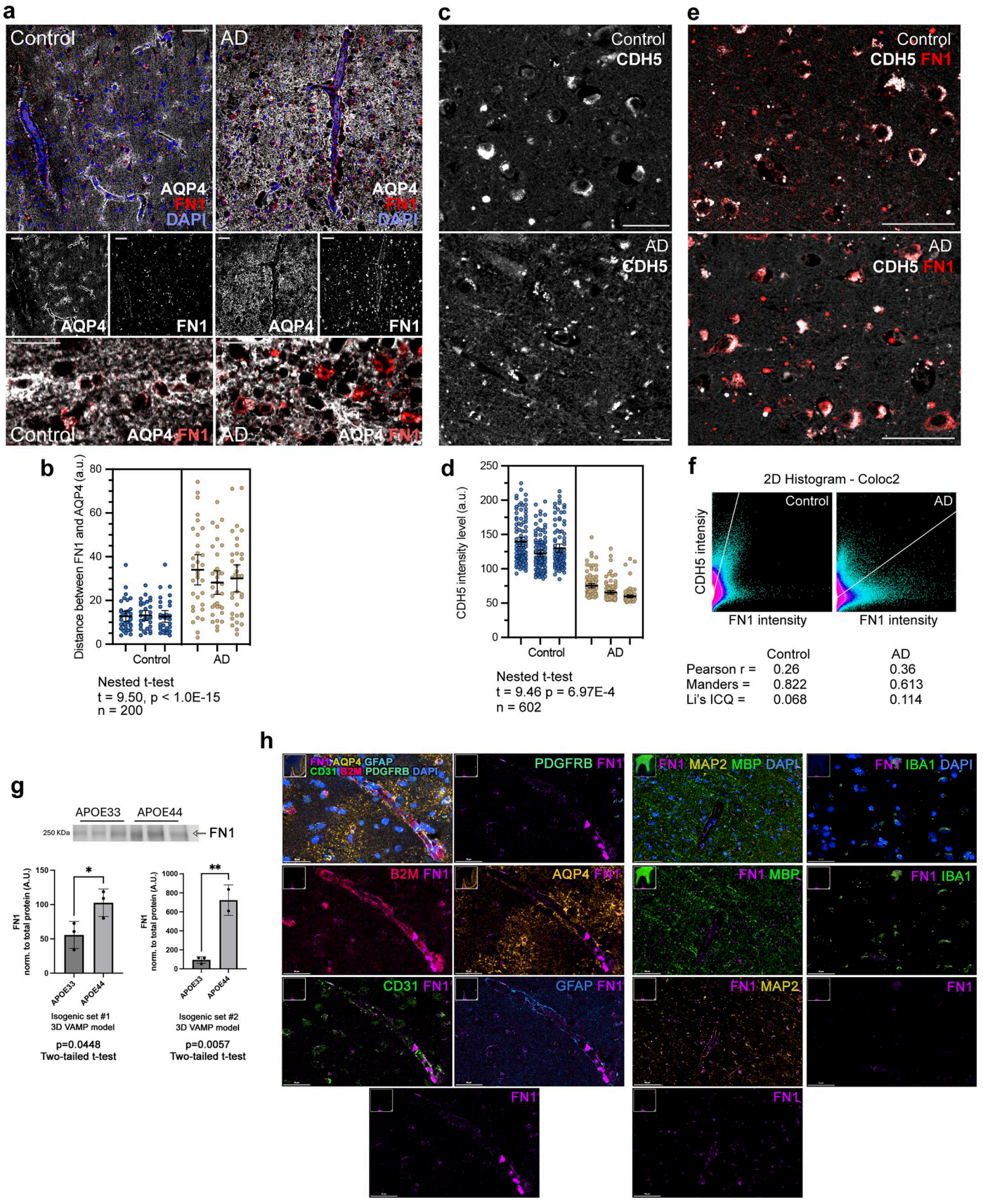

Extended Data Fig. 2 | See next page for caption.

https://doi.org/10.1038/s43587-026-01204-0

Extended Data Fig. 2 | Changes in glial polarity and altered fibronectin (FN1) localization in AD. a, Representative images of cortex from control and Alzheimer's disease (AD) cases stained for aquaporin-4 (AQP4), fibronectin (FN1), and nuclei (DAPI). **b**, Quantification of FN1-AQP4 spatial proximity. Measurements were obtained from n = 3 independent human donors per group. Multiple ROIs were analyzed per donor, and statistical inference was performed at the donor level using generalized estimating equations (GEE, two-sided). **c**, Representative images of CDH5 (VE-cadherin) immunostaining in cortical tissue from control and AD cases. **d**, Quantification of CDH5 intensity. Measurements were obtained from n = 3 independent human donors per group. Multiple ROIs were analyzed per donor, and statistical inference was performed at the donor level using generalized estimating equations (GEE, two-sided). Data are presented as mean ± s.e.m. **e**, Dual-channel images of CDH5 and FN1 and their colocalization. Data are presented as mean ± s.e.m. **f**, 2D histograms of CDH5 and FN1 signal intensities (Coloc 2 analysis. Scale bars: 50 µm. **g**, Western blot quantification for FN1 expression in 3D VAMP models with isogenic iPSC-derived cell lines. Western blot analyses showing FN1 protein levels in 3D VAMP cultures derived two isogenic lines. Increased FN1 levels are observed in APOE4/4 (2E3, 4B4) models compared to their corresponding APOE3/3 controls (MC2C, RC2C) in both isogenic lines. Each data point represents one independent 3D VAMP culture. Statistical analyses were performed using biological replicates. Data are presented as mean ± s.e.m. **h**, FN1 protein localization in brain cell types with multiplex immunostaining. Representative images from multiplex immunostaining for FN1, GFAP (astrocyte). AQP4 (astrocyte endfeet), CD31 (endothelia), B2M (endothelia), MBP (oligodendrocyte), IBA1 (microglia), PDGFR (pericyte), MAP2 (neuron). Scale bars: 100 µm for MBP and MAP2; 50 µm elsewhere. Representative images are from two independent runs with similar results.

https://doi.org/10.1038/s43587-026-01204-0

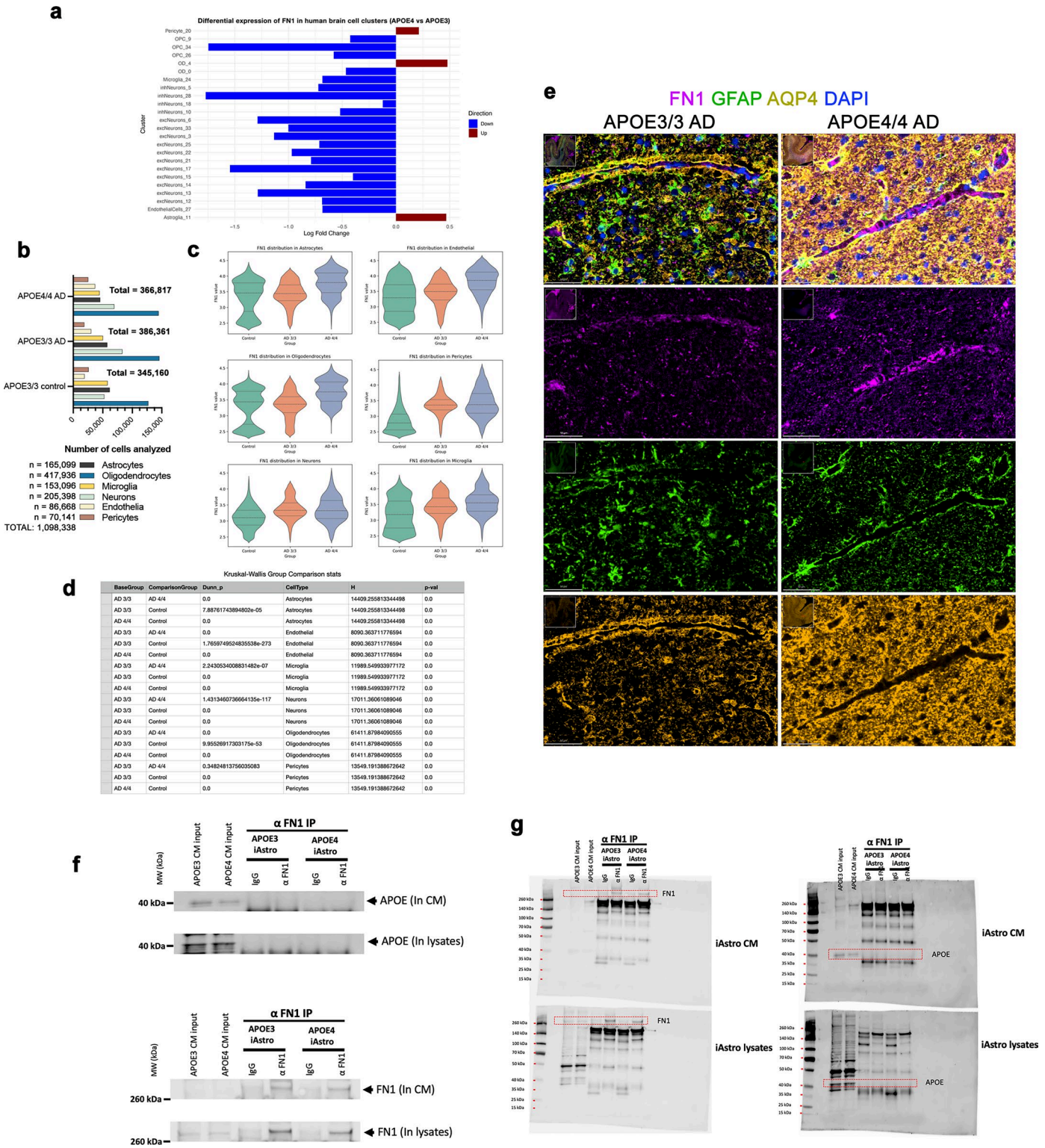

BaseGroup	ComparisonGroup	Dunn_p	CellType	H	p-val
AD 3/3	AD 4/4	0.0	Astrocytes	14409.255813344498	0.0
AD 3/3	Control	7.88761743894802e-05	Astrocytes	14409.255813344498	0.0
AD 4/4	Control	0.0	Astrocytes	14409.255813344498	0.0
AD 3/3	AD 4/4	0.0	Endothelial	8090.363711776594	0.0
AD 3/3	Control	1.7659749524835538e-273	Endothelial	8090.363711776594	0.0
AD 4/4	Control	0.0	Endothelial	8090.363711776594	0.0
AD 3/3	AD 4/4	2.2430534008831482e-07	Microglia	11989.549933977172	0.0
AD 3/3	Control	0.0	Microglia	11989.549933977172	0.0
AD 4/4	Control	0.0	Microglia	11989.549933977172	0.0
AD 3/3	AD 4/4	1.4313460736664135e-117	Neurons	17011.36061089046	0.0
AD 3/3	Control	0.0	Neurons	17011.36061089046	0.0
AD 4/4	Control	0.0	Neurons	17011.36061089046	0.0
AD 3/3	AD 4/4	0.0	Oligodendrocytes	61411.87984090555	0.0
AD 3/3	Control	9.955269173031 75e-53	Oligodendrocytes	61411.87984090555	0.0
AD 4/4	Control	0.0	Oligodendrocytes	61411.87984090555	0.0
AD 3/3	AD 4/4	0.34824813756035083	Pericytes	13549.191388672642	0.0
AD 3/3	Control	0.0	Pericytes	13549.191388672642	0.0
AD 4/4	Control	0.0	Pericytes	13549.191388672642	0.0

Extended Data Fig. 3 | Differential expression of FN1 in human brain with APOE4. a, Graph indicates differential expression of *FN1* gene in human brain snRNA-seq dataset comparing *APOE4* carriers to *APOE3* individuals (from ref.28, cell cluster IDs retained as in the original publication). APOE4-dependent *FN1* upregulation is most pronounced in astrocytes. **b**, Cell numbers analyzed in multiplex immunostaining. **c**, Distribution of FN1 expression in cell types based on *APOE* genotype and AD status. **d**, Kruskal-Wallis test statistics between groups in every cell type comparison. **e**, Multiplex immunostain for FN1, AQP4, GFAP and DAPI counterstain in *APOE3/3* and *APOE4/4* AD patient brains. Representative images are from two independent runs with similar results. Scale bars 50 µm. **f**, Upper blot: representative immunoblots showing the presence of APOE in conditioned media (CM) and cell lysate input lanes, but no detectable APOE bands in FN1 pulldown lanes. Lower blot: representative immunoblot confirming successful FN1 pulldown on agarose beads using the FN1 antibody. **g**, Full blot membrane images. Representative immunoblots are from three independent experiments with similar results.

https://doi.org/10.1038/s43587-026-01204-0

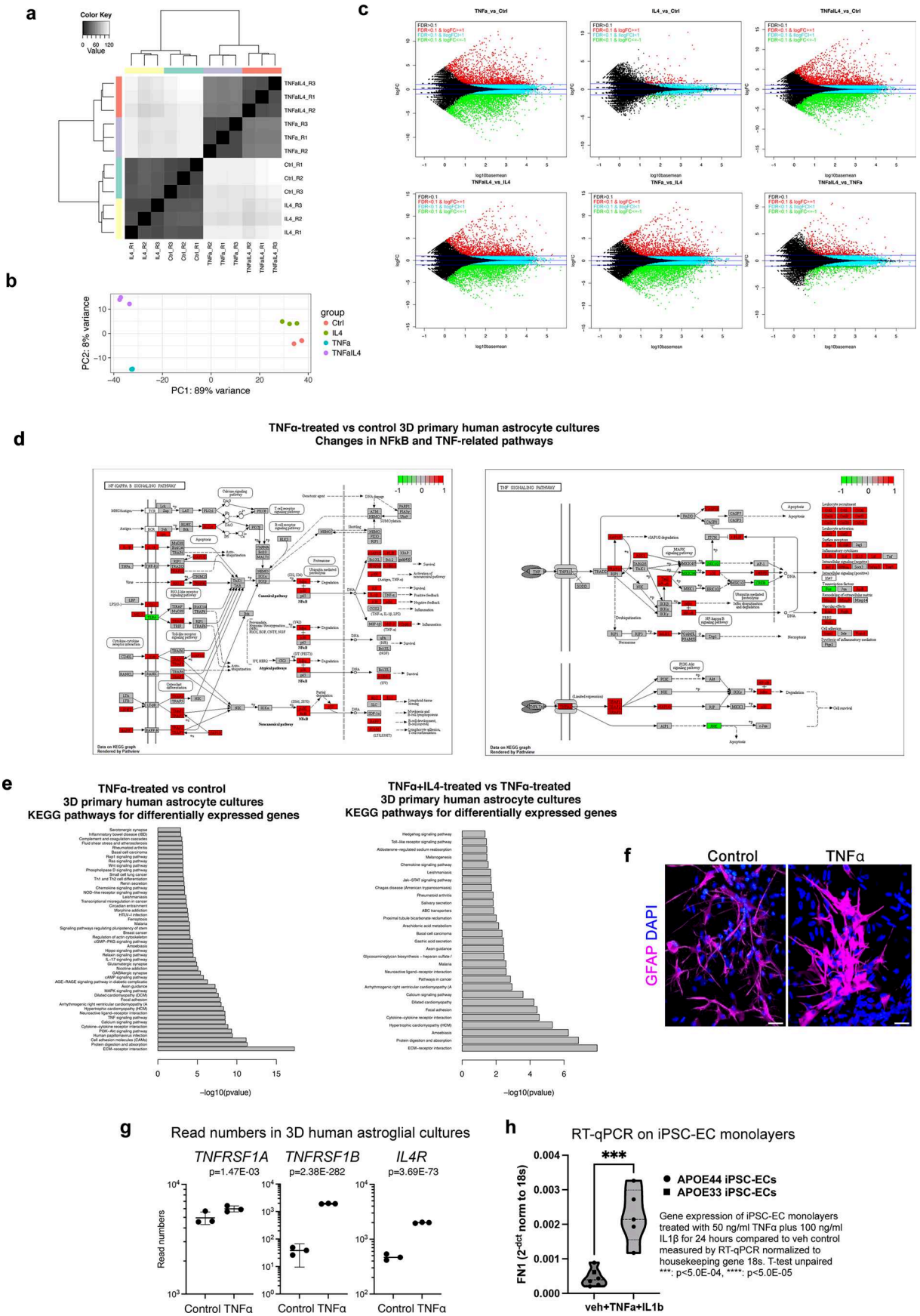

Extended Data Fig. 4 | See next page for caption.

https://doi.org/10.1038/s43587-026-01204-0

Extended Data Fig. 4 | Bulk RNA sequencing in 3D hydrogel cultures, TNFα treatment response, and TNFα and IL4 receptor expression in 3D pHA cultures. a, Sample correlation graph for control, IL4-treated, TNFα-treated, and TNFα + IL4-treated replicates. **b**, Principal component analyses of groups. **c**, MA plots for comparison between samples. Red, overexpression above significance threshold, green, downregulated above significance threshold. **d**, KEGG pathway schematics indicating changes NFkB and TNFα signaling components after TNFα treatment in 3D primary human astrocytes (pHA) cultures. Red: upregulated, green: downregulated. **e**, KEGG pathway chart for differentially expressed genes in TNFα-treated versus control 3D pHA cultures and TNFα + IL4-treated versus TNFα-treated 3D pHA cultures. Gene Set Enrichment Analysis (GSEA), with statistical significance determined by phenotype-label permutation and FDR correction. **f**, Immunostaining for GFAP with DAPI counterstain in control and TNFα-treated 3D pHA cultures. Scale bars equal 25 µm. Representative images are from three independent experiments with similar results. **g**, RNA sequencing read counts of TNFRSF1A, TNFRSF1B, and IL4R in 3D primary human astrocyte (pHA) cultures under control and TNFα-treated conditions. Each data point represents one independent 3D pHA culture (n = 3 independent biological replicates per condition). Statistical analyses were performed using biological replicates and with unpaired two-tailed t-test. Data are presented as mean ± s.d. **h**, RT-qPCR analysis of FN1 expression in human iPSC-derived endothelial cell (iPSC-EC) monolayers treated with vehicle or TNFα (50 ng/ml) plus IL1β (100 ng/ml) for 24 h. Gene expression was normalized to 18S. Each data point represents one independent biological replicate (n = 4 (APOE33) and n = 7 (APOE44) independent cultures). Violin plots show the data distribution; the center line indicates the median, the box indicates the interquartile range, whiskers extend to the minimum and maximum values, and points represent individual biological replicates. Statistical significance was determined using an unpaired two-sided Student's t-test. p = 0.0005.

https://doi.org/10.1038/s43587-026-01204-0

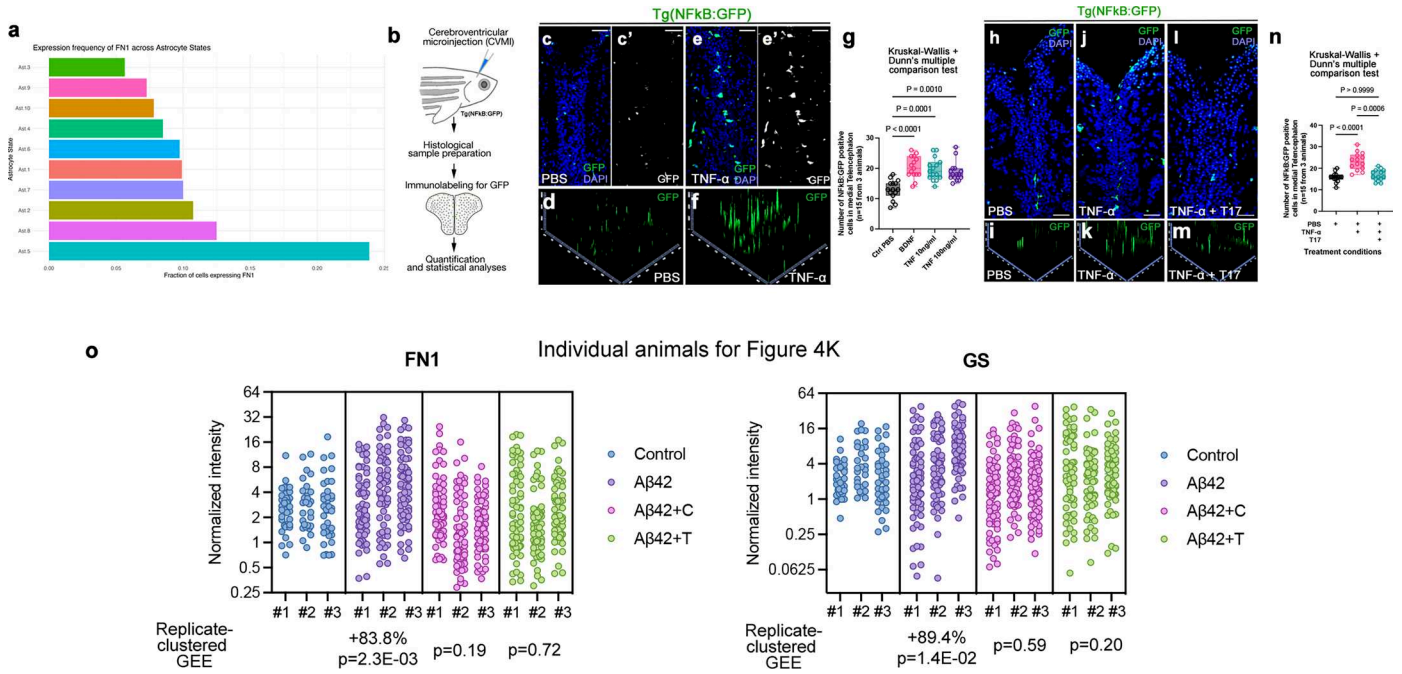

Extended Data Fig. 5 | TNFα activates NFkB signaling in zebrafish brain. **a**, Bar plot showing the fraction of cells expressing *FN1* across astrocyte states identified in the Hispanic multiome dataset[28] following label transfer from ROSMAP data[38]. Astrocyte state 5 (Ast.5), corresponding to the reactive astrocyte cluster, exhibits the highest FN1 expression frequency. **b**, In vivo experimental scheme. Adult transgenic reporter zebrafish that express GFP under the NFkB promoter were injected. Histological sections were prepared at 1 day after the injection. Immunostaining for GFP is followed by quantification and statistical analyses of GFP-positive cells in the medial telencephalic region. **c-f**, GFP and DAPI staining on brain sections of NFkB:GFP reporter transgenic animals injected with PBS (**c, d**) and TNFα (**e, f**). **c'**, Individual GFP fluorescence channel of c. **e'**, Individual GFP fluorescence channel of e. **d, f**, Topological fluorescence histograms for NFkB activity in the brain sections of the animals injected with PBS (**d**) and TNFα (**f**). **g**, Quantification of the average number of NFκB-positive cells per telencephalic section under the treatment conditions shown in b-e. Five brain sections were analyzed from each animal (n = 3 independent animals per condition; 15 sections total). Each data point represents one brain section. Statistical inference was performed at the animal level with Kruskal-Wallis, Dunn's multiple comparison test. Data are presented as mean ± s.e.m. **h-l**, GFP and DAPI staining on brain sections of NFkB:GFP reporter transgenic animals injected with PBS (**h**), TNFα (**i**), and TNFα + T17 (TNFα blocker, ref.142) **i, k, m**, Topological fluorescence histogram for NFkB activity in **g** (**i**), **j** (**k**), and **m** (**l**). **n**, Quantification of the average number of NFκB-positive cells per telencephalic section under the treatment conditions shown in **g-k**. Five brain sections were analyzed from each animal (n = 3 independent animals per condition; 15 sections total). Each data point represents one brain section. Statistical inference was performed at the animal level with Kruskal-Wallis, Dunn's multiple comparison test. Data are presented as mean ± s.e.m. Statistical analyses for multiple comparisons were performed with Dunn's multiple comparison test after Kruskal-Wallis test. p values are shown. Scale bars equal 50 µm. **o**, Individual animal representation of data in Fig. 4k. Each data point in graphs are individual measurements that are nested within replicate cluster, which are the unit of inference using GEE with robust SEs (two-sided).

https://doi.org/10.1038/s43587-026-01204-0

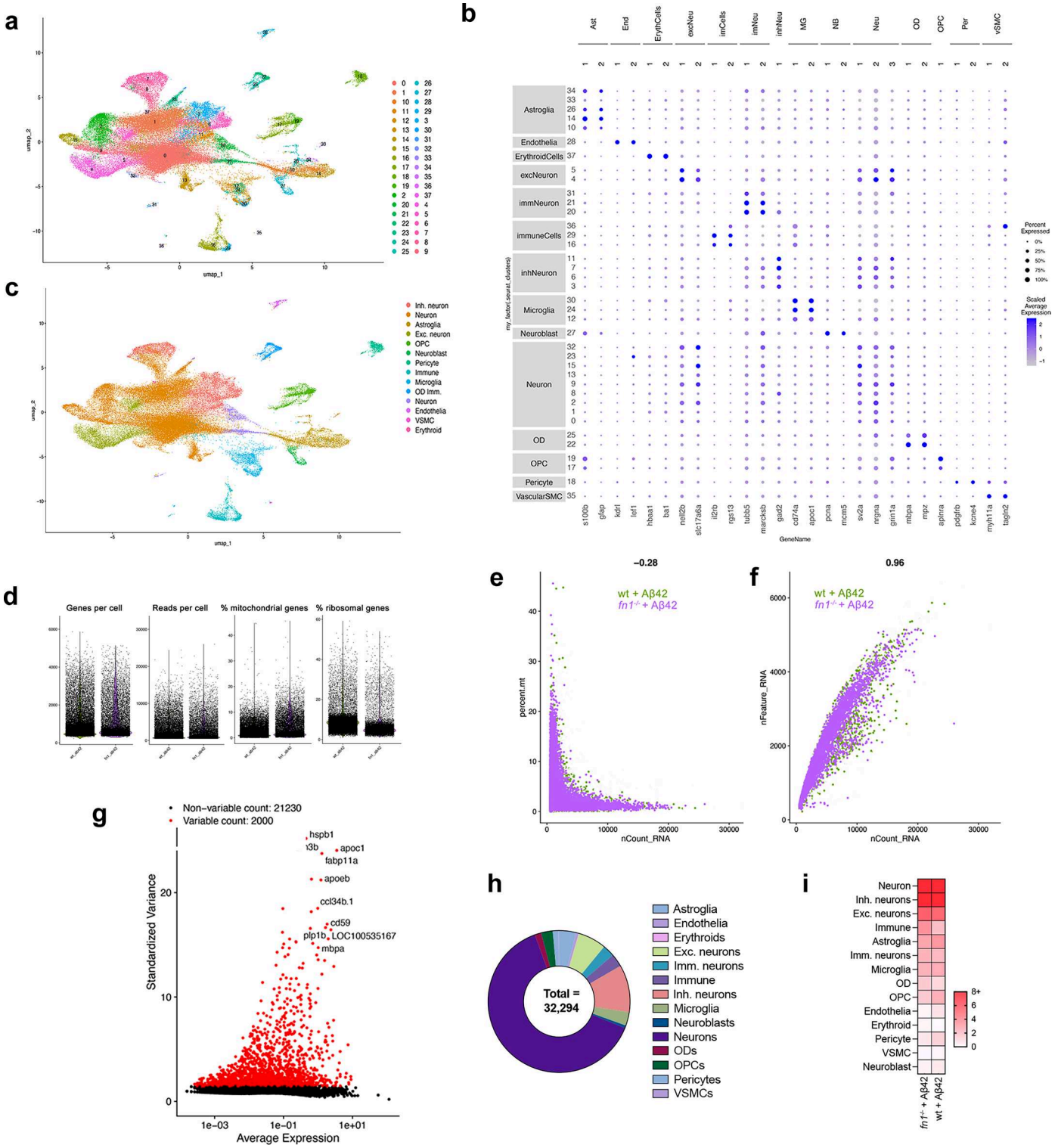

Extended Data Fig. 6 | Single cell transcriptomics in fn1b homozygous knockout animals after Aβ42. a, UMAP for 38 clusters. **b**, Dot plot for cell type markers. **c**, UMAP with cell types color-coded. **d**, Violin plots for genes per cell, reads per cell, percent mitochondrial gene expression and percent ribosomal gene expression. **e**, Distribution graphs for percent mitochondrial gene expression against reads per cell in wt + Aβ42 and *fn1b*$^{-/-}$ + Aβ42 samples. **f**, Distribution graphs for number of sequenced genes per cell against reads per cell in wt + Aβ42 and *fn1b*$^{-/-}$ + Aβ42 samples. **g**, Distribution plot for most variable gene expressions. **h**, Total number of cells sequenced and their pie chart distribution to cell types. **i**, Heat map of comparing percentages of sequenced cell types in wt + Aβ42 and *fn1b*$^{-/-}$ + Aβ42 samples.

https://doi.org/10.1038/s43587-026-01204-0

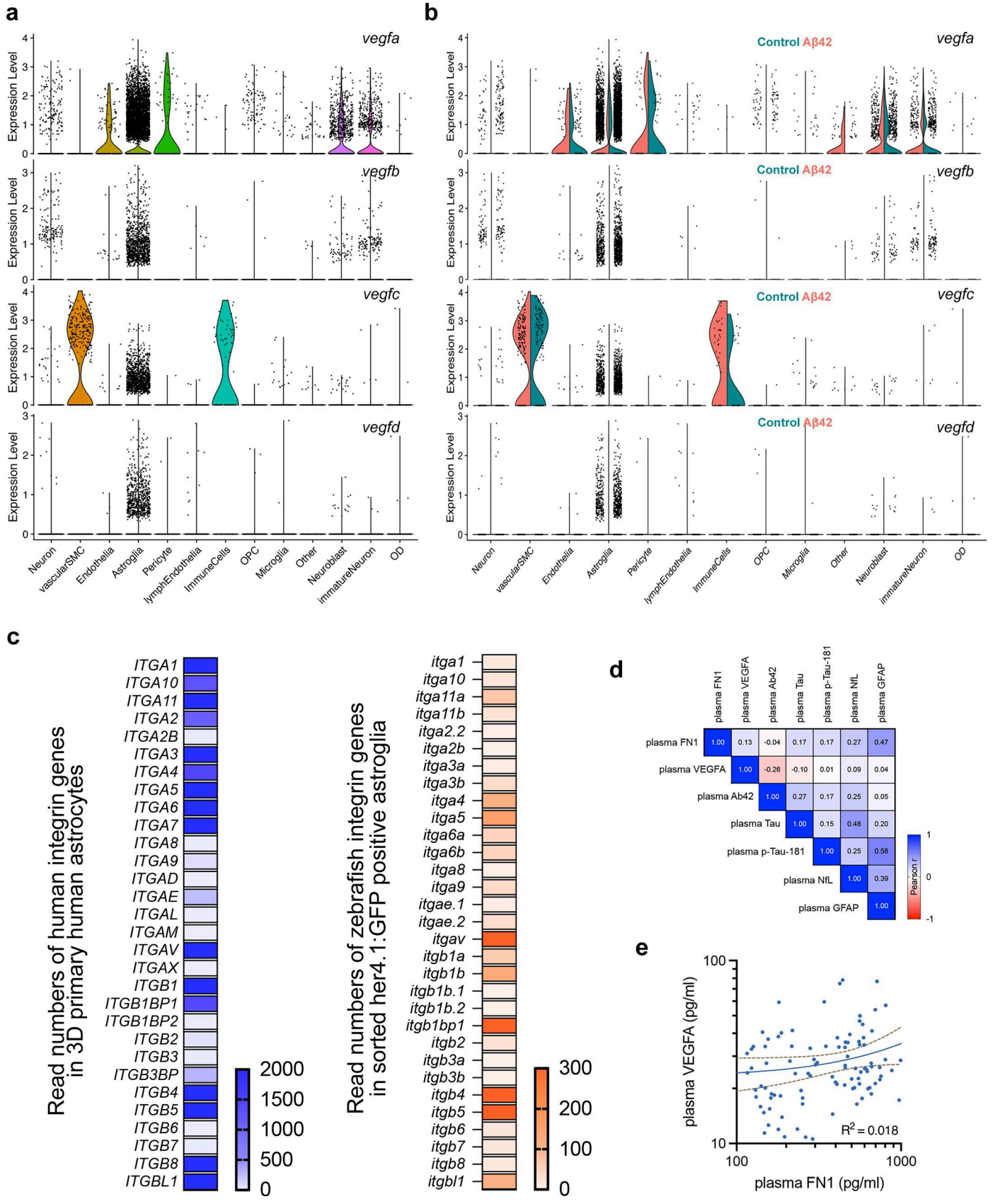

Extended Data Fig. 7 | See next page for caption.

https://doi.org/10.1038/s43587-026-01204-0

Extended Data Fig. 7 | Expression of VEGF ligands, expression of integrin receptors in 3D pHA cultures and adult zebrafish brain astrocytes, and relationship of plasma FN1 levels with VEGFA. a, Violin plots for expression of *vegfa, vegfb, vegfc*, and *vegfd* in zebrafish brain. **b**, Split violin plots for expression of *vegfa, vegfb, vegfc*, and *vegfd* comparing control and Aβ42 treatment conditions. Data from refs. 12,43,45,112. **c**, Heat maps for bulk RNA sequencing reads in 3D pHA and her4:GFP-positive sorted astrocytes from zebrafish brain. Data from refs. 37,43,45. **d**, Pearson correlation matrix depicting relationships between plasma FN1 levels and plasma biomarkers associated with AD, including VEGFA, Ab42, Tau, p-Tau-181, NfL, and GFAP. Pearson correlation coefficients (r) are color-coded from -1 (red) to 1 (blue), with values provided in each cell. Plasma FN1 shows no correlation with VEGFA (r = 0.13). **e**, Scatter plot showing the relationship between plasma FN1 and VEGFA concentrations. No significant correlation is observed (R^2; = 0.018). Both axes are log-scaled, and a non-linear fit with confidence intervals is shown.

https://doi.org/10.1038/s43587-026-01204-0

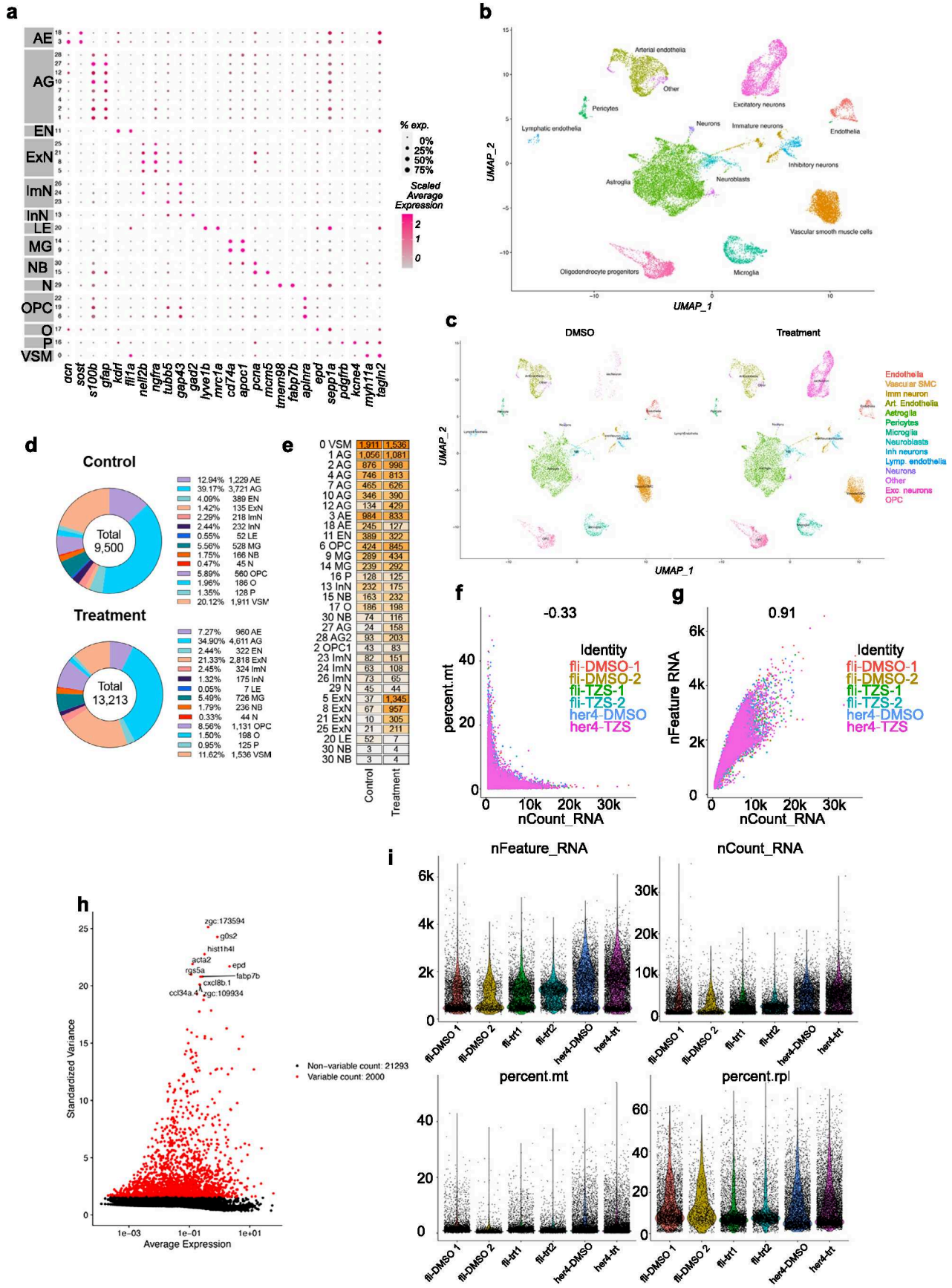

Extended Data Fig. 8 | See next page for caption.

https://doi.org/10.1038/s43587-026-01204-0

Extended Data Fig. 8 | Single cell transcriptomics in VEGFRi zebrafish brains. **a**, Dot plot for cell type markers. **b**, UMAP for cell types in color-codes. **c**, UMAP for cell types in control (left) and VEGFRi (right) samples. **d**, Total number of cells sequenced per experimental group as pie charts, and their cell type percentages. **e**, Heat map comparing sequenced cell numbers in clusters (control and treatment - VEGFRi). **f**, Distribution graphs for percent mitochondrial gene expression against reads per cell in control and VEGFRi samples. **g**, Distribution graphs for number of sequenced genes per cell against reads per cell in control and VEGFRi samples. **h**, Distribution plot for most variable gene expressions. **i**, Violin plots for sequenced genes per cell, reads per cell, percent mitochondrial gene expression and percent ribosomal gene expression. Vehicle-treated and VEGFRi fli1a:EGFP-sorted cells had two replicates, vehicle-treated and VEGFRi her4:RFP-sorted cells has one replicate.

https://doi.org/10.1038/s43587-026-01204-0

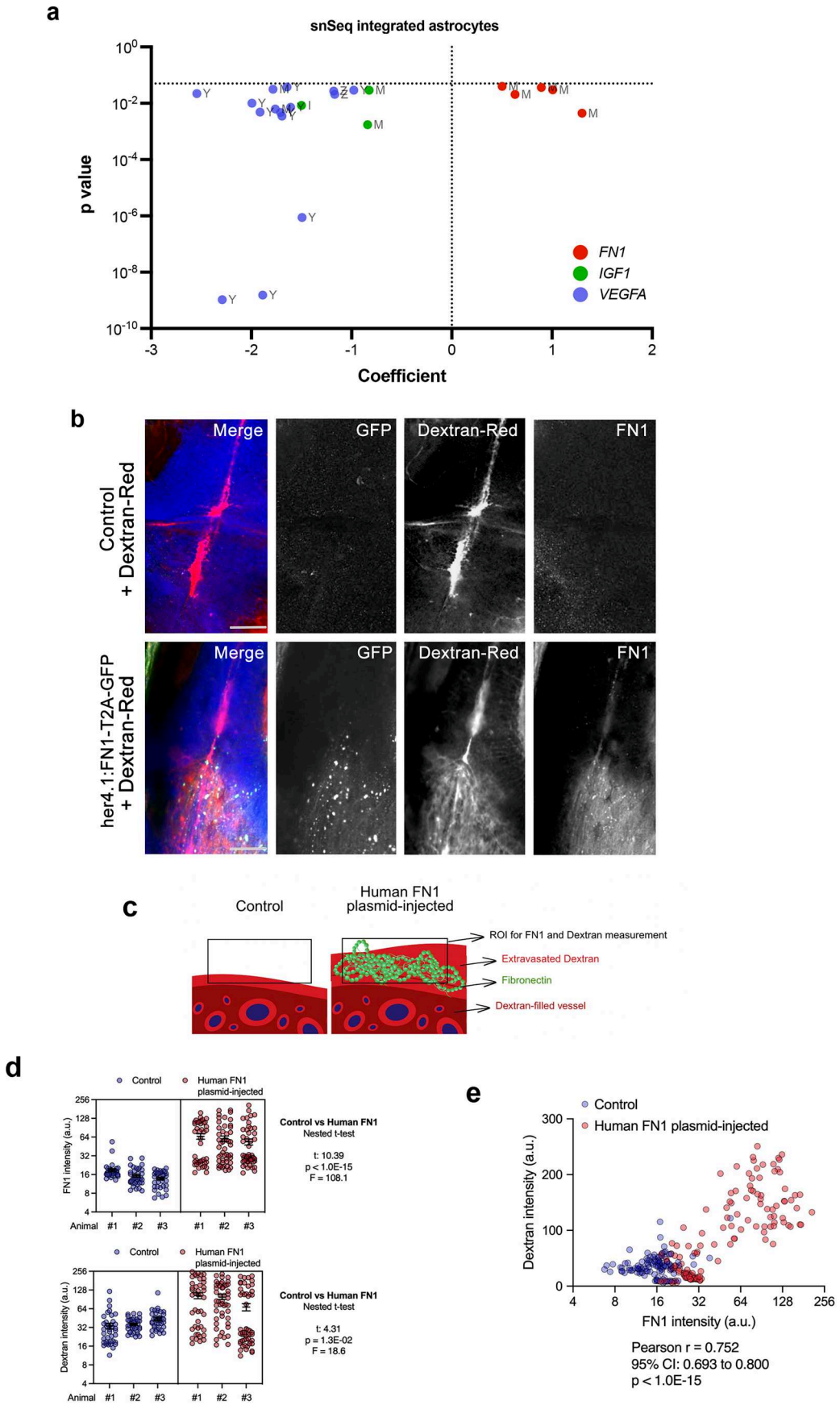

Extended Data Fig. 9 | See next page for caption.

https://doi.org/10.1038/s43587-026-01204-0

Extended Data Fig. 9 | Expression of FN1, VEGFA, IGF1 in integrated human single nucleus dataset, and astroglial FN1 causes vascular leakage in zebrafish. **a**, Graph indicating astrocyte clusters in human single nucleus datasets that upregulate *FN1* and downregulate *IGF1* and *VEGFA*. Data derived from integration of single nucleus datasets in refs. 2,24,40,53 by ref. I: ref. 40 Y: ref. 2., Z: ref. 24, M: ref. 53. Statistics: MAST hurdle model, with regression coefficients (β) estimated for the effect of interest and statistical significance evaluated using Wald tests. **b**, Representative confocal images of control and her4.1:FN1-T2A-GFP zebrafish larvae after injection with 3 kDa Dextran-Red at 3 dpf and fixation 15 min after injection. Merged and single-channel images show GFP, Dextran-Red, and FN1. Control larvae show Dextran-Red largely confined to the vasculature, whereas her4.1:FN1-T2A-GFP larvae show astroglial GFP expression, increased FN1 signal, and increased extravascular Dextran-Red signal. Scale bars, 100 µm. **c**, Schematic showing the region-of-interest strategy used to quantify FN1 deposition and extravascular Dextran-Red intensity. **d**, Quantification of FN1 intensity and extravascular Dextran-Red intensity in control and her4.1:FN1-T2A-GFP larvae. Each data point represents one quantified ROI. Measurements were obtained from n = 3 independent animals per group. Multiple ROIs were analyzed per animal, and statistical inference was performed at the animal level using a two-tailed nested t-test to account for repeated measurements from the same animal. **e**, Correlation between FN1 intensity and Dextran-Red intensity across quantified ROIs. Pearson correlation coefficient, 95% confidence interval, and exact P value are indicated on the graph (Pearson correlation). Data are presented as mean ± s.e.m.

https://doi.org/10.1038/s43587-026-01204-0

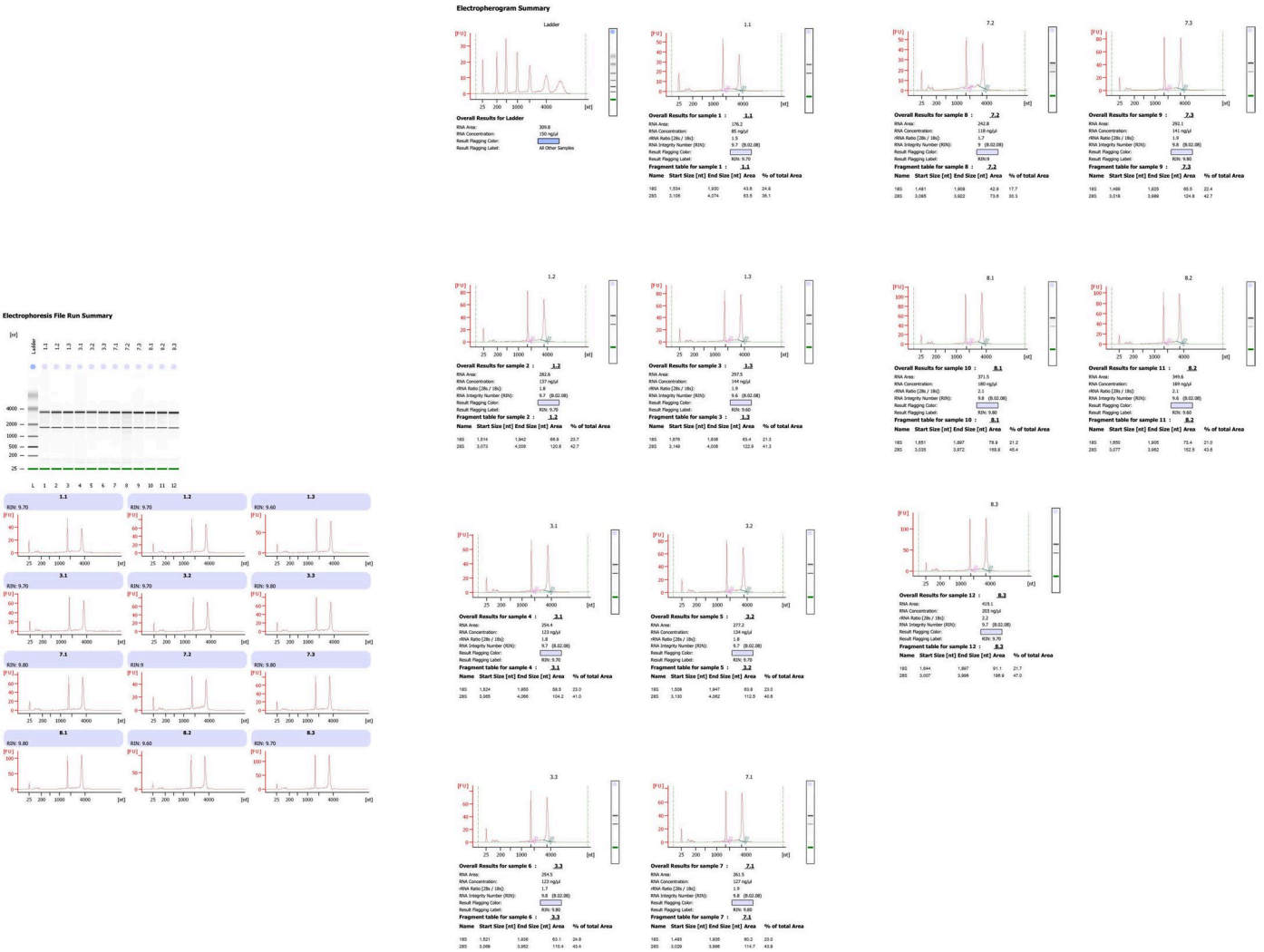

Extended Data Fig. 10 | RNA quality in bulk RNA sequencing of 3D pHA cultures. Flow cytometry gating parameters, electrophoresis file run summary, and RNA integrity measures by electropherogram summaries and RIN values.

nature portfolio

Corresponding author(s): Caghan Kizil

Last updated by author(s): Sep 1, 2026

Reporting Summary

Nature Portfolio wishes to improve the reproducibility of the work that we publish. This form provides structure for consistency and transparency in reporting. For further information on Nature Portfolio policies, see our Editorial Policies and the Editorial Policy Checklist.

Statistics

For all statistical analyses, confirm that the following items are present in the figure legend, table legend, main text, or Methods section.

n/a	Confirmed	
☐	☒	The exact sample size (*n*) for each experimental group/condition, given as a discrete number and unit of measurement
☐	☒	A statement on whether measurements were taken from distinct samples or whether the same sample was measured repeatedly
☐	☒	The statistical test(s) used AND whether they are one- or two-sided *Only common tests should be described solely by name; describe more complex techniques in the Methods section.*
☐	☒	A description of all covariates tested
☐	☒	A description of any assumptions or corrections, such as tests of normality and adjustment for multiple comparisons
☐	☒	A full description of the statistical parameters including central tendency (e.g. means) or other basic estimates (e.g. regression coefficient) AND variation (e.g. standard deviation) or associated estimates of uncertainty (e.g. confidence intervals)
☐	☒	For null hypothesis testing, the test statistic (e.g. *F*, *t*, *r*) with confidence intervals, effect sizes, degrees of freedom and *P* value noted *Give P values as exact values whenever suitable.*
☒	☐	For Bayesian analysis, information on the choice of priors and Markov chain Monte Carlo settings
☐	☒	For hierarchical and complex designs, identification of the appropriate level for tests and full reporting of outcomes
☐	☒	Estimates of effect sizes (e.g. Cohen's *d*, Pearson's *r*), indicating how they were calculated

Our web collection on statistics for biologists contains articles on many of the points above.

Software and code

Policy information about availability of computer code

Data collection

Raw single-cell RNA sequencing data were processed using the Cell Ranger Single Cell Software Suite (10x Genomics, v6.1.2) with default parameters, and reads were aligned to the zebrafish reference genome GRCz11 (Ensembl release 105). Cell clustering, marker gene identification, differential expression analysis, and feature plot generation were performed using Seurat (v5). For quantitative RT–PCR, cycle threshold (Ct) values were obtained using a QuantStudio™ 3 Real-Time PCR System (Thermo Fisher Scientific). Genome-wide DNA methylation profiles were generated using the Infinium MethylationEPIC BeadChip (Illumina) at the New York Brain Bank. Confocal image acquisition and colocalization analyses were performed using the ZEN software colocalization module (blue edition, version 3.2; Carl Zeiss, Jena, Germany). Automated cell counting was conducted using a Countess II FL Automated Cell Counter (Thermo Fisher Scientific). RNA integrity and quality were assessed using an Agilent 2100 Bioanalyzer (Agilent Technologies).

Data analysis	Imaging data were acquired using Zeiss AxioImager Z1, Zeiss LSM780, and Zeiss LSM800 confocal microscopes. Colocalization of immunohistochemical markers was quantified using the ZEN software colocalization module (Carl Zeiss, Germany). Multiplex immunofluorescence staining was performed using the COMET platform (Lunaphore Technologies), and image analysis was conducted using HORIZON Viewer (Lunaphore Technologies) and HALO software (Indica Labs). For bulk RNA sequencing analyses, quality-controlled reads were aligned to the human genome (GRCh38) using GSNAP, and differential expression analysis was performed with DESeq2. Single-cell RNA-seq datasets were processed using Seurat (v5). Cells with fewer than 200 expressed genes or genes expressed in fewer than three cells were excluded prior to downstream analyses. Following quality filtering, datasets were normalized, the top 2,000 variable genes were selected, and datasets were integrated using FindIntegrationAnchors, IntegrateData, IntegrateLayers, and JoinLayers functions. DoubletFinder was used to identify and remove doublets prior to downstream analyses. Cycle threshold (Ct) values for qRT–PCR experiments were obtained using a QuantStudio™ 3 Real-Time PCR System (Thermo Fisher Scientific). Statistical analyses were performed using GraphPad Prism (v9.2.0).

For manuscripts utilizing custom algorithms or software that are central to the research but not yet described in published literature, software must be made available to editors and reviewers. We strongly encourage code deposition in a community repository (e.g. GitHub). See the Nature Portfolio guidelines for submitting code & software for further information.

Data

Policy information about availability of data

All manuscripts must include a data availability statement. This statement should provide the following information, where applicable:

- Accession codes, unique identifiers, or web links for publicly available datasets
- A description of any restrictions on data availability
- For clinical datasets or third party data, please ensure that the statement adheres to our policy

All sequencing datasets generated in this study are deposited to NCBI Gene expression Omnibus (GEO) with the following accession numbers: GSE268721, GSE268780, GSE268803, and GSE269111. Previous datasets used in this study are GSE108038 and GSE78117. Source data underlying all graphs in the main figures and Extended Data figures are provided with this paper. The unique reagents generated in this study are available from the corresponding author upon reasonable request.

Research involving human participants, their data, or biological material

Policy information about studies with human participants or human data. See also policy information about sex, gender (identity/presentation), and sexual orientation and race, ethnicity and racism.

Reporting on sex and gender	na
Reporting on race, ethnicity, or other socially relevant groupings	na
Population characteristics	na
Recruitment	na
Ethics oversight	Human samples were sourced from the New York Brain Bank and anonymized to ensure that researchers had no access to the personal information of the donors. Approval from the Institutional Review Board at Columbia University Irving Medical Center was obtained prior to the generation of clinical data.

Note that full information on the approval of the study protocol must also be provided in the manuscript.

Field-specific reporting

Please select the one below that is the best fit for your research. If you are not sure, read the appropriate sections before making your selection.

☒ Life sciences ☐ Behavioural & social sciences ☐ Ecological, evolutionary & environmental sciences

For a reference copy of the document with all sections, see nature.com/documents/nr-reporting-summary-flat.pdf

Life sciences study design

All studies must disclose on these points even when the disclosure is negative.

Sample size	For single-cell sequencing experiments, SCOPIT was used to estimate sequencing depth and cell numbers. For experimental studies, sample sizes were guided by prior work in the field and, where appropriate, power calculations performed using G*Power or nQuery. For analyses of human cohorts, postmortem tissue, cerebrospinal fluid, proteomic, transcriptomic, and genetic datasets, all available eligible samples meeting predefined inclusion criteria were analyzed; no formal sample size calculations were performed for these observational studies. For imaging datasets involving nested measurements, the biological replicate (animal or donor) was predefined as the independent unit of inference.
Data exclusions	No animals, human donors, biological replicates, or experimental datasets were excluded from the analyses except where technical sample

Data exclusions	preparation or processing problems occurred, as described in the Methods. For sequencing experiments, low-quality cells and doublets were removed during standard quality-control processing before downstream analyses.
Replication	Experimental findings were independently replicated where appropriate using biological replicates, independent human cohorts, complementary experimental systems, and orthogonal methodologies. Representative microscopy and immunoblot images are from experiments repeated independently with similar results, as indicated in the figure legends. For experimental studies, a minimum of three biological replicates (individual animals or human donors) per condition was used where applicable. Multiple measurements (e.g., vessels or ROIs) obtained from the same individual were treated as nested observations and analyzed using cluster-aware statistical models, with the biological replicate defined as the independent unit of inference.
Randomization	Animals were randomly assigned to experimental and control groups where applicable to minimize selection bias. Experimental groups were balanced across independent experiments, and randomized block designs were used when appropriate. Human postmortem tissues, cerebrospinal fluid samples, and publicly available transcriptomic and genetic datasets were observational and therefore not subject to experimental allocation. Image acquisition and quantitative analyses were performed in a blinded manner, and statistical analyses accounted for relevant biological covariates where appropriate.
Blinding	Image acquisition and quantitative image analyses in zebrafish and mouse experiments were performed in a blinded manner. Tissue staining and labeling were performed by one investigator, while image quantification was performed independently with sample identities concealed until completion of the analysis. Blinding was not applicable to computational analyses of previously generated datasets or automated bioinformatic workflows, which were performed using predefined analysis pipelines.

Reporting for specific materials, systems and methods

We require information from authors about some types of materials, experimental systems and methods used in many studies. Here, indicate whether each material, system or method listed is relevant to your study. If you are not sure if a list item applies to your research, read the appropriate section before selecting a response.

Materials & experimental systems

n/a	Involved in the study
☐	☒ Antibodies
☐	☒ Eukaryotic cell lines
☒	☐ Palaeontology and archaeology
☐	☒ Animals and other organisms
☒	☐ Clinical data
☒	☐ Dual use research of concern
☒	☐ Plants

Methods

n/a	Involved in the study
☒	☐ ChIP-seq
☐	☒ Flow cytometry
☒	☐ MRI-based neuroimaging

Antibodies

Antibodies used

For the immunohistochemistry (IHC), the primary antibodies used included:

FN1 (Proteintech, Cat.# 66042-1-Ig, dilution 1:250 and 1:300), (Sigma, Cat. #F3648, dilution 1:100),
CD31 (Abcam, Cat.# ab134168, dilution 1:250 and 1:300), CD31 (BD Biosciences, Cat # 550389, dilution 1:200)
GFAP (Thermo Fisher, Cat.# OPA1-06100, dilution 1:250), GFAP (Abcam, Cat.#4674, dilution 1:500), GFAP (Novus, Cat.# NBP1-05198, dilution 1:2500)
VEGF (R&D Systems, Cat.# MAB2932-100, dilution 1:200 and 1:300)
IGF-1 (Abcam, Cat.# ab106836, dilution 1:200 and 1:300), IGF1 (Abcam, Cat #ab9572, dilution 1:500)
HB-EGF (Thermo Fisher, Cat.# PA5-119187, dilution 1:200 and 1:300)
A-beta42 (Cell Signaling, Cat.# 8243S, dilution 1:200)
GS (Abcam, Cat.# ab176562, dilution 1:500)
MAP2 (Abcam Cat. #ab5392, dilution 1:1000)
MBP (Abcam Cat #ab133620, dilution 1:20000)
IBA1 (Abcam Cat# ab283319, dilution 1:500), (WAKO, Cat #011-27991, dilution 1:100)
CD140b (R&D Systems Cat #AF385, dilution 1:100)
4G8 (Biolegend Cat# 800701, dilution 1:100)
AQP4 (Abcam Cat #ab282586, dilution 1:10000), (Abcam Cat #ab284135 dilution 1:200), (Proteintech Cat #CL594-16473 dilution 1:500)
CDH5 (Thermo Fisher Cat #PA5-143232, dilution 1:200)
Fibrinogen (Abcam Cat #ab34269, dilution 1:100 and 1:300)
APOE (Millipore Sigma Cat #Calbiochem 178479, dilution 1:200), (Bioss Cat #bs-5039R, dilution 1:200)
B2M (Abcam Cat #ab75853, dilution 1:200)
ZO-1 (Thermo Fisher, Cat.# 33-9100, dilution 1:500), ZO1 (Proteintech, cat# 21773-1-AP, dilution factor 1:200)
GFP (Thermo Fisher, Cat.# PA1-9533, dilution 1:2000)
BLBP (Abcam, Cat.# ab281734, dilution 1:1000), BLBP (Abcam, Cat.# ab279649, dilution 1:500)
PDGFRB (R&D Systems, Cat. #AF385-SP, dilution 1:100)
FN1-EDA (Antibodies-online, Cat.# ABIN108413, dilution 1:200)
FN1-EDB (Cell Signaling, Cat.# 36349, dilution 1:200)
Fibronectin (Thermo Fisher, Cat.# PA5-29578, dilution 1:250)
Anti-Dextran Antibody, Clone DX1; Unconjugated, mouse mAb IgG1 (Stem Cell, Cat # 60026, dilution 1:500)

The secondary antibodies employed were:
Goat anti-mouse Alexa Fluor 448 (Thermo Fisher, Cat.# A11001, dilution 1:500)
Goat anti-chicken Alexa Fluor 448 (Thermo Fisher, Cat.# A11039, dilution 1:500)
Goat anti-rabbit Alexa Fluor 555 (Thermo Fisher, Cat.# A32732, dilution 1:500)
Goat anti-mouse Alexa Fluor 555 (Thermo Fisher, Cat.# A21127, dilution 1:500)
Goat anti-mouse Alexa Fluor 568 (Thermo Fisher, Cat.# A11019, dilution 1:250)
Goat anti-rabbit Alexa Fluor 647 (Thermo Fisher, Cat.# A32733, dilution 1:500)
Donkey anti-mouse Alexa Fluor 488 (Thermo Fisher, Cat.# A32766, dilution 1:500)
Donkey anti-goat Alexa Fluor 555 (Thermo Fisher, Cat.# A32816, dilution 1:500)
Donkey anti-rabbit Alexa Fluor 647 (Thermo Fisher, Cat.# A32795, dilution 1:500)
Donkey anti-Rabbit IgG Alexa Fluor 647(Thermo Fisher Scientific, #A31573, dilution 1:1000)
Donkey anti-Mouse IgG AF750 (Thermo Fisher Scientific, #SA000081, dilution 1:1000)
Donkey anti-Chicken IgY AF647 (Thermo Fisher Scientific, #A78952, dilution 1:1000)
Donkey anti-mouse IgG AF568 (Thermo Fisher Scientific, #A10037, dilution 1:1000)
Donkey anti-Chicken IgY AF488 (Thermo Fisher Scientific, #A78948, dilution 1:1000)
Donkey anti-Goat IgG Alexa 4Fluor 488 (Thermo Fisher Scientific, #A-11055 1:1000)
Donkey anti-Goat IgG AF647 (Jackson Immunoresearch, #705-606-147, dilution 1:250)
Donkey anti-rabbit F(ab)' AlexaFluor-647 (Jackson ImmunoResearch 711-605-152, dilution 1:250)
Donkey anti-rabbit F(ab)' AlexaFluor-488 (Jackson ImmunoResearch 715-545-150, dilution 1:250)

For Western Blot and Co-immunoprecipitation, following antibodies were used:
Fibronectin (Invitrogen PA5-29578, 1:1000), FN1 (Proteintech, Cat.# 66042-1-Ig, dilution 1:1000)
b-actin (Millipore Sigma A5316-100UL, dilution 1:1000)
APOE (Millipore Sigma/Calbiochem, Cat. #178479, dilution 1:1000)

Validation

Antibodies are validated by the manufacturer through wither western blots, immunization peptide inhibition or knockout validation. All antibodies were tested for efficacy and reliability with no-primary controls in human samples, cell cultures,and zebrafish before use.

Eukaryotic cell lines

Policy information about cell lines and Sex and Gender in Research

Cell line source(s)

Primary human fetal astrocytes were obtained from ScienCell Research Laboratories (Cat. #1800; sex not specified by the vendor). KOLF2.1J isogenic human iPSC lines (male donor) expressing APOEε3/3 or APOEε4/4 variants were used, together with additional previously published APOE isogenic iPSC lines derived from four independent human donors, as described in the Methods. iPSCs were maintained under feeder-free conditions in mTeSR1 medium and differentiated into astrocytes, endothelial cells, mural cells, and 3D vascular models as described. Differentiation efficiency was confirmed by immunostaining for lineage-specific markers.

Authentication

Primary human fetal astrocytes were commercially obtained from ScienCell Research Laboratories and authenticated by the vendor. KOLF2.1J and the additional APOE isogenic iPSC lines were authenticated by genotype verification and G-banded karyotyping, as described in the original publications and confirmed prior to use. All lines used in this study exhibited normal karyotypes.

Mycoplasma contamination

Cells are negative for HIV-1, HBV, HCV, mycoplasma, bacteria, yeast, and fungi.

Commonly misidentified lines
(See ICLAC register)

The cell lines used in this study are not listed in the ICLAC register of commonly misidentified cell lines.

Animals and other research organisms

Policy information about studies involving animals; ARRIVE guidelines recommended for reporting animal research, and Sex and Gender in Research

Laboratory animals

Human APOE targeted replacement mice on a C57BL/6J background (APOEε3 and APOEε4 lines) and APPNL-G-F knock-in mice (C57BL/6J background; Swedish, Arctic, and Iberian mutations) were used. Age- and sex-matched C57BL/6J wild-type mice served as controls where appropriate. Adult Tg(kdrl:GFP) zebrafish (Danio rerio; approximately 6 months of age; both sexes) were used for VEGFR inhibition studies. Tg(fli1a:EGFP) and Tg(her4.1:RFP) zebrafish lines were used for cell sorting and functional analyses.

Wild animals

na

Reporting on sex

Animals from both sexes were used for this study in equal ratios.

Field-collected samples

na

Ethics oversight

All mice used in this study were treated in accordance with the National Institutes of Health Guide for the Care and Use of Laboratory Animals and approved by the Columbia University Medical Center Institutional Animal Care and Use Committee (IACUC) (approval number AABF3553 and AABR4602). Animals were maintained under temperature and humidity-controlled environment of Columbia University Medical Center on a 12/12-h light/dark cycle, with ad libitum access to food and water in compliance with the protocols approved by the Institutional Animal Care and Use Committee of Columbia University (IACUC). For zebrafish, all animal experiments were performed in accordance with the applicable regulations and approved by the Institutional Animal Care and Use Committee

(IACUC) at Columbia University (protocol number AC-AABN3554). Animals from the same fish clutch were randomly distributed for each experimental group. Animals were handled with caution to reduce suffering and overall animal numbers.

Note that full information on the approval of the study protocol must also be provided in the manuscript.

Plants

Seed stocks

Report on the source of all seed stocks or other plant material used. If applicable, state the seed stock centre and catalogue number. If plant specimens were collected from the field, describe the collection location, date and sampling procedures.

Novel plant genotypes

Describe the methods by which all novel plant genotypes were produced. This includes those generated by transgenic approaches, gene editing, chemical/radiation-based mutagenesis and hybridization. For transgenic lines, describe the transformation method, the number of independent lines analyzed and the generation upon which experiments were performed. For gene-edited lines, describe the editor used, the endogenous sequence targeted for editing, the targeting guide RNA sequence (if applicable) and how the editor was applied.

Authentication

Describe any authentication procedures for each seed stock used or novel genotype generated. Describe any experiments used to assess the effect of a mutation and, where applicable, how potential secondary effects (e.g. second site T-DNA insertions, mosiacism, off-target gene editing) were examined.

Flow Cytometry

Plots

Confirm that:

☒ The axis labels state the marker and fluorochrome used (e.g. CD4-FITC).

☒ The axis scales are clearly visible. Include numbers along axes only for bottom left plot of group (a 'group' is an analysis of identical markers).

☒ All plots are contour plots with outliers or pseudocolor plots.

☒ A numerical value for number of cells or percentage (with statistics) is provided.

Methodology

Sample preparation

Zebrafish brains were dissected and single-cell suspensions were prepared according to previously established protocols (https://doi.org/10.1016/j.xpro.2020.100042). The telencephalon of 6–16-month-old fish was dissected in ice-cold PBS and enzymatically dissociated using the Neural Tissue Dissociation Kit (Miltenyi Biotec, Cat. No. 130-092-628). After dissociation, cells were filtered through a 40 µm cell strainer into PBS containing 2% BSA, centrifuged at 300 g for 10 min, and resuspended in PBS with 4% BSA. Viability indicator dyes Sytox Blue (Invitrogen, Cat. No. S34857) and DyeCycle Ruby (Invitrogen, Cat. No. V10309) were used during fluorescence-activated cell sorting (FACS). Samples from different experimental groups were processed in parallel to minimize processing-related variability.

Instrument

Sony MA900-FP cell sorter (Sony Biotechnology).

Software

Sony Cell Sorter Software (Sony Biotechnology).

Cell population abundance

For VEGFR inhibition experiments, a total of 24,518 sorted cells were collected and analyzed. For fn1b$^{-/-}$ experiments, 66,848 sorted cells were collected across biological replicates.

Gating strategy

Sytox Blue–negative (viable) and DyeCycle Ruby–positive (proliferating) cell populations were gated for cell viability. FSC-A/SSC-A gates were used to select the cellular fraction, and FSC-H/FSC-A gating was applied to exclude doublets. Gates were established using unstained and single-color controls and applied consistently across all samples. Representative sorting histograms are provided in Supplementary Information 1.

☒ Tick this box to confirm that a figure exemplifying the gating strategy is provided in the Supplementary Information.